

ALMA Observations of Massive Clouds in the Central Molecular Zone: External-Pressure-Confining Dense Cores and Salpeter-like Core Mass Functions

ZHENYING ZHANG (张朕荧),^{1,2} XING LU (吕行),² TIE LIU (刘铁),² SHENG-LI QIN (秦胜利),¹ ADAM GINSBURG,³ YU CHENG (程宇),⁴ HAUYU BAOBAB LIU,^{5,6} DANIEL L. WALKER,⁷ XINDI TANG (汤新弟),^{8,9,10,11} SHANHUAO LI (李尚活),¹² QIZHOU ZHANG,¹³ THUSHARA PILLAI,¹⁴ JENS KAUFFMANN,¹⁴ CARA BATTERSBY,¹⁵ SIYI FENG (冯思轶),¹⁶ SUINAN ZHANG (张遂楠),² QI-LAO GU (顾琦烙),² FENGWEI XU (许峰玮),^{17,18,19} WENYU JIAO (焦文裕),² XUNCHUAN LIU (刘训川),² LI CHEN (陈立),¹ QIU-YI LUO (罗秋怡),^{2,20,21} XIAOFENG MAI (麦晓枫),^{2,20} ZI-YANG LI (李紫杨),^{1,2} DONGTING YANG (杨东庭),¹ XIANJIN SHEN (沈先进),¹ MEIZHU LIU (刘梅竹),²² AND ZHIQIANG SHEN²

¹School of Physics and Astronomy, Yunnan University, Kunming 650091, People's Republic of China

²Shanghai Astronomical Observatory, Chinese Academy of Sciences, 80 Nandan Road, Shanghai 200030, People's Republic of China

³Department of Astronomy, University of Florida, 211 Bryant Space Science Center P.O Box 112055 Gainesville, FL 32611-2055, USA

⁴National Astronomical Observatory of Japan, National Institutes of Natural Sciences, 2-21-1 Osawa, Mitaka, Tokyo 181-8588, Japan

⁵Department of Physics, National Sun Yat-Sen University, No. 70, Lien-Hai Road, Kaohsiung City 80424, Taiwan, R.O.C.

⁶Center of Astronomy and Gravitation, National Taiwan Normal University, Taipei 116, Taiwan

⁷UK ALMA Regional Centre Node, Jodrell Bank Centre for Astrophysics, The University of Manchester, Manchester M13 9PL, UK

⁸Xinjiang Astronomical Observatory, 150 Science 1-Street, Urumqi, Xinjiang 830011, Peoples Republic of China

⁹University of Chinese Academy of Sciences, Beijing, 100080, Peoples Republic of China

¹⁰Key Laboratory of Radio Astronomy, Chinese Academy of Sciences, Urumqi, 830011, Peoples Republic of China

¹¹Xinjiang Key Laboratory of Radio Astrophysics, Urumqi, 830011, Peoples Republic of China

¹²Max Planck Institute for Astronomy, Königstuhl 17, D-69117 Heidelberg, Germany

¹³Center for Astrophysics — Harvard & Smithsonian, 60 Garden Street, Cambridge, MA 02138, USA

¹⁴Haystack Observatory, Massachusetts Institute of Technology, 99 Millstone Road, Westford, MA 01886, USA

¹⁵Department of Physics, University of Connecticut, 196A Auditorium Road, Unit 3046 Storrs, CT 06269, USA

¹⁶Department of Astronomy, Xiamen University, Zengcuo'an West Road, Xiamen, 361005, Peoples Republic of China

¹⁷Kavli Institute for Astronomy and Astrophysics, Peking University, Beijing 100871, People's Republic of China

¹⁸I. Physikalisches Institut, Universität zu Köln, Zülpicher Str. 77, D-50937 Köln, Germany

¹⁹Department of Astronomy, School of Physics, Peking University, Beijing, 100871, People's Republic of China

²⁰School of Astronomy and Space Sciences, University of Chinese Academy of Sciences, No. 19A Yuquan Road, Beijing 100049, People's Republic of China

²¹Key Laboratory of Radio Astronomy and Technology, Chinese Academy of Sciences, A20 Datun Road, Chaoyang District, Beijing, 100101, People's Republic of China

²²Center for Astrophysics, Guangzhou University, Guangzhou 510006, People's Republic of China

ABSTRACT

We present Atacama Large Millimeter/submillimeter Array (ALMA) Band 6 (1.3 mm) observations of dense cores in three massive molecular clouds within the Central Molecular Zone (CMZ) of the Milky Way, including the Dust Ridge cloud e, Sgr C, and the 20 km s⁻¹ cloud, at a spatial resolution of 2000 au. Among the 834 cores identified from the 1.3 mm continuum, we constrain temperatures and linewidths of 253 cores using local thermodynamic equilibrium (LTE) methods to fit the H₂CO and/or CH₃CN spectra. We determine their masses using the 1.3 mm dust continuum and derived temperatures, and then evaluate their virial parameters using the H₂CO and/or CH₃CN linewidths and construct the core mass functions (CMFs). We find that the contribution of external pressure is crucial for the virial equilibrium of the dense cores in the three clouds, which contrasts with the environment in the Galactic disk where dense cores are already bound even without the contribution of external pressure. We also find that the CMFs show a Salpeter-like slope in the high-mass ($\gtrsim 3\text{--}6 M_{\odot}$) end, a change from previous works with our new temperature estimates. Combined with the possible

top-heavy initial mass functions (IMFs) in the CMZ, our result suggests that gas accretion and further fragmentation may play important roles in transforming the CMF to the IMF.

Keywords: Galactic center — Star formation — Molecular clouds — Core Mass Function

1. INTRODUCTION

The central molecular zone (CMZ) of the Milky Way, located at the Galactic Center with a radius of approximately 300 pc, exhibits distinctive characteristics compared to the star formation environment in the solar neighborhood (Henshaw et al. 2023). There is molecular gas with a mass exceeding $10^7 M_{\odot}$ (Morris & Serabyn 1996; Longmore et al. 2013; Battersby et al. 2024), an average gas number density of approximately 10^4 cm^{-3} (Paglione et al. 1998; Longmore et al. 2013), a high gas temperature of 50–100 K (Ao et al. 2013; Ginsburg et al. 2016; Krieger et al. 2017), a strong magnetic field of about 1 mG (Pillai et al. 2015; Lu et al. 2024), and strong turbulence of Mach numbers \mathcal{M} of around 30 (Rathborne et al. 2014; Henshaw et al. 2016). Barnes et al. (2017) found an incipient star formation rate (SFR) for the CMZ of about $0.09 \pm 0.02 M_{\odot} \text{ yr}^{-1}$, which is one order of magnitude lower than expected based on the dense gas-star formation relationship (Longmore et al. 2013; Kauffmann et al. 2017b; Lu et al. 2019a). A possible explanation for this could be that the clouds in the CMZ are in an early stage of evolution or that strong turbulence suppresses the collapsing and fragmentation of the clouds (Kruijssen et al. 2014; Krumholz et al. 2017).

The initial mass function (IMF) is the distribution of stellar masses of zero-age main sequence stars. It is crucial for various fields in astrophysics, from star formation to galaxy evolution. It is believed to be universally applicable (Kroupa 2002; Bastian et al. 2010; Matthews et al. 2014), although potential variations with respect to local environments have been found (e.g., Hopkins 2018; Li et al. 2023a). The high-mass end of the IMF roughly follows a power law of the following form: $\frac{dN}{d \log M} \propto M^{-\alpha}$. Kroupa (2002) fitted a power law index of $\alpha = 1.35$. However, there is still controversy over the origin of the IMF and its dependence on environment.

Stars form in dense cores (Bergin & Tafalla 2007). Therefore, it has been suggested that the IMF is related to the core mass function (CMF), an analog of the IMF that describes the distribution of core masses in a star formation region (Hennebelle & Chabrier 2008; Offner et al. 2014; Ntormousi & Hennebelle 2019). Numerical simulations have produced CMFs with a shape consistent with that of the IMF (Klessen 2000; Padoan & Nordlund 2011). Therefore, studying the CMF is cru-

cial for exploring the origin of the IMF and investigating the early stages of star formation. Recent results from the ALMA-IMF large program (Motte et al. 2022; Ginsburg et al. 2022; Pouteau et al. 2023) suggested that as molecular clouds evolve from quiescent to burst phases, the CMF may change from Salpeter-like to top-heavy, and then it might return to Salpeter-like as clouds approach the end of their star-forming phase.

The CMZ is a specific target of interest for studying the relation between the CMF and IMF in extreme star forming environment. The IMF in young massive star clusters in the CMZ has been measured to be top-heavy, i.e., with an overpopulation of higher mass stars with respect to the ‘canonical’ power-law form of $\frac{dN}{d \log M} \propto M^{-1.35}$ (Hußmann et al. 2012; Hosek et al. 2019). Meanwhile, previous ALMA observations of dense cores in the CMZ clouds found signatures of top-heavy CMFs (e.g., Lu et al. 2020). However, there has been a dearth of constraints on the temperature of dense cores in the CMZ while estimating the core masses. Usually, a uniform core temperature (e.g., 20 K) is assumed, which could be biased and lead to large uncertainties in the CMFs (see Appendix D of Lu et al. 2020). Furthermore, the analysis of virial equilibrium of dense cores in the CMZ has been hindered because of a lack of spectral line observations that are able to measure the turbulent line width. Without the knowledge of virial states of cores, we cannot separate gravitationally bound cores that are deemed to collapse and form stars from unbound cores that do not form stars.

To more robustly characterize the masses and virial states of cores in the CMZ, we employ the H_2CO and CH_3CN molecular lines to constrain the temperatures and velocity dispersions of cores in three massive molecular clouds in the CMZ. The rotational transitions of H_2CO and the CH_3CN *K*-ladder are widely-used thermometers in observations of dense gas in clouds and cores (e.g., Downes et al. 1980; Bieging et al. 1982; Zylka et al. 1992; Mangum et al. 2008; Ao et al. 2013; Tang et al. 2013). In particular, we focus on the following H_2CO transitions: $J_{K_1, K_2} = 3_{0,3}-2_{0,2}$ ($E_u/k = 20.95 \text{ K}$, $f_{\text{rest}} = 218.222192 \text{ GHz}$), $2_{2,2}-2_{2,1}$ ($E_u/k = 68.09 \text{ K}$, $f_{\text{rest}} = 218.47563 \text{ GHz}$), and $2_{2,1}-2_{2,0}$ ($E_u/k = 68.11 \text{ K}$, $f_{\text{rest}} = 218.76007 \text{ GHz}$). Their critical densities at the temperature of 100 K is $\sim 3 \times 10^5 \text{ cm}^{-3}$. For CH_3CN , the transitions of interest include the *K*-ladder from

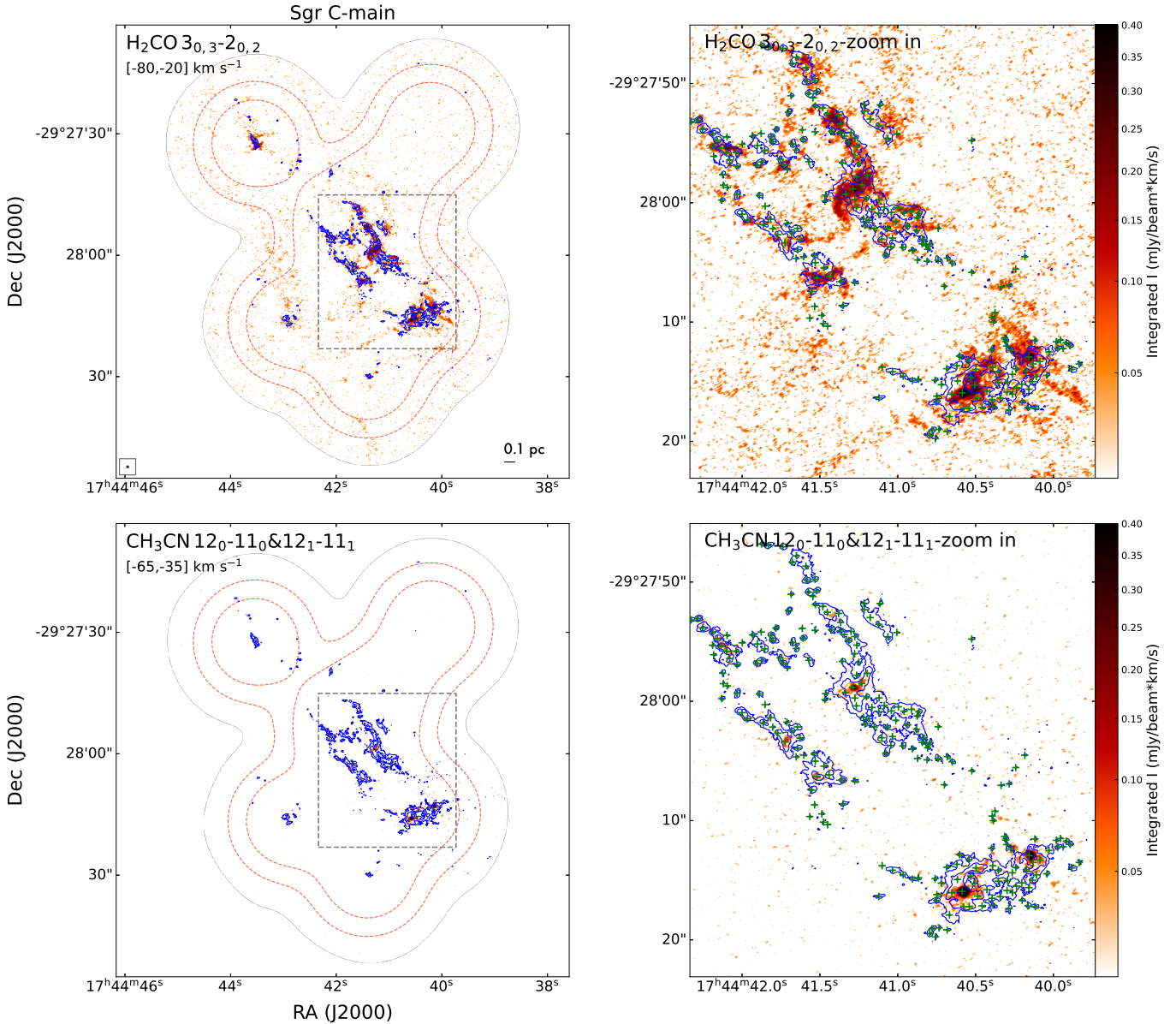


Figure 1. The integrated intensity (0th moment) maps of the H₂CO and CH₃CN line emission toward the three clouds. The inner and outer red dashed loops in the left panels show the ALMA primary-beam responses at 50% and 30%, respectively. The left panels show the integrated intensities of H₂CO 3_{0,3}-2_{0,2} and CH₃CN 12₀-11₀/ 12₁-11₁, while the right panels are the zoomed-in views of the dashed boxes in the left panels. The blue contours show the 1.3 mm dust continuum at levels of 5 and 20 $\times \sigma$, where $\sigma = 40 \mu\text{Jy beam}^{-1}$. The green '+' symbols illustrate the peak positions of the cores identified from the 1.3 mm continuum. (The complete figure set (7 images) is available in the online journal.)

$J_K = 12_0-11_0$ ($E_u/k = 68.86$ K, $f_{\text{rest}} = 220.7472$ GHz) to 12_7-11_7 ($E_u/k = 325.899$ K, $f_{\text{rest}} = 220.5944$ GHz), with a critical density at 100 K of $\sim 5 \times 10^6 \text{ cm}^{-3}$. The cloud sample includes the relatively quiescent Dust Ridge cloud e (cloud e hereafter), the 20 km s⁻¹ cloud in an intermediate star formation state, and the actively star forming Sgr C (Lu et al. 2019b, 2021). These clouds are selected from a representative sample of massive clouds in the CMZ (Kauffmann et al. 2017a,b) and show clear fragmentation in our ALMA 1.3 mm contin-

uum observations at a resolution of 2000 au (Lu et al. 2020). Additionally, we incorporate the impact of external pressure into the virial analysis, by using the SMA molecular line data from Lu et al. (2019b).

The structure of the paper is organized as follows: In Section 2, we describe the observations and data reduction. In Section 3, we present the observational results. We then discuss the virial parameters, and the CMF within the molecular clouds in Section 4. Finally, we summarize our findings in Section 5. Throughout the

paper, we adopt a distance of 8.277 kpc to the Galactic Center ([GRAVITY Collaboration et al. 2022](#)) and assume that all the clouds under consideration are at this distance.

2. OBSERVATIONS AND DATA REDUCTION

The ALMA observations have been presented in [Lu et al. \(2020, 2021\)](#), where details of the observational setups and data reduction can be found. Here we reiterate the information that is related to our analysis in the current work.

The ALMA 12-m array observations in Band 6 toward the three clouds were conducted in the C40-5 and C40-3 configurations during April and July 2017 under the Project 2016.1.00243.S (PI: Q. Zhang). The correlators were configured to cover frequency ranges of 217–221 GHz and 231–235 GHz, with a uniform frequency resolution of 0.977 MHz (equivalent to a velocity resolution of 1.3 km s^{-1}). In this paper, we present the results derived from the 1.3 mm continuum and molecular line data of H₂CO transitions $3_{0,3}-2_{0,2}$, $3_{2,2}-2_{2,1}$, and $3_{2,1}-2_{2,0}$, as well as the CH₃CN transitions 12_0-11_0 to 12_7-11_7 .

The calibration and imaging of the data were performed using the Common Astronomy Software Application (CASA) version 5.4.0 ([CASA Team et al. 2022](#)). The calibrated data were then imaged using the `tclean` task with a robust Briggs parameter of 0.5. The achieved angular resolution of the images is approximately $0''.24 \times 0''.18$. The sensitivity of the spectral line data is in the range of $1.6\text{--}2.0 \text{ mJy beam}^{-1}$ per 1.3 km s^{-1} channel.

3. RESULTS

In [Lu et al. \(2020\)](#), the identification of dense cores in the three clouds has been carried out using the dendrogram algorithm implemented in the astrodendro package¹ upon the continuum images, where the ‘leaves’ of the dendograms were considered as dense cores. The three key parameters in astrodendro, the minimum intensity, the minimum significance, and the minimum area of leaves were set to 4σ , 1σ , and one synthesized beam size (i.e., 30.125 pixels), respectively, where $\sigma = 40 \text{ mJy beam}^{-1}$. In cloud e, Sgr C, and the 20 km s^{-1} cloud, 89, 274, and 471 cores were identified, respectively. The 1.3 mm continuum flux within the boundary of each leaf, defined by the 4σ contour, without removing any background contribution from the larger structures within the dendrogram hierarchy, was adopted as the

flux of a core. Here we directly adopted the core catalogs of [Lu et al. \(2020\)](#), and extracted the H₂CO and/or CH₃CN spectra toward the cores for fitting.

As discussed in [Lu et al. \(2020\)](#), the maximum recoverable scale as determined by the short baselines in the ALMA array during our observations is $7''$ ($\sim 0.3 \text{ pc}$), whereas we focus on the dense cores at much smaller scales of 2000 AU. The missing flux issue of ALMA as an interferometer unlikely affects the measurement of fluxes of the cores significantly.

3.1. Overview of the spectral line emission

[Figure 1](#) illustrates the integrated intensity maps of the H₂CO $3_{0,3}-2_{0,2}$ and CH₃CN $12_0-11_0/12_1-11_1$ transitions in the three molecular clouds. Note that no masking was applied to the moment maps. The velocity ranges adopted for integrating the intensities are marked in the panels. We integrated the 12_0-11_0 and 12_1-11_1 transitions of CH₃CN altogether because the two lines are blended and therefore cannot be separated.

As shown in [Figure 1](#), we found that the CH₃CN emission is mostly only detected towards the 1.3 mm emission. However, the H₂CO $3_{0,3}-2_{0,2}$ emission is not always associated with the 1.3 mm continuum, especially toward Sgr C and the 20 km s^{-1} cloud where a significant number of filamentary structures in the H₂CO emission are observed. A subset of these filaments have been identified as protostellar outflows in [Lu et al. \(2021\)](#). The others are likely related to pc-scale shocks, which will be discussed in other works of the series (K. Yang et al. in prep.). For the H₂CO emission spatially coincident with the identified cores, we assumed that it traces dense gas in the cores and therefore can be used to estimate the gas temperature and linewidth of the cores. In [Appendix C](#), we compared H₂CO gas associated with the cores and that not associated with any cores, and found that the two samples of H₂CO emissions present statistically different temperatures, with the H₂CO associated with the cores showing lower temperatures.

3.2. Core temperatures from H₂CO and CH₃CN

[Figure 2](#) left provides examples of the observed mean spectra of H₂CO within dense cores from the three clouds, showing the three transitions $3_{0,3}-2_{0,2}$, $3_{2,2}-2_{2,1}$, and $3_{2,1}-2_{2,0}$. [Figure 2](#) right presents the observed mean spectra of CH₃CN within dense cores from the three clouds, encompassing lines from 12_0-11_0 to 12_7-11_7 . Gaussian fits were employed on the mean H₂CO and CH₃CN spectra to estimate temperatures and velocity dispersions of the dense cores, which were later used for estimating the masses and virial states of the cores.

¹ <http://www.dendrograms.org>

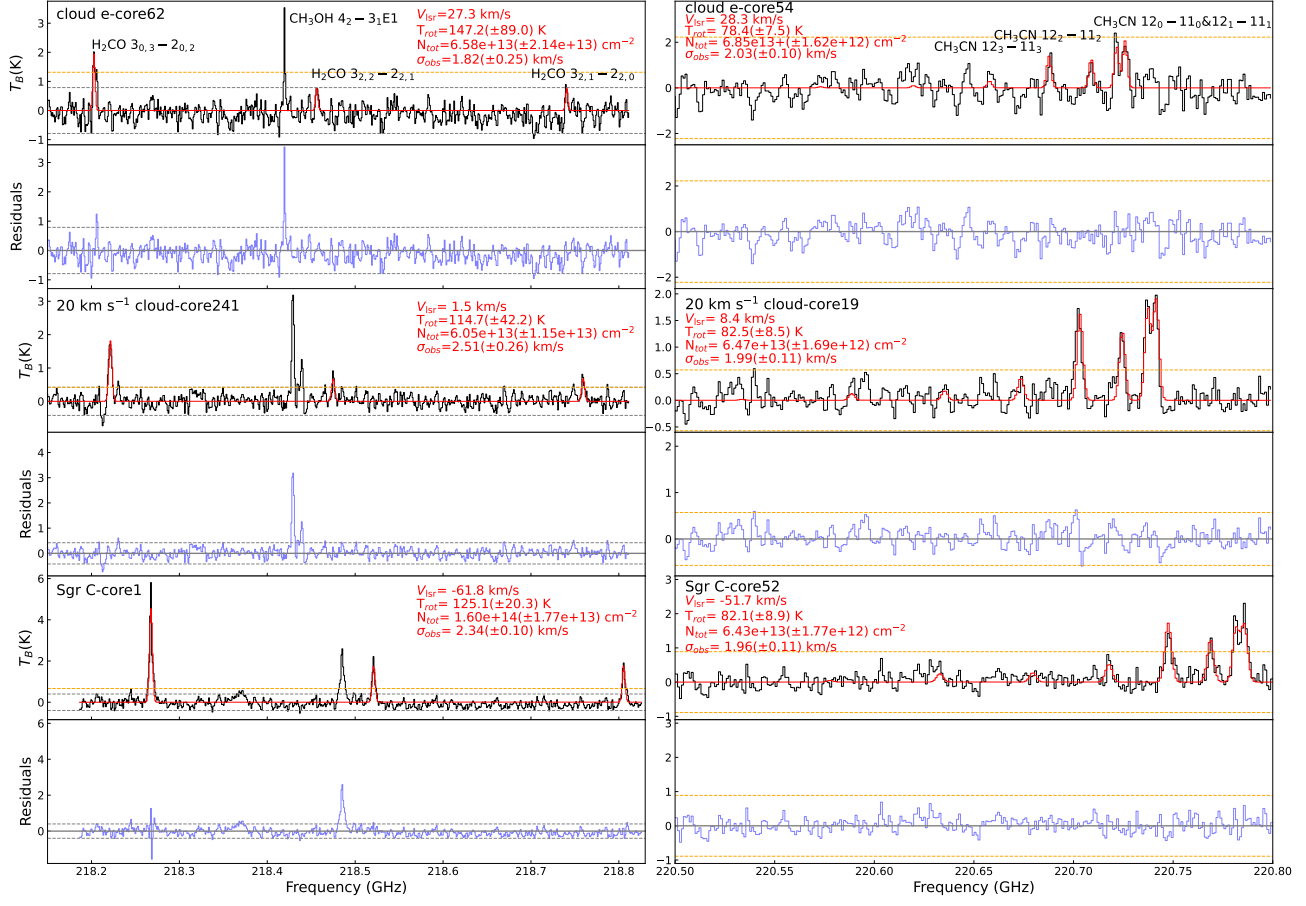


Figure 2. Examples of H₂CO (left) and CH₃CN (right) spectra detected in three cores, each from one of the three clouds. The complete gallery of all the fitting results can be found in Appendix A. The black curves show the observed spectra, while the red curves are the results of the LTE fits. The gray dashed lines indicate the $\pm 3\sigma$ levels, while the orange dashed line represents the 5σ level. Above the spectra display the core indices, the best-fit centroid velocity, temperature, column density, and velocity dispersion. The blue curves below the spectra represent the fit residuals.

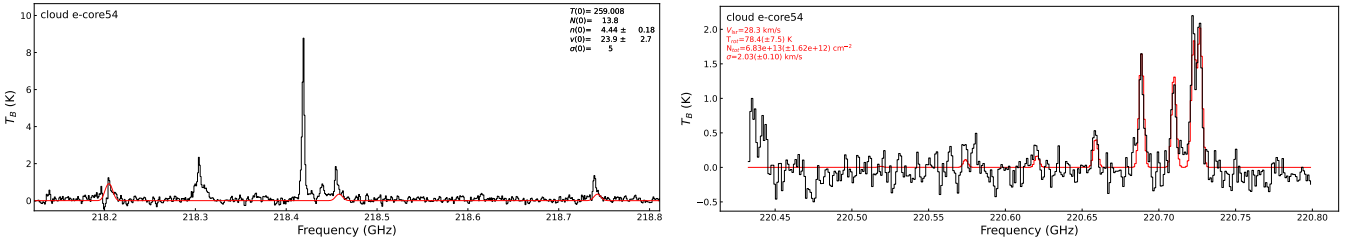


Figure 3. The LTE fitting results for core 54 in cloud e, using the FFFL code to fit H₂CO (left) and the EMANON code to fit CH₃CN (right). The H₂CO lines show clear self absorption, and therefore cannot be fit reasonably.

Note that when both H₂CO and CH₃CN lines are detected towards a core, the fitting result using CH₃CN was adopted, as in such cases the H₂CO lines are always optically thick and show self absorption making the fit impractical (see Figure 3).

For the fitting of the H₂CO lines, we employed the FFFL code² that assumes the LTE conditions. The LTE is likely achieved in the cores given the high densities of $\gtrsim 10^6$ cm⁻³ (Goldsmith 2001). Nonetheless, to validate the results, we also performed fitting using the non-LTE method implemented with RADEX (van der

3.2.1. Fitting spectral lines

² <https://github.com/xinglunju/FFFL>

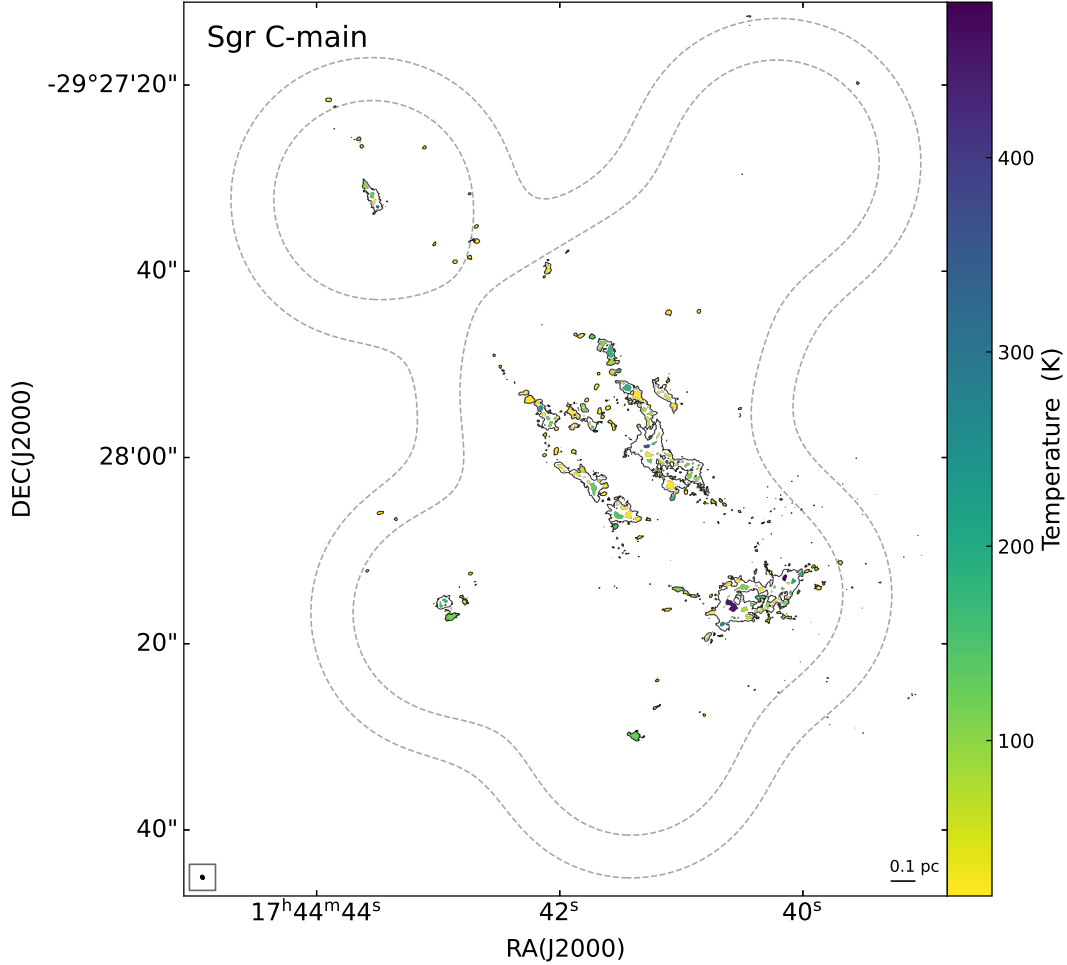


Figure 4. An overview of the temperatures of the cores. The inner and outer dashed loops represent the ALMA primary-beam responses at 50% and 30%, respectively. The black contour represents the 1.3 mm continuum emission at the level of 5σ . The color patches show the positions and morphologies of the cores (see Table 1), color-coded by their temperatures. Note that for cores (132/268) where neither H₂CO nor CH₃CN is detected, we assume a temperature of 20 K. (The complete figure set (7 images) is available in the online journal.)

Tak et al. 2007) within the PySpecKit package (Ginsburg et al. 2022), with results presented in Appendix A. We found consistent temperatures and velocity dispersions between the LTE and non-LTE methods as shown in Figure A4.

The FFTL code performs forward modeling, in which model spectra are constructed based on the input temperature, column density, velocity dispersion, and the centroid velocity. Then the difference between the model spectra and the observed one is minimized using the *lmfit* package³ to derive the best-fit model spectrum, whose input parameters (most notably, the temperature and the velocity dispersion) are taken as the final fitting result.

When selecting dense cores for fitting H₂CO, we required the H₂CO 3_{0,3}–2_{0,2} spectra to have a signal-to-noise (S/N) ratio higher than 5, where the RMS noise of the mean spectra was measured between the frequency range of 218.60–218.65 GHz that is mostly line-free. Note that there are several line-rich hot cores where emission of certain lines still exists in this frequency range. The RMS noise for these hot cores could be overestimated. Then there were two scenarios:

- i) When one or both of the other two H₂CO transitions, 3_{2,2}–2_{2,1} and 3_{2,1}–2_{2,0}, have S/N ratios higher than 3, we fit the three transitions simultaneously using the FFTL code.
- ii) When both of the two transitions have S/N ratios lower than 3, we derived an upper limit for the temperature: we used the 3σ value as the upper limit for the peak intensity of the two lines, and got the upper limit

³ <https://lmfit.github.io/lmfit-py/>

of the line ratio between these two transitions and the $3_{0,3}-2_{0,2}$ transition. This line ratio was then converted to a temperature upper limit following a best-fit power law relation between the line ratio and the temperature, which is derived from the best-fit temperatures in scenario i). There are 24 cases in the three clouds where we take this approach to estimate upper limits of the core temperature. Such upper limits are marked with ‘<’ in front of the temperature values in [Table 1](#). Details of the line ratio-temperature relation can be found in [Appendix B](#).

For the cores where CH_3CN $12_0-11_0/12_1-11_1$ lines have a S/N ratio higher than 5, we also fit the CH_3CN 12_0-11_0 to 12_7-11_7 transitions to derive the temperature and velocity dispersion. The RMS noise was measured from the line-free channels in the frequency range of 220.55–220.58 GHz. We utilized the *emanon* code⁴ with the LTE assumption, which adopts the same forward-fitting approach as FFTL.

As mentioned above, for all the cores with CH_3CN detections, the H_2CO lines are also detected. We adopted the fitting results of CH_3CN , as the H_2CO lines are optically thick and exhibit pronounced self-absorption, and therefore cannot be fit robustly ([Figure 3](#)). We note that a systematic bias may exist between the best-fit parameters from the two lines, as they trace different gas components within the cores given their different excitation conditions. CH_3CN likely traces the hotter interiors of the cores, whereas H_2CO traces more extended dense gas.

To validate the fitting results of CH_3CN , we conducted a cross-check using the XCLASS package that assumed the LTE conditions as well ([Möller et al. 2017](#)). As shown in [Figure A5](#) of [Appendix A](#), we found consistent results between the *emanon* code and the XCLASS package.

In the end, for cloud e, Sgr C, and the 20 km s⁻¹ cloud, 15, 120, and 85 cores were successfully fitted with H_2CO , and 4, 17, and 12 cores were fitted with CH_3CN . [Figure 4](#) shows an overview of the core temperature. All the H_2CO and CH_3CN spectra detected toward the cores and best-fit results are presented Figures [A1](#) and [A2](#). Histograms of temperatures and velocity dispersions are presented in [Figure A3](#). The fitting results for the first 10 dense cores in each of the three clouds are showcased in [Table 1](#). A complete catalog of fitting results for all the dense cores within the three clouds can be found in [Table E1](#), [Table E2](#), and [Table E3](#), respectively.

⁴ <https://github.com/xinglunju/emanon>, named after a fiction by Shinji Kajio.

3.3. Physical Properties of the Cores

In [Table 1](#), physical properties of the dense cores within the three molecular clouds are provided. The catalog includes 19, 137, and 97 dense cores in cloud e, Sgr C, and the 20 km s⁻¹ cloud, respectively, whose H_2CO and/or CH_3CN spectra were successfully fitted.

3.3.1. Core masses

We assumed that gas and dust in the cores are coupled and therefore their temperatures are equal ($T_{\text{dust}} = T_{\text{gas}}$). This assumption are justified as the gas densities in the cores are expected to be sufficiently high ($\geq 10^6 \text{ cm}^{-3}$; [Goldsmith 2001](#)): the densities were estimated to be $\sim 10^7 \text{ cm}^{-3}$ assuming a T_{dust} of 20 K in [Lu et al. \(2020\)](#); if higher temperatures of several hundreds K were adopted (see [Section 3.2](#)), the resulting densities would be an order of magnitude lower but still $\sim 10^6 \text{ cm}^{-3}$.

As discussed in [Section 3.2.1](#), when both CH_3CN and H_2CO lines are detected towards a core, we adopted the best-fit LTE temperature of the former. When only H_2CO is detected, the best-fit LTE temperature using the H_2CO lines is adopted. If neither CH_3CN nor H_2CO is detected, a dust temperature of 20 K is adopted, which is the assumption in [Lu et al. \(2020\)](#) and corresponds to the typical value of dust temperatures in cold cores ([Bergin & Tafalla 2007](#)).

Assuming optically thin dust emission, the core mass was estimated following [Hildebrand \(1983\)](#):

$$M_{\text{core}} = \frac{D^2 S_{\nu} \eta}{\kappa_{\nu} B_{\nu}(T_{\text{dust}})}, \quad (1)$$

where D is the distance to the core ($D=8.277 \text{ kpc}$), S_{ν} is the dust emission flux, $\eta=100$ is the gas to dust mass ratio, $\kappa_{\nu}=0.899 \text{ cm}^2 \text{ g}^{-1}$ ([Ossenkopf & Henning 1994](#)) is the dust absorption coefficient, T_{dust} is the core temperature, and $B_{\nu}(T_{\text{dust}})$ is the Planck function at the temperature T_{dust} . Note that for the cores with only upper limits of temperatures (see [Section 3.2.1](#)), the derived masses would be lower limits, which we have marked with ‘>’ in front of their mass values in [Table 1](#). Also note that the gas-to-dust ratio in the CMZ could be as low as ~ 50 [Giannetti et al. \(2017\)](#). However, this does not affect our discussion of the CMF slope in [Section 3.4](#) where all core masses would scale down at the same rate, nor does it change the virial analysis in [Section 3.3.3](#), where the virial parameters would increase by a factor of 2 while all the conclusions remain unaffected.

3.3.2. Non-thermal motions in the cores

We calculated the sound speed (c_s) and the Mach number (\mathcal{M}) following

$$c_s = \sqrt{\frac{k_B T_{\text{core}}}{\mu m_H}}, \quad (2)$$

and

$$\mathcal{M} = \frac{\sigma_{\text{NT}}}{c_s} = \frac{\sqrt{\sigma_{\text{tot}}^2 - c_s^2}}{c_s}, \quad (3)$$

where k_B is the Boltzmann constant, T_{core} the temperature of the core derived in Section 3.2, μ is the mean molecular weight and is taken to be 2.37 (Kauffmann et al. 2008), m_H is the mass of the hydrogen atom, σ_{NT} is the non-thermal velocity dispersion, and σ_{tot} is the total (thermal and non-thermal) velocity dispersion.

The H₂CO and CH₃CN lines were fitted to estimate the velocity dispersion σ_{obs} , as described in Section 3.2.1. Then, the channel width of $V_{\text{ch}} = 1.35 \text{ km s}^{-1}$ was subtracted quadratically to derive the deconvolved velocity dispersion:

$$\sigma_{\text{deconv}}^2 = \sigma_{\text{obs}}^2 - \left(\frac{V_{\text{ch}}}{2\sqrt{2 \ln 2}} \right)^2. \quad (4)$$

The total velocity dispersion, which includes the thermal and non-thermal components, was then derived following

$$\sigma_{\text{tot}}^2 = \sigma_{\text{NT}}^2 + c_s^2 = \left(\sigma_{\text{deconv}}^2 - \frac{k_B T_{\text{core}}}{\mu_{\text{mol}} m_H} \right) + \frac{k_B T_{\text{core}}}{\mu m_H}, \quad (5)$$

where the molecular weight μ_{mol} is 28 for H₂CO and 44 for CH₃CN.

Figure 5 shows the relation between the non-thermal velocity dispersion (σ_{NT}) and sound speed (c_s) of the cores in the three clouds. The Mach numbers of the cores are listed in Table 1, with their errors estimated from the error propagation. The mean Mach numbers in cloud e, Sgr C, and the 20 km s⁻¹ cloud are 3.2, 4.4 and 4.3, respectively, suggesting supersonic motions in the cores. The result confirms that the cores in the three clouds are subject to supersonic non-thermal motions (e.g., turbulence, infall, or rotation), which is the typical condition for gas in the CMZ (e.g., Rathborne et al. 2014).

3.3.3. Virial parameters

As shown in Section 3.2, 253 dense cores have sufficiently high S/N ratios in H₂CO or CH₃CN to estimate temperatures and velocity dispersions. We then performed virial analyses to assess dynamical states of these cores. We considered the contributions of kinetic energy (Ω_K), gravitational potential energy (Ω_G), and

external pressure (Ω_P) from surrounding gas in the virial equilibrium analysis.

Assuming a spherically symmetric Gaussian density distribution for the gravitational potential energy, the gravitational term (Ω_G) can be derived following (Bertoldi & McKee 1992):

$$\Omega_G = -\frac{3}{5}a \frac{GM_{\text{core}}^2}{R}, \quad (6)$$

where R is the effective core radius. We took the core area A_{core} from *astrodendro* and derived R following $R = \sqrt{A_{\text{core}}/\pi}$. The parameter a is a constant whose value depends on the power-law index of the radial density distribution $\rho \propto r^{-k_p}$, $a = (1 - k_p/3)/(1 - 2k_p/5)$. Here we took $k_p = 2$ and $a = 5/3$, which is the case for self-gravitating cores (Bertoldi & McKee 1992).

The kinetic energy of a core of mass M_{core} and one-dimensional (1D) velocity dispersion σ_{tot} is given by

$$\Omega_k = \frac{3}{2}M_{\text{core}}\sigma_{\text{tot}}^2. \quad (7)$$

Lastly, following e.g. Kirk et al. (2017) and Scibelli et al. (2023), the external pressure term Ω_P is given by

$$\Omega_P = -4\pi P_{\text{out}} R^3. \quad (8)$$

P_{out} is external pressure given by

$$P_{\text{out}} = \rho_{\text{out}} \sigma_{\text{tot,out}}^2 = \mu m_H n_{\text{out}} \sigma_{\text{tot,out}}^2, \quad (9)$$

where $\sigma_{\text{tot,out}}$ is thermal plus non-thermal velocity dispersion of the gas surrounding the core. We assumed that the cores are enveloped by gas at larger scales, as captured by the SMA observations at a resolution of 4'' in Lu et al. (2019b), and adopted the gas density n_{out} estimated using the SMA 1.3 mm continuum (assuming a dust temperature of 20 K) and the velocity dispersion $\sigma_{\text{tot,out}}$ from the SMA N₂H⁺ or CH₃OH lines (Lu et al. 2019b). The adopted values for the cores are listed in Table 1. Note that the SMA observations also suffered from the missing flux issue and filtered out spatially extended emission. However, such emission should represent more diffuse gas enclosing the gas component captured by the SMA, and thus not directly exerting pressure on the even small cores in the ALMA observations.

We considered the equilibrium between gravitational and kinetic energies

$$2\Omega_k + \Omega_G = 0, \quad (10)$$

and derived the virial parameter α_{vir} as

$$\alpha_{\text{vir}} = -\Omega_k/\Omega_G. \quad (11)$$

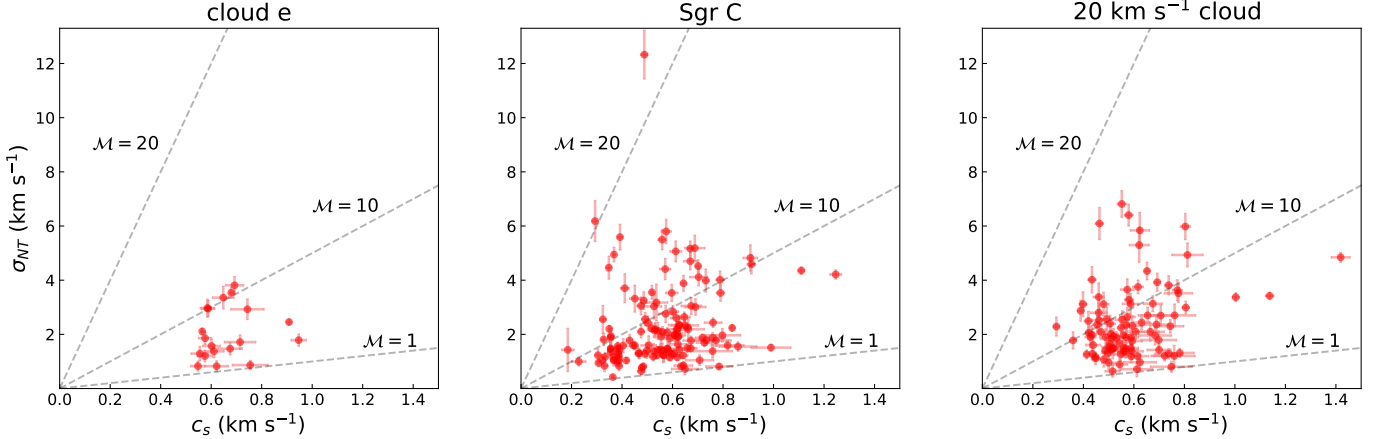


Figure 5. Comparisons between the non-thermal velocity dispersion (σ_{NT}) and the sound speed (c_s). The dashed gray lines represent Mach numbers $\mathcal{M} = 1, 10$, and 20 .

If α_{vir} is lower than the critical value of 2, a core would be gravitationally bound, otherwise it would be unbound (Kauffmann et al. 2013). Figure 6 depicts the distribution of the virial parameters of the dense cores within the three clouds, which the dashed horizontal line marks the critical value of 2. It can be seen that the majority of the dense cores (247/253) are in an unbound state.

If we additionally considered the contribution of external pressure

$$2\Omega_k + \Omega_G + \Omega_P = 0, \quad (12)$$

and then derived the virial parameter as

$$\alpha_{vir,p} = -\frac{\Omega_k}{\Omega_G + \Omega_P}. \quad (13)$$

We listed the virial parameters of the cores that take external pressure into account in Table 1, and plotted the results in Figure 7 (cf. Pattle et al. 2015; Kirk et al. 2017). Histograms of the virial parameters in the three individual clouds are shown in Figure 8.

As shown in Figure 7, taking the external pressure into account in the virial equilibrium leads to a greater number of cores being bound (154/253), including 10/19, 108/137, and 36/97 cores in cloud e, Sgr C, and the 20 km s⁻¹ cloud, respectively, characterized by $\alpha_{vir,p} < 2$. Moreover, the majority of the cores (239/253) have $\Omega_G/\Omega_P < 1$, indicating that the cores are predominantly confined by external pressure instead of self gravity, including 18/19, 134/137, 88/97 cores in cloud e, Sgr C, and the 20 km s⁻¹ cloud, respectively.

Our finding contrasts with results toward clouds in the Galactic disk, where most of the cores are already bound even without considering the contribution of external pressure in the virial equilibrium (e.g., Kauffmann

et al. 2013; Li et al. 2023b; Cheng et al. 2024), and reveals that non-thermal motions in the form of external pressure and internal support dominate gas dynamics in the spatial scale of individual cores (~ 2000 au). This result echoes with previous studies that highlight high pressure star forming environments in the CMZ on spatial scales of ~ 0.1 pc (Liu et al. 2013; Walker et al. 2018; Myers et al. 2022; Callanan et al. 2023) and $\sim 10^3$ AU (Williams et al. 2022).

3.4. Core Mass Functions

To fit a power law to the high-mass end of the CMF, we employed the maximum likelihood estimation (MLE) method (Clauset et al. 2009) implemented in the *plfit* package⁵, following the form

$$\frac{dN}{d \log M} \propto M^{-\alpha}. \quad (14)$$

The power-law index (α) and the lower limit of the power law relation (M_{min}) were simultaneously determined during the fitting (see e.g., Lu et al. 2020).

We fit the CMFs for each cloud as well as for the three clouds combined, as shown in Figure 9. Note that we have excluded those sources with $\alpha_{vir,p} > 2$ and therefore being unbound. In the end, 80, 245, and 410 cores were considered for cloud e, Sgr C, and the 20 km s⁻¹ cloud, respectively. The best-fit power-law indices α for each individual cloud are between 1.09 and 1.38. For the combined CMF of the three clouds, the best-fit α is 1.33 ± 0.14 . These power-law indices are higher than those reported in Lu et al. (2020), which were derived from CMFs of the same sample of dense cores, yet with an assumed universal dust temperature

⁵ <https://github.com/keflavich/plfit>

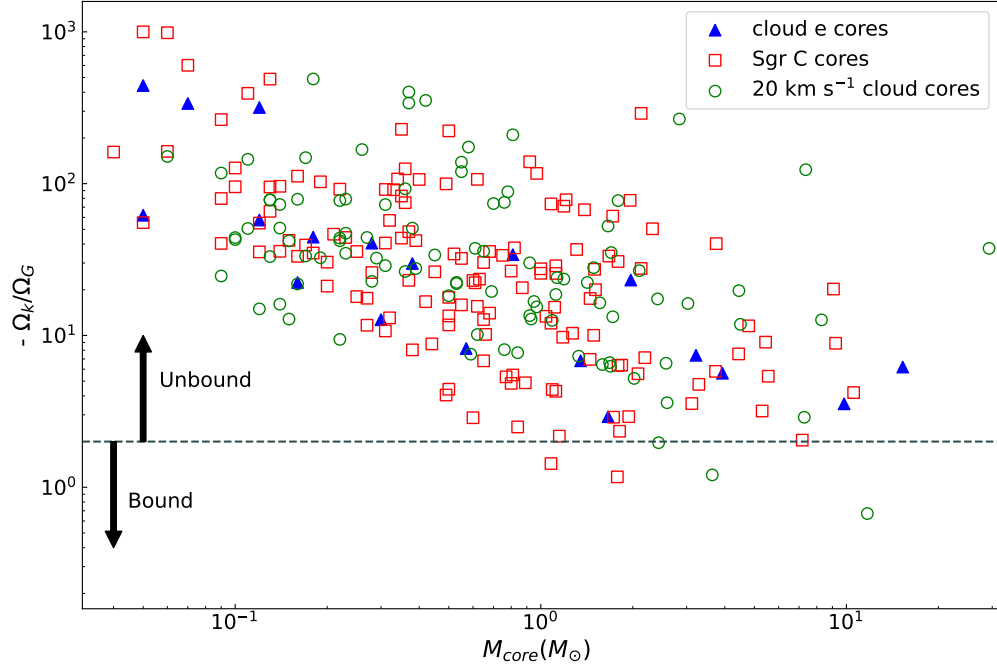


Figure 6. Distribution of masses and virial parameters of the cores, considering only gravitational and kinetic energies. The data points are color-coded by the clouds they belong to. Cores located above the dashed line ($\alpha_{\text{vir}} = -\Omega_k/\Omega_G = 2$) are considered to be unbound.

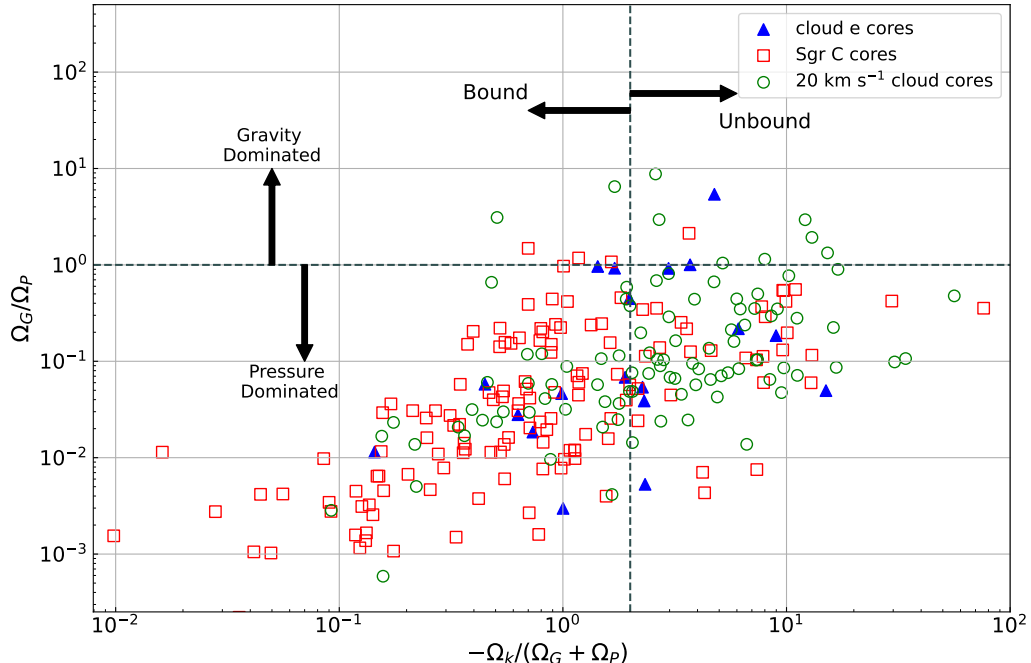


Figure 7. Virial parameters ($\alpha_{\text{vir},p}$) versus confinement ratios (Ω_G/Ω_P). Cores located above the horizontal dashed line ($\Omega_G/\Omega_P = 1$) are dominantly confined by gravity, while those below are dominantly confined by external pressure. Cores located to the left of the vertical dashed line $\alpha_{\text{vir},p} = -\Omega_k/(\Omega_G + \Omega_P) = 2$ are considered to be bound, while those to the right are unbound.

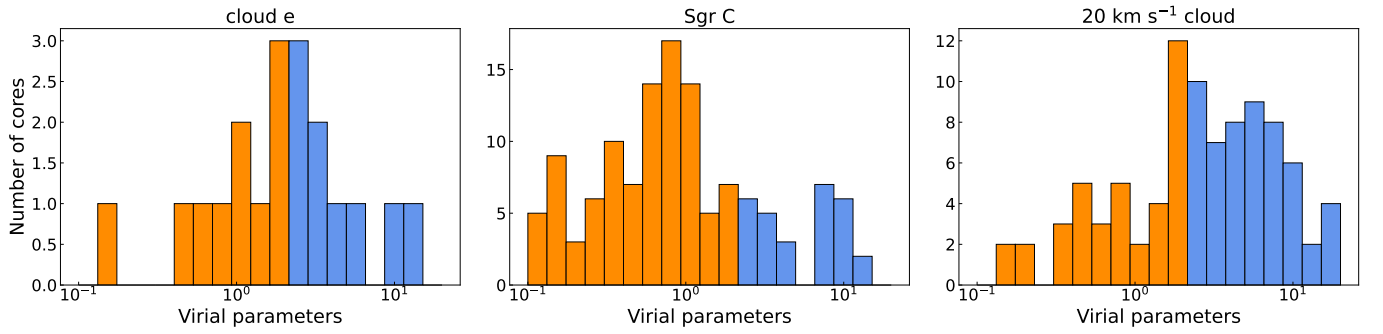


Figure 8. Histograms of virial parameters of the cores. The orange bars represent the portion of cores with virial parameter $\alpha_{\text{vir},p} = -\Omega_k/(\Omega_G + \Omega_p) < 2$, which are 10/19, 108/137, 36/97 in the cloud e, Sgr C, and the 20 km s^{-1} cloud, respectively.

of 20 K. In Appendix D, we conducted several tests, e.g., changing the assumed temperatures for the cores without H₂CO/CH₃CN line detections from 20 K to 30 K or 50 K, using the temperatures derived from the non-LTE method, and only using cores with temperatures estimated from the H₂CO/CH₃CN lines, and found that the CMFs consistently show higher power-law indices than those in Lu et al. (2020).

Figure 10 displays the cumulative distribution functions (CDFs) of core masses derived from a constant dust temperatures of 20 K (Lu et al. 2020) and from the updated core temperatures in the current work. The p -values of two-sample Kolmogorov-Smirnov (K-S) tests between the two CDFs are 0.63, 2.9×10^{-7} , and 0.01, for the three clouds respectively, and 2.9×10^{-9} for the three clouds combined. Usually when $p < 0.05$, one considers that the two samples in the K-S test are not drawn from the same distribution. As such, the core masses estimated with the updated temperatures do represent a statistically different distribution than those reported in Lu et al. (2020), except for cloud e where the number of cores is lower and therefore the statistics may not be robust.

We noted that the estimated power-law indices of the high-mass ends of the CMFs are consistent with that of the canonical IMF with $\alpha=1.35$ (Kroupa 2002). That is, the CMFs of the three clouds exhibit a Salpeter-like shape in their high-mass ends. The implications of these findings will be discussed in Section 4.2.

4. DISCUSSION

4.1. Dynamical states of the cores in different clouds

Figure 8 shows histograms of the virial parameters in the three clouds. The orange bars represent cores with virial parameters $\alpha_{\text{vir},p} < 2$, which are expected to be bound. Toward the three clouds, there are 10, 108, and 37 cores that fall within this bound state. These cores will likely collapse and form stars.

Meanwhile, the blue bars indicate that a large population of cores are unbound. As seen in Figures 7 & 8, even after considering the contribution of external pressure, there are still 9 out of the 19 cores in cloud e, 29 out of the 137 cores in Sgr C, and 61 out of the 97 cores in the 20 km s⁻¹ with $\alpha_{\text{vir},p} > 2$. The situation is more pronounced in the 20 km s⁻¹ cloud compared to Sgr C, while in cloud e there are not statistically enough cores with molecular line detection to reach a conclusion.

The different fractions of bound or unbound cores in Sgr C and the 20 km s⁻¹ cloud may reflect their different evolutionary phases regarding star formation, or different cloud-scale dynamics when they orbit around the Galactic Center. To discriminate between these scenar-

ios or explore other alternatives, a large sample of clouds in the CMZ at various evolutionary phases and orbital positions is needed to determine the viral states of dense cores. Our observations tentatively lend stronger support to the latter case:

- The estimate of the virial parameter is clearly affected by the measurement of velocity dispersions. When a core is associated with outflows, the velocity dispersion is likely to be overestimated because outflows broaden the H₂CO linewidth (H₂CO has been found to trace outflows in these clouds; Lu et al. 2021). Additionally, the presence of hot molecular cores, which are an advanced evolutionary phase of high-mass star formation, will also broaden the observed linewidth due to high temperatures (up to a few 10² K) and strong feedback. In such cases, the higher ratios of unbound to bound cores in the 20 km s⁻¹ cloud might suggest that star formation activities in the 20 km s⁻¹ cloud are more active than in Sgr C. However, this appears inconsistent with our observations. The number of outflows in the 20 km s⁻¹ cloud and Sgr C are 20 vs. 18, respectively, while the numbers of hot molecular cores (represented by cores with CH₃CN emission identified in the current work) are 12 vs. 17, respectively. These numbers are not significantly different. We conducted a test and found that after excluding cores associated with outflows and hot cores, the distribution of their virial parameters remained largely unchanged.

- The different positions and evolutionary stages of the two clouds in the CMZ may lead to different cloud-scale dynamics. The 20 km s⁻¹ cloud is closer to the center of gravitational potential in most of the 3D models of the CMZ (see Section 4.3.2 of Henshaw et al. 2023) and therefore is expected to experience stronger tidal effects than Sgr C. In certain models (e.g., Kruijssen et al. 2015), the 20 km s⁻¹ cloud may have recently passed or will soon pass through the pericenter of an elliptical orbit, which results in a strong tidal effect. This tidal compression would drive turbulence and deform the cloud, during which transient substructures such as unbound over-densities may emerge. These substructures are not the usually bound dense cores, but are sometimes referred to as ‘starless cores’ and will disperse over a few dynamical timescales (Offner et al. 2022).

In this sense, the upcoming ALMA CMZ Exploration Survey (ACES) results, which have systematically surveyed the CMZ in continuum emission and molecular

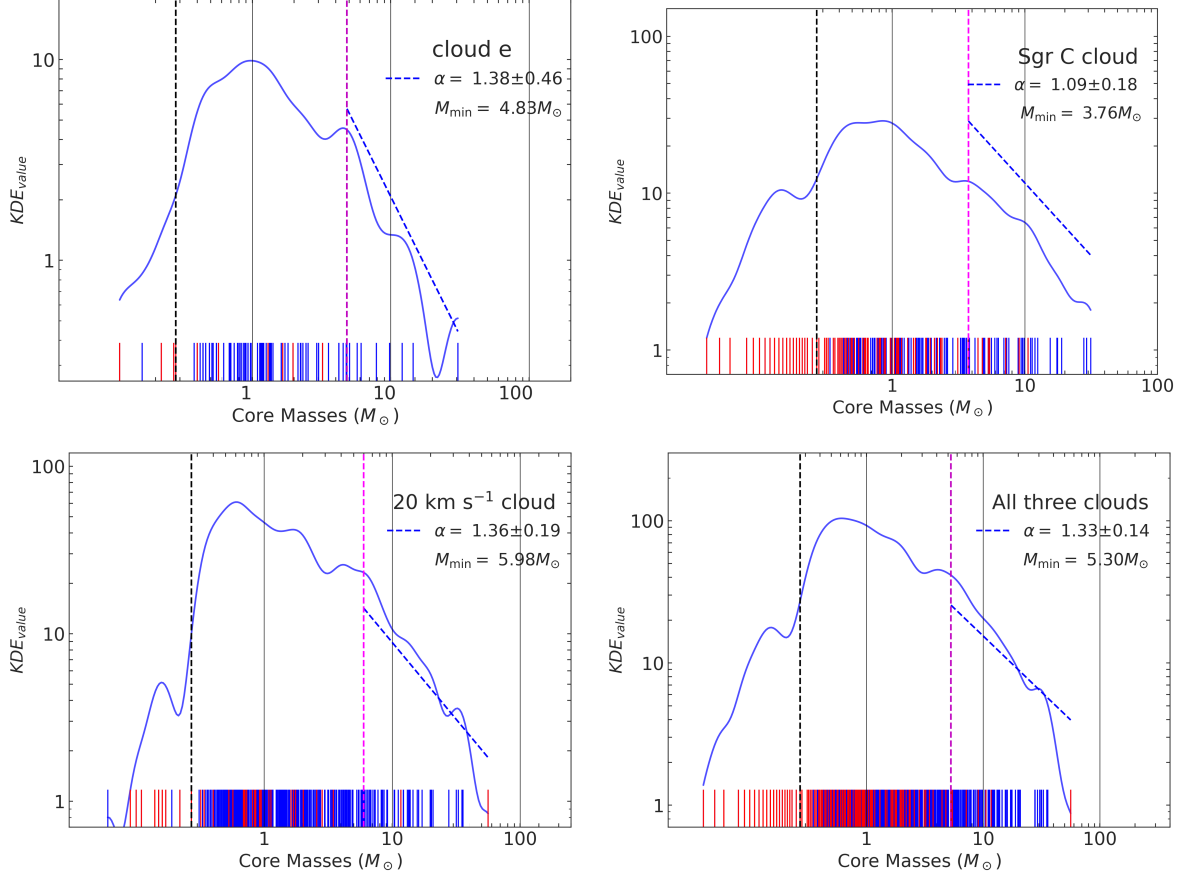


Figure 9. CMFs for the three individual clouds and the three clouds combined. The blue curves represent the kernel density estimations (KDEs) of the core masses. The red sticks attached to the bottom horizontal axes denote the core masses obtained with best-fit temperatures from H₂CO or CH₃CN, while the blue ones represent the core masses assuming a dust temperature of 20 K. The black vertical dashed lines represent the 5σ mass sensitivity ($0.27 M_{\odot}$) at a dust temperature of 20 K. The magenta vertical dashed lines represent the minimum core masses of the power-law fittings as determined by *plfit*, and the slanted blue dashed lines represent the best-fit power-law relations with an arbitrary normalization. Note that we choose not to plot histograms of core masses, because we do not bin the masses to fit the power-law, but carry out the power-law fitting using all the actual data above the minimum core masses following the MLE method.

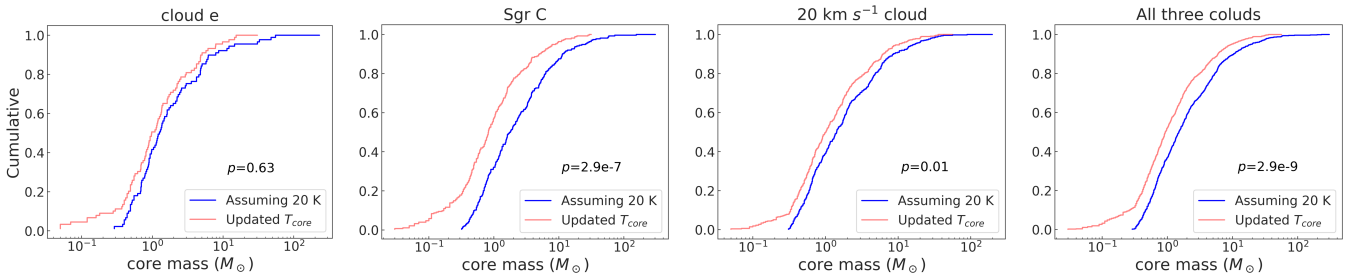


Figure 10. Cumulative distributions of the core masses in the current work and from Lu et al. (2020). The blue curves represent the cumulative mass distributions assuming a dust temperature of 20 K for all cores. The red curves represent the mass distributions with partially updated temperatures from fitting H₂CO and CH₃CN lines. The p -values of the two-sample K-S tests between the cumulative distributions are displayed in the bottom-right corners of the panels.

lines in the 3 mm band at a resolution of $\sim 2''$, will be critical to discerning evolutionary phases and star formation states of clouds in the CMZ and exploring the origin of the different fractions of bound vs. unbound cores.

4.2. Comparing the CMFs and the IMF in the CMZ

In this study, we have updated the temperatures and therefore the masses of 19, 137, and 97 cores in cloud e, Sgr C, and the 20 km s^{-1} cloud, respectively, by fitting the H₂CO or CH₃CN lines. Figure 1 shows that the cores with H₂CO or CH₃CN line emission are usually bright in the 1.3 mm continuum emission. In Lu et al. (2020), when a universal dust temperature of 20 K was assumed, these cores were estimated to be massive and populate the high-mass ends of the CMFs. With the updated temperatures, their masses become lower, and thus the high-mass ends of the CMFs become steeper and become consistent with the shape of the Salpeter-like IMF, as presented in Section 3.4.

Additionally, Figure D1 illustrates that when the minimum masses of the power-law fitting are fixed to the same values in Lu et al. (2020), the power-law indices remain to be higher than those reported in Lu et al. (2020). Meanwhile, to verify the reliability of the data, we test the CMFs composed only of cores with the best-fit temperatures from the H₂CO or CH₃CN lines, as shown in Figure D4. For each of the clouds, the number of cores is too low for a robust statistical result. For the three clouds combined, we again found a Salpeter-like shape in the high-mass end.

Therefore, using the updated core temperatures, the three clouds present a Salpeter-like slope in the high-mass end of their CMFs ($\alpha \sim 1.35$). This changes the conclusion of top-heavy CMFs in Lu et al. (2020), and highlights the importance of obtaining reliable core temperatures when fitting the CMFs (Dell’Ova et al. 2024).

The Salpeter-like CMFs observed in the three CMZ clouds aligns with several recent findings toward clouds in the Galactic disk (e.g., Cao et al. 2021; Suárez et al. 2021; Pouteau et al. 2023), where Salpeter-like CMFs are also detected. However, unlike the Galactic disk where the IMF is found to be universally consistent with the Salpeter shape, the young massive star clusters in the CMZ are suggested to present top-heavy IMFs (Hußmann et al. 2012; Hosek et al. 2019), although it can also be explained by tidal stripping of lower-mass stars (Park et al. 2020).

There have been debates on the inconsistency between CMFs and IMFs observed toward clouds in the Galactic disk, where the IMFs have the Salpeter-like slope in the high-mass end yet the CMFs sometimes are top-heavy

(e.g., Zhang et al. 2015; Motte et al. 2018; Sanhueza et al. 2019; Cheng et al. 2024; Louvet et al. 2024). These results question the direct mapping between the CMF and the IMF, and may suggest a picture of dynamic evolution of core masses through active gas accretion that gradually converges the shape of the CMF to that of the IMF (Pouteau et al. 2023; Cheng et al. 2024). In this study, the inconsistency possibly persists but the shapes of the two mass functions are reversed: the IMFs may be top-heavy, while the CMFs are found to be Salpeter-like. The implication is similar to the studies toward the Galactic disk regions: gas accretion into the cores as well as fragmentation may continuously change the shape of the CMF (e.g, more active accretion toward more massive cores: Bonnell et al. 1998, 2001; more efficient Jeans fragmentation of denser cores: Larson 2005; Elmegreen et al. 2008), which may eventually lead to a top-heavy IMF.

4.3. Caveats and perspectives

We raise several caveats of our study:

- Core identification: It has been shown that the parameters used in astrodendro affect the outcome of core identification and therefore the shape of CMFs (Lu et al. 2020). The algorithm adopted for the core identification (e.g., dendrogram vs. getsf) also has an impact on the derived CMFs (Cheng et al. 2024).
- Decoupled gas and dust temperatures: In the Galactic Center environment, the gas temperature and dust temperature are not necessarily well coupled. For example, in shocked regions in the 20 km s^{-1} cloud, an enhanced gas temperature has been observed (Lu et al. 2017), yet shock heating and pressure-volume work may not efficiently heat dust on >2000 AU scales. If a core is not internally heated by protostars, it may be possible that the gas temperature is higher than the dust temperature because of shock heating. In Appendix C, we carry out a simple test to compare the H₂CO emission that is or is not associated with the cores as traced by the 1.3 mm continuum, and find that the H₂CO compact sources spatially associated with the cores present lower temperatures than the other sample that are presumably heated by shocks. Therefore, the H₂CO gas in the cores seems to less affected by shock heating, although the possibility cannot be completely excluded.
- Overestimation of the velocity dispersions: As discussed in Section 3.2.1, outflows traced by H₂CO

and hot cores traced by CH₃CN exist in the three clouds, which broaden the observed velocity dispersion and lead to overestimation of the virial parameters. In Figure 8, the few cores with virial parameters greater than 10 may be heavily contaminated by outflows or hot cores. Note that several commonly used tracers of dense gas in cores, such as N₂H⁺, may be subject to the high ionization in the CMZ and therefore not well correlated with dense cores (Santa-Maria et al. 2021). A careful selection of appropriate molecular lines that are correlated with dense gas in the cores and are less effected by outflows should be carried out, which will be the subject of next papers of the series.

- Incomplete temperature measurements in the cores: In Section 3.2.1, we have updated the temperatures of a subset of the cores using the H₂CO and CH₃CN lines, which results in a steeper slope for the high-mass ends of the CMFs. The remaining cores do not present sufficient S/N ratios in the H₂CO or CH₃CN lines, yet many of them are found to be bound in Section 3.3.3 and therefore could be already forming stars and be heated internally. Their temperatures, as a result, could be higher than the assumed 20 K, and then the core masses could be overestimated, although the temperatures cannot be too high (otherwise molecular transitions such as H₂CO and CH₃CN should have been excited). The impact on the shape of the CMFs is an issue to be explored, should we obtain multiple-band continuum data in the future to construct dust spectral energy distributions and more robustly measure dust temperatures in the cores.

5. CONCLUSIONS

In this study, we investigate gas dynamics and CMFs of dense cores within three massive clouds in the CMZ using our ALMA 1.3 mm continuum and spectral line observations at 2000-AU resolution. We estimate temperatures and velocity dispersions using the H₂CO or CH₃CN lines for a total of 253 cores in the cloud e (19 out of 89), Sgr C (137 out of 274), and the 20 km s⁻¹ cloud (97 out of 471). Then we evaluate their virial equilibrium taking external pressure into consideration, and revisit their CMFs using the newly derived core temperatures as well as excluding unbound sources. Our main findings are:

- The high Mach numbers in the cores ($\mathcal{M} \sim 3\text{--}4$) suggest the existence of supersonic non-thermal motions down to small spatial scales of 2000 AU.

- In the extreme environment of the CMZ, the contribution of external pressure is critical for the virial equilibrium of the cores, without which most of the cores would be unbound. This differs from the situation of the cores in the Galactic disk where gas is already bound even without considering external pressure.

ACKNOWLEDGMENTS

X.L. acknowledges support from the National Key R&D Program of China (No. 2022YFA1603101), the Strategic Priority Research Program of the Chinese Academy of Sciences (CAS) Grant No. XDB0800300, the National Natural Science Foundation of China (NSFC) through grant Nos. 12273090 and 12322305, the Natural Science Foundation of Shanghai (No. 23ZR1482100), and the CAS “Light of West China” Program No. xbzg-zdsys-202212. A.G. acknowledges support from the National Science Foundation (NSF) under grants AAG 2008101 and 2206511 and CAREER 2142300. Y.C. was partially supported by a Grant-in-Aid for Scientific Research (KAKENHI number JP24K17103) of the JSPS. H.B.L. is supported by the National Science and Technology Council (NSTC) of Taiwan (Grant Nos. 111-2112-M-110-022-MY3, 113-2112-M-110-022-MY3). Q.Z. acknowledges support from the NSF under Award No. 2206512. C.B. gratefully acknowledges funding from the NSF under Award Nos. 2108938, 2206510, and CAREER 2145689, as well as from the National Aeronautics and Space Administration through the Astrophysics Data Analysis Program under Award “3-D MC: Mapping Circumnuclear Molecular Clouds from X-ray to Radio,” Grant No. 80NSSC22K1125. This paper makes use of the following ALMA data: ADS/JAO.ALMA#2016.1.00243.S. ALMA is a partnership of ESO (representing its member states), NSF (USA), and NINS (Japan), together with NRC (Canada), MOST and ASIAA (Taiwan), and KASI (Republic of Korea), in cooperation with the Republic of Chile. The Joint ALMA Observatory is operated by ESO, AUI/NRAO, and NAOJ. This research has made use of NASA’s Astrophysics Data System.

Facility: ALMA

Software: CASA (McMullin et al. 2007; CASA Team et al. 2022), APLpy (Robitaille & Bressert 2012), Astropy (Astropy Collaboration et al. 2013, 2018, 2022), XCLASS (Möller et al. 2017).

Table 1. Parameters of the cores and their H₂CO and CH₃CN lines.

Core ID	RA and Dec	Flux	R	T _{H₂CO}	T _{H₂CO}	T _{CH₃CN}	T	σ _{H₂CO}	σ _{H₂CO}	σ _{CH₃CN}	σ	M _{core}	\mathcal{M}	α _{vir,p}
		density		LTE	non-LTE	LTE		LTE	non-LTE	LTE				
(J2000)		(mJy)	(AU)	(K)	(K)	(K)	(K)	(km s ⁻¹)	(km s ⁻¹)	(km s ⁻¹)	(km s ⁻¹)	(M_{\odot})		
(1)	(2)	(3)	(4)	(5)	(6)	(7)	(8)	(9)	(10)	(11)	(12)	(13)	(14)	(15)
cloud e														
1	17:46:47.19, -28:32:16.93	0.46	1200	-	-	-	-	-	-	-	0.69	-	-	
2	17:46:46.98, -28:32:14.43	0.48	1320	-	-	-	-	-	-	-	0.68	-	-	
3	17:46:48.39, -28:32:10.31	4.07	2250	-	-	-	-	-	-	-	6.12	-	-	
4	17:46:47.05, -28:32:09.91	0.72	1500	138.3±49.7	83±21	-	138.3±49.7	3.86±0.32	4.32±0.63	-	3.86±0.32	0.12	5.50±0.55	15.01
5	17:46:47.07, -28:32:08.93	21.53	3950	69.2±14.7	73±0.5	94.4±9.7	94.4±9.7	2.73±0.25	1.36±0.24	3.02±0.19	3.02±0.19	3.93	5.21±0.29	4.76
6	17:46:47.01, -28:32:08.88	0.25	1150	-	-	-	-	-	-	-	0.79	-	-	
7	17:46:46.93, -28:32:08.57	0.2	1030	95.4±34.6	70±5.5	-	95.4±34.6	1.34±0.19	1.34±0.42	-	1.34±0.19	0.05	2.09±0.38	2.31
8	17:46:47.07, -28:32:07.26	152.95	8160	-	-	237.9±16.8	237.9±16.8	-	-	2.53±0.1	2.53±0.1	15.29	2.70±0.12	2.97
9	17:46:46.95, -28:32:08.02	1.77	1820	-	-	-	-	-	-	-	2.53	-	-	
10	17:46:46.91, -28:32:07.58	1.1	1600	-	-	-	-	-	-	-	1.72	-	-	
Sgr C														
1	17:44:41.38, -29:28:29.90	19.33	4620	125.1±20.3	140±7	-	125.1±20.3	2.34±0.1	2.18±0.32	-	2.34±0.1	4.79	3.43±0.18	0.54
2	17:44:41.32, -29:28:30.03	0.34	1360	88±28	101±63	-	<89.1	1.56±0.2	1.27±0.37	-	1.56±0.2	<0.09	2.61±0.41	0.26
3	17:44:40.81, -29:28:27.70	0.37	1290	-	-	-	-	-	-	-	0.84	-	-	
4	17:44:41.21, -29:28:26.84	1.1	2330	113.5±42.8	125±16	-	113.5±42.8	1.56±0.18	1.43±0.53	-	1.56±0.18	0.31	2.30±0.33	0.13
5	17:44:41.20, -29:28:23.94	0.61	1680	43.8±7.4	63±39	-	43.5±7.3	1.24±0.14	1.02±0.28	-	1.24±0.14	0.50	3.02±0.41	0.31
6	17:44:40.76, -29:28:19.77	0.36	1370	-	-	-	-	-	-	-	0.77	-	-	
7	17:44:40.79, -29:28:19.50	1.15	1310	26.8±7.1	26±26	-	<89.9	1.36±0.21	1.35±0.31	-	1.36±0.21	>0.32	4.04±0.78	0.52
8	17:44:40.78, -29:28:19.09	1.14	1310	73.7±31.2	130±12	-	<99.5	1.7±0.33	1.53±0.63	-	1.7±0.33	>0.28	3.15±0.72	0.35
9	17:44:40.68, -29:28:19.20	0.43	1440	-	-	-	-	-	-	-	0.90	-	-	
10	17:44:40.73, -29:28:19.01	0.25	1150	-	-	-	-	-	-	-	0.54	-	-	
20 km s ⁻¹ cloud														
1	17:45:36.41, -29:06:30.01	0.4	1290	-	-	-	-	-	-	-	0.71	-	-	
2	17:45:36.53, -29:06:29.63	0.27	1040	-	-	-	-	-	-	-	0.36	-	-	
3	17:45:36.53, -29:06:29.38	0.33	1240	-	-	-	-	-	-	-	0.51	-	-	
4	17:45:36.23, -29:06:29.28	0.34	1330	-	-	-	-	-	-	-	0.55	-	-	
5	17:45:36.27, -29:06:28.57	0.25	1360	-	-	-	-	-	-	-	0.52	-	-	
6	17:45:36.64, -29:06:26.83	0.86	1720	101.5±49.7	125±61	-	101.5±49.7	2.39±0.37	2.99±0.96	-	2.39±0.37	0.21	3.90±0.70	6.12
7	17:45:36.34, -29:06:26.57	0.26	1200	-	-	-	-	-	-	-	0.42	-	-	
8	17:45:36.70, -29:06:24.69	0.5	1790	61.2±20.4	69.1±3.1	-	61.2±20.4	3.43±0.51	3±1	-	3.43±0.51	0.21	7.34±1.18	11.18
9	17:45:36.41, -29:06:24.27	0.33	1590	-	-	-	-	-	-	-	0.71	-	-	
10	17:45:36.31, -29:06:23.97	0.35	1290	-	-	-	-	-	-	-	0.46	-	-	

NOTE.—The table lists physical parameters of the first 10 dense cores from each of the three clouds complete lists are shown in Tables E1, E2. Columns (2), (3), and (4) present the coordinates, 1.3 mm continuum flux density, and effective radius of the cores, respectively, as determined by astrodendro (Lu et al. 2020). Columns (5) to (7) show temperatures from the LTE fitting of H₂CO, the non-LTE fitting of H₂CO, and the LTE fitting of CH₃CN using EMANON. Column (8) lists the adopted temperature. Columns (9) to (11) correspond to the velocity dispersions from different approaches, and column (12) shows the adopted value. The masses, Mach numbers, and virial parameters of the cores are presented in columns (13), (14), and (15).

APPENDIX

A. FITTING RESULTS OF THE H₂CO AND CH₃CN LINES

The left panel in Figure A1 illustrates the fitting results of the H₂CO lines using the LTE method to 233 cores, including 16, 127, and 90 cores in cloud e, Sgr C, and the 20 km s⁻¹ cloud, respectively. The right panel shows the corresponding fitting results from the non-LTE method. Note that Figure A1 includes H₂CO fitting results of the cores with CH₃CN detections as well.

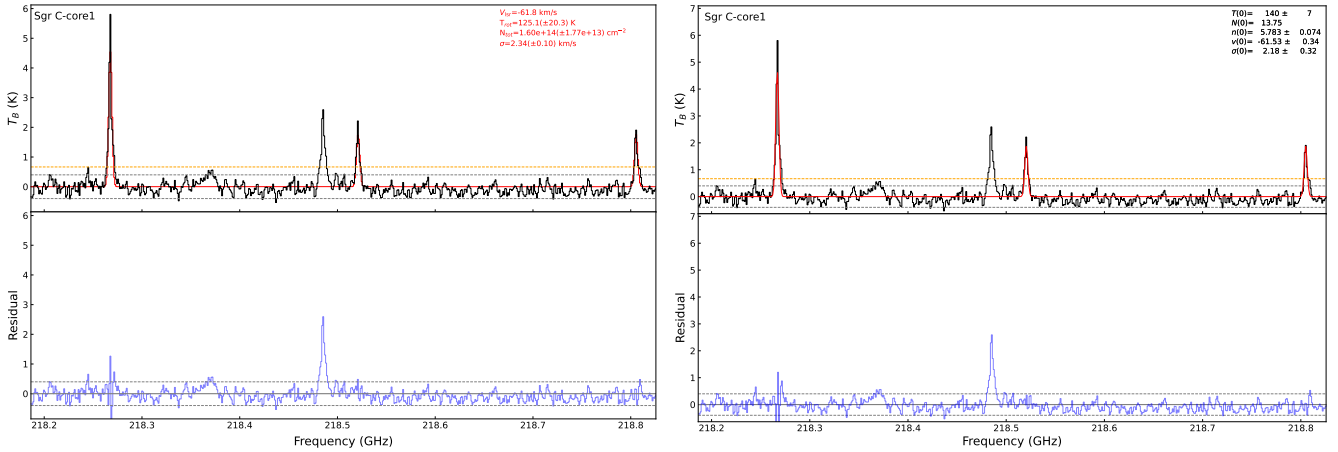


Figure A1. The LTE and non-LTE fitting results towards one core are presented here. The complete figure set (466 images) is available in the online journal.

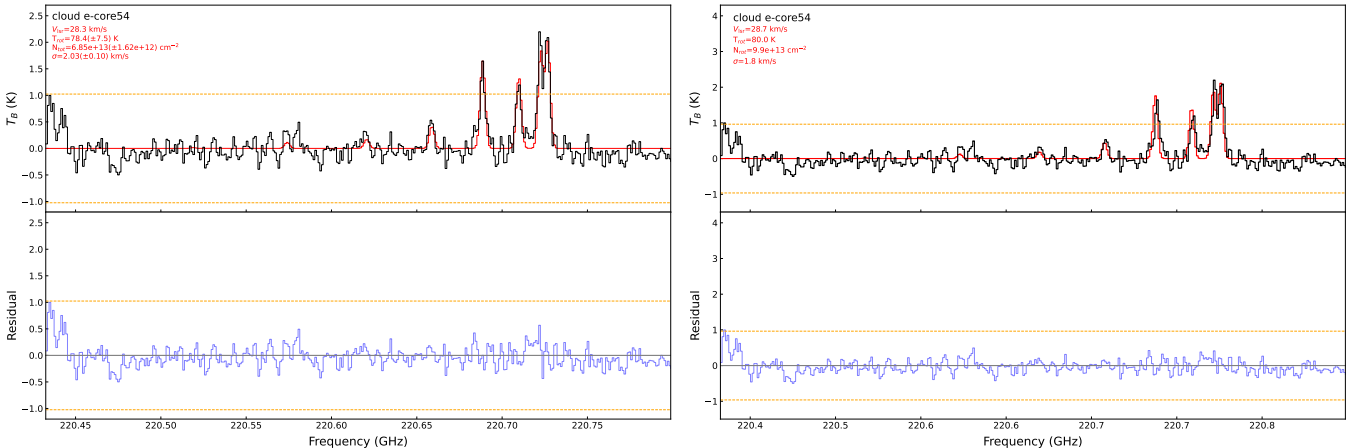


Figure A2. The LTE fitting results using the EMANON code and XCLASS towards one core are presented here. The complete figure set (66 images) is available in the online journal.

Figure A2 depicts the LTE fittings of CH₃CN lines to 33 cores, including 4, 17, and 12 cores in cloud e, Sgr C, and the 20 km s⁻¹ cloud, respectively. The left and right panels show the fitting results using the EMANON code and the XCLASS package, respectively.

Figure A3 shows histograms of temperatures and velocity dispersions of the cores with H₂CO spectra detected, comparing the LTE and non-LTE methods.

Figure A4 presents results from the LTE and non-LTE approaches employed for fitting the temperature and velocity dispersion using the H₂CO lines. We observed a general consistency in the fitted temperatures and velocity dispersions

between the two approaches. Note that under the assumption of LTE, we have assumed that the best-fit H₂CO rotational temperature equals the kinetic temperature.

In Figure A5, we compared temperatures derived using the two LTE approaches with CH₃CN lines. The results show that the temperatures are consistent within the fitting errors.

Figure A6 shows that the temperatures and velocity dispersions of the cores derived from CH₃CN are generally higher than those derived from H₂CO (through forced fitting despite the self absorption). This may be because CH₃CN traces inner parts of a core where the gas is hotter and more turbulent due to stronger feedback from embedded protostars.

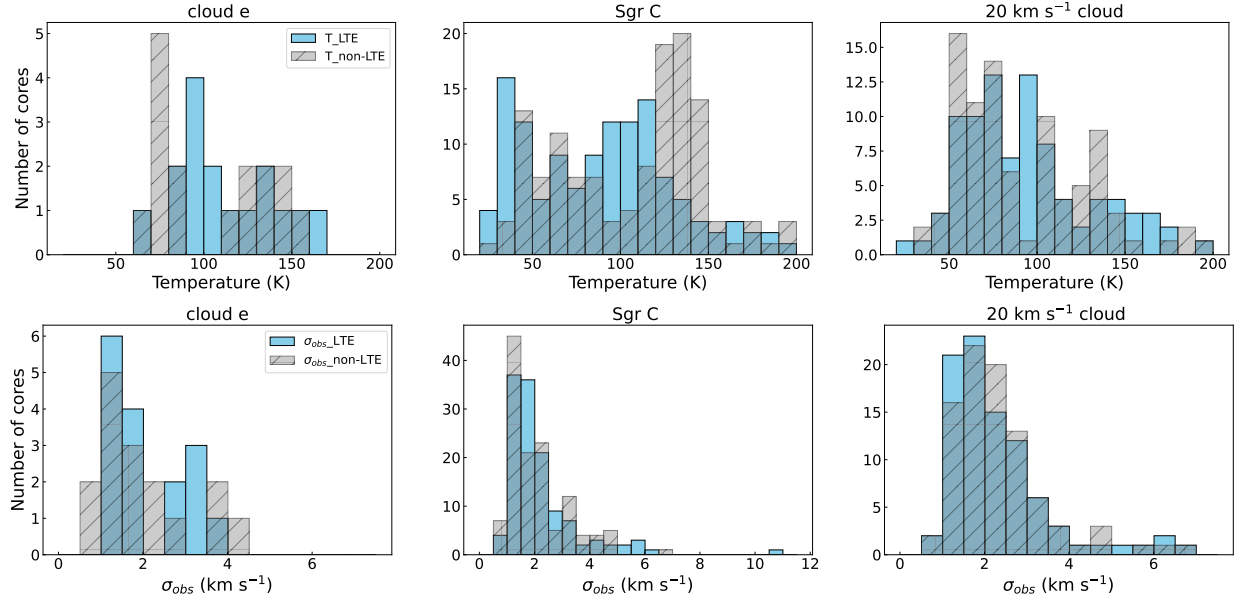


Figure A3. Histograms of temperatures and velocity dispersions. The upper panel shows the temperatures, and the lower panels show the velocity dispersions. The blue bars represent the LTE fitting results, while the striped grey bars represent the non-LTE fitting results.

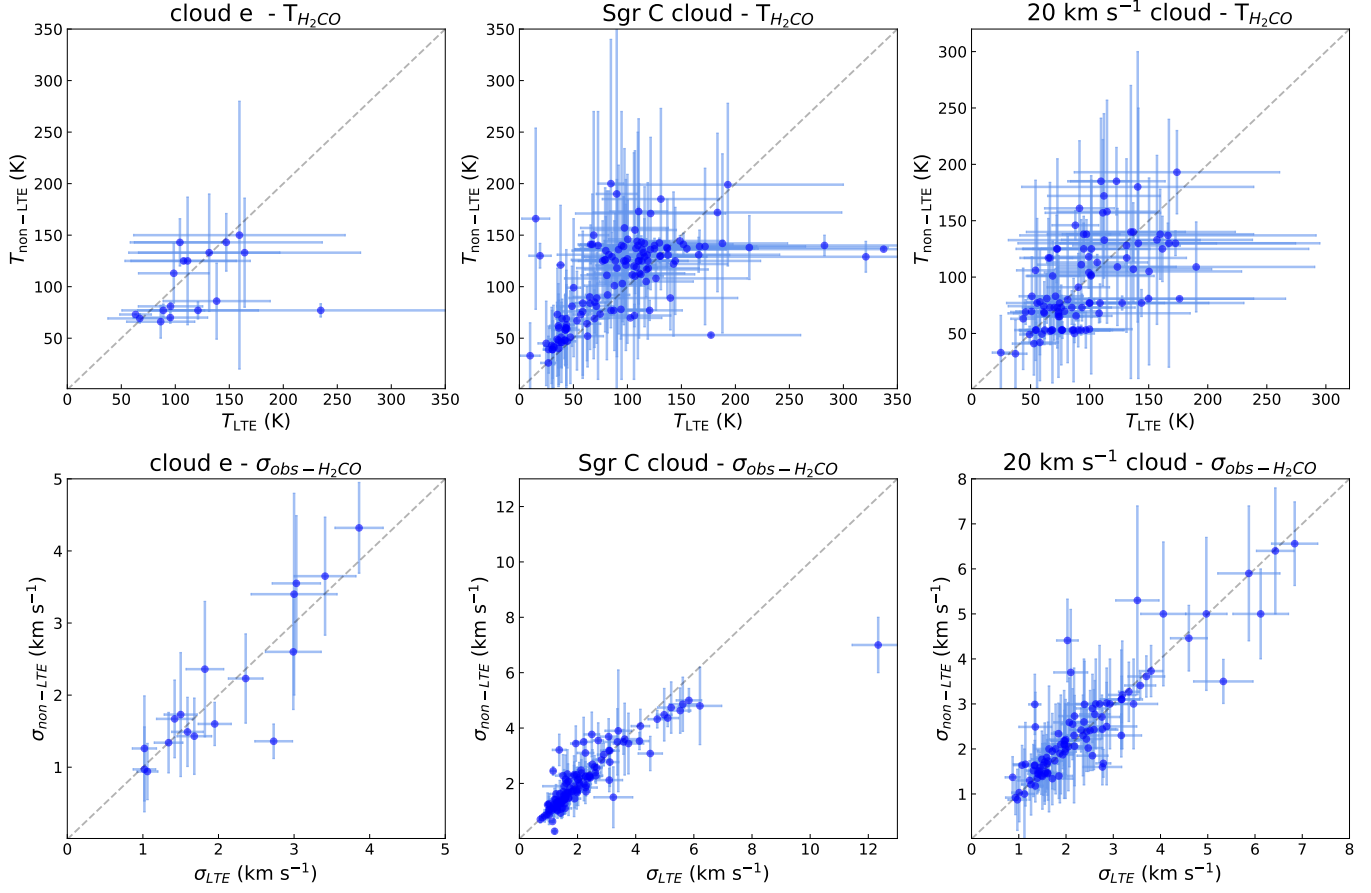


Figure A4. The upper panels show the correlation between the core temperatures in the three clouds derived from H_2CO under LTE and non-LTE assumptions, while the lower panels depict the correlation for the velocity dispersions. The blue dots with error bars represent the best-fit values, and the dashed diagonal lines represent where the two fitting results are equal.

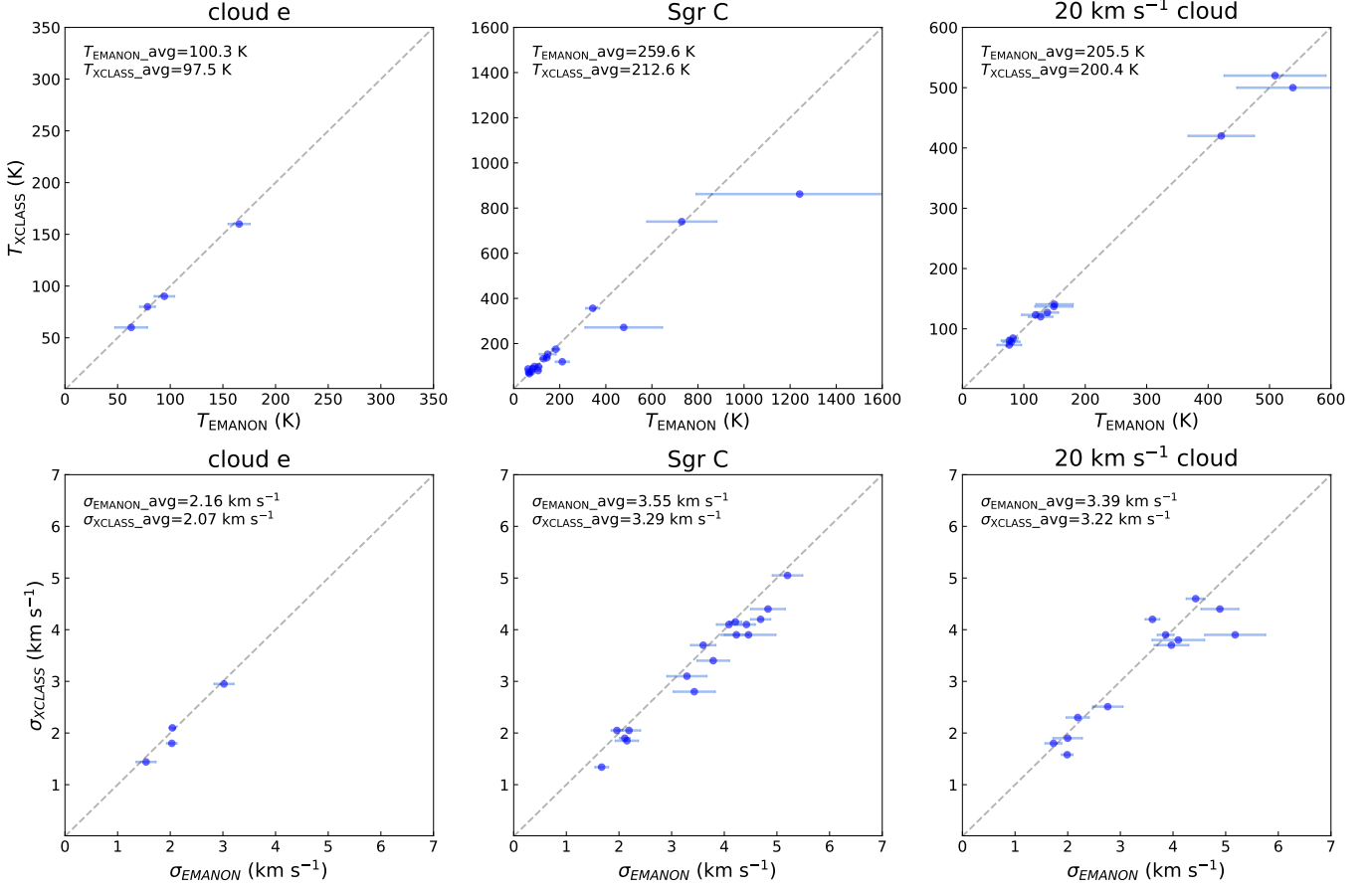


Figure A5. The upper panels show the correlation between the temperatures of the cores in the three clouds derived from CH₃CN under LTE conditions using the EMANON code vs. XCLASS, while the lower panels depict the correlation for the velocity dispersions. The symbols are the same as in Figure A4, except that XCLASS fits do not output errors so vertical error bars are not plotted.

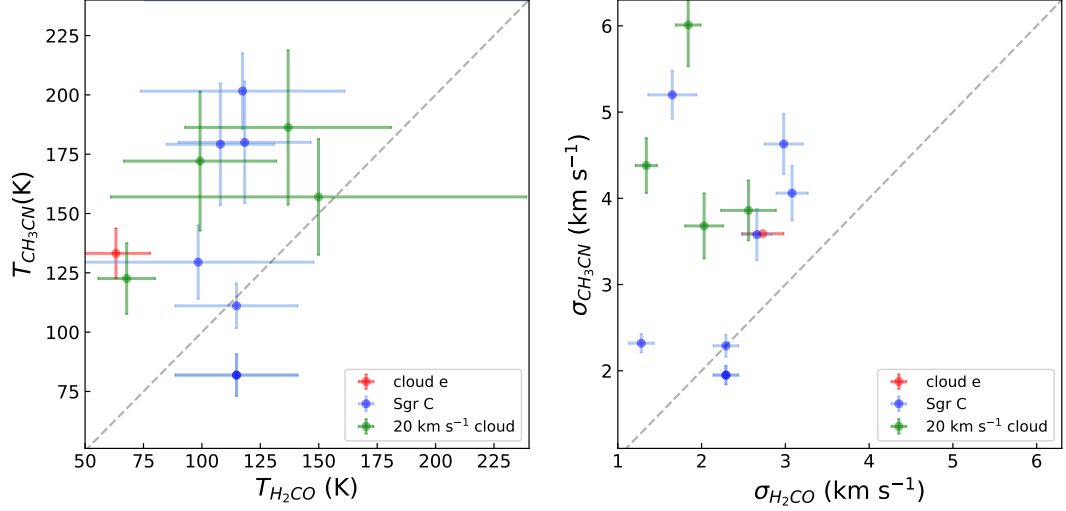


Figure A6. The left panel shows the correlation between the core temperatures in the three clouds derived from H₂CO and CH₃CN under LTE assumptions, while the right panel depicts the correlation for the velocity dispersions. The blue dots with error bars represent the best-fit values, and the dashed diagonal lines indicate where the fitting results are equal.

B. H₂CO LINE RATIO-TEMPERATURE RELATION

In Section 3.2.1, when only H₂CO_{3,0,3}–_{2,0,2} line is detected (above the 5σ level) in a core (i.e., scenario ii), we use the 3σ value as the upper limit for the peak intensities of H₂CO_{3,2,2}–_{2,2,1} and _{3,2,1}–_{2,2,0} lines, and derive the upper limit for the line ratio between these two transitions and the _{3,0,3}–_{2,0,2} transition. Then we collect all the cases where the _{3,0,3}–_{2,0,2} line plus at least one of _{3,2,2}–_{2,2,1} and _{3,2,1}–_{2,2,0} lines are detected (i.e., scenario i), and fit their line ratios and temperature to derive a line ratio-temperature relation, as shown in Figure B1. The relation between the line ratio (LR) and the temperature (T) follows:

$$T = 67.9 \exp(0.8LR), \quad (\text{B1})$$

which is then used to convert the line ratios to temperatures for scenario ii.

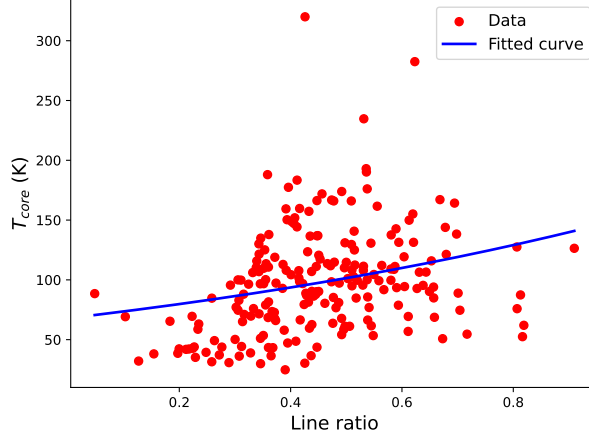


Figure B1. H₂CO line ratio-temperature relation map.

C. CORRELATION BETWEEN THE CORES AND H₂CO GAS

As discussed in Section 3.1, the H₂CO line emission is not necessarily associated with the cores traced by the 1.3 mm continuum. To test how well the H₂CO emission and the 1.3 mm continuum emission are correlated, we select the C1 clump in the 20 km s⁻¹ cloud as an example, where apparent spatially extended H₂CO emission is seen. We use astrodendro to identify 96 compact sources in the integrated intensity map of the H₂CO _{3,0,3}–_{2,0,2} line. Then we clarify them into those associated with the dense cores ('core-related') and those not ('core-unrelated'), which consist of 10 and 86 compact sources, respectively, and fit the H₂CO lines. However, 67 out of these sources cannot be fit because their _{3,0,3}–_{2,0,2} peak intensities are below 5σ . Figure C1 shows best-fit temperatures and velocity dispersions of the compact sources where LTE fittings can be carried out. The core-related compact sources clearly present lower temperatures than core-unrelated ones.

We further run K-S tests on the temperatures and velocity dispersions of the two samples. As shown in Figure C2, the p value of the K-S test on the temperatures is 0.068, suggesting a marginally significant difference between the core-related and core-unrelated compact sources. However, the difference in velocity dispersions is not statistically significant given the high p value.

Therefore, the H₂CO emission spatially not associated with the cores may indeed represent a hotter gas component than the dense gas in the cores. Meanwhile, whether H₂CO detected toward the cores solely traces dense gas remains uncertain, although it may present statistically different temperatures than the core-unrelated component.

D. TESTS ON THE CORE MASS FUNCTIONS

We carry out a series of tests on the CMFs, most of which are about different assumptions on the dust temperature. In all cases, the power-law indices of the high-mass ends of the CMFs remain to be higher than those derived in Lu et al. (2020) and close to 1.35.

Figure D1 shows the CMFs for the three individual clouds and the three clouds combined, adopting the core temperatures derived in Section 3.2 and fixing the minimum masses for the power-law fit to the same ones in Lu et al.

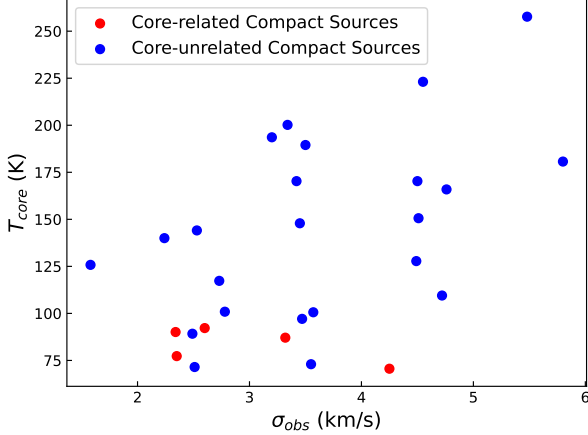


Figure C1. Temperatures and velocity dispersions of the H₂CO compact sources. The red points represent the core-related H₂CO compact sources, while the blue points indicate the core-unrelated ones.

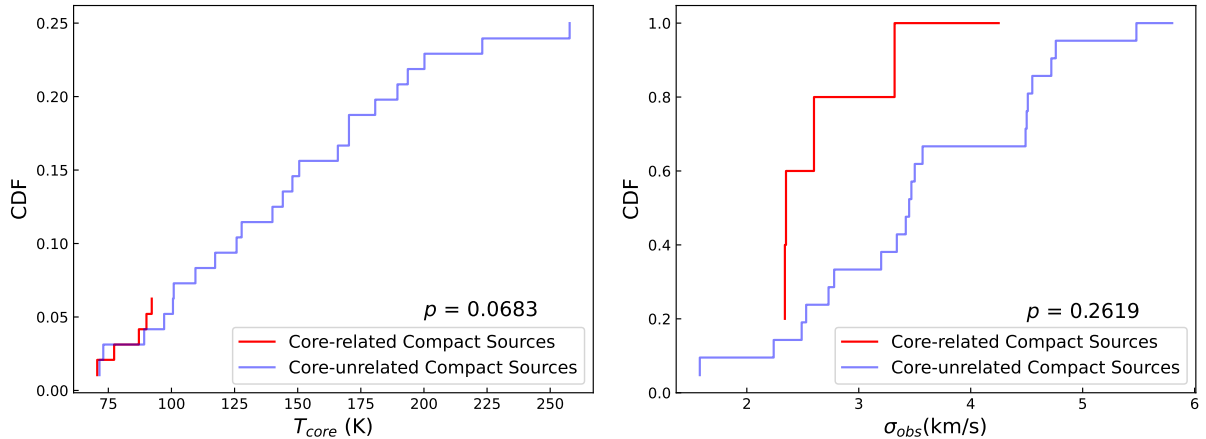


Figure C2. The left panel shows the cumulative distribution of temperatures for both core-related and core-unrelated H₂CO compact sources, while the right panel shows the cumulative distribution of velocity dispersions.

(2020). This demonstrates that the higher power-law indices in this work are not a result of different minimum masses in the fit.

Figure D2 shows the CMFs for the three individual clouds and the three clouds combined, where core temperatures derived in Section 3.2 are used, and for cores without H₂CO or CH₃CN detections, core temperatures of 30 K are adopted. Similarly, Figure D3 shows the case where core temperatures of 50 K are adopted when H₂CO or CH₃CN lines are not detected. The power law indices are higher than those reported in Lu et al. (2020) and can be up to ~ 2 .

Figure D4 shows the CMFs for the three individual clouds and the three clouds combined, adopting the core temperatures derived in Section 3.2. Here we only include the core masses with updated temperatures, and perform the power-law fitting to the high-mass ends of the CMFs following the same approach as in Section 3.4. For the three clouds combined, one finds a Salpeter-like shape in the high-mass end of the CMF. We note that this test does not imply a new selection criteria that only considers warmer or hotter cores with H₂CO and/or CH₃CN emission, but only illustrates that the CMF shape is not affected by excluding the colder cores in Figure 9.

We also test whether adopting the core temperatures derived from non-LTE fits of the H₂CO lines has any effect on the slope of the CMFs. Figure D5 demonstrates that the results are consistent with those in Figure 9.

Lastly, we carry out a Monte Carlo experiment by varying the core temperatures within their corresponding uncertainty ranges, and regenerating the core masses and the CMFs 80000 times. As shown in Figure D6, the power law indices of the CMFs of the three clouds show Gaussian distributions around mean values of 1.2–1.4, consistent with being Salpeter-like.

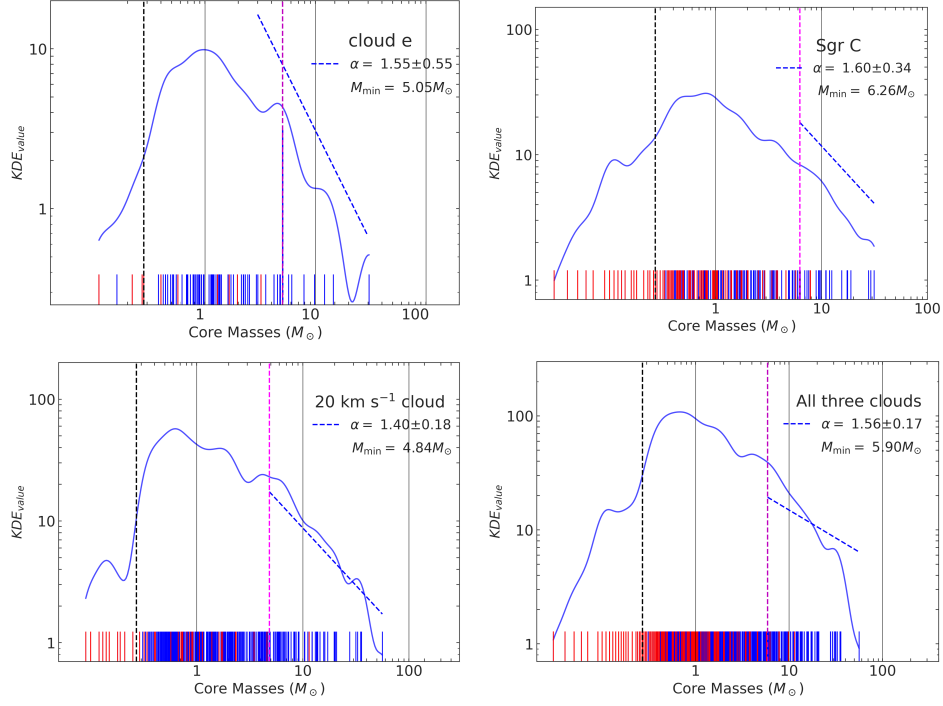


Figure D1. The CMFs for the three individual clouds and the three clouds combined after fixing the minimum mass for the power-law fit. The symbols in the figures are the same as in Figure 9.

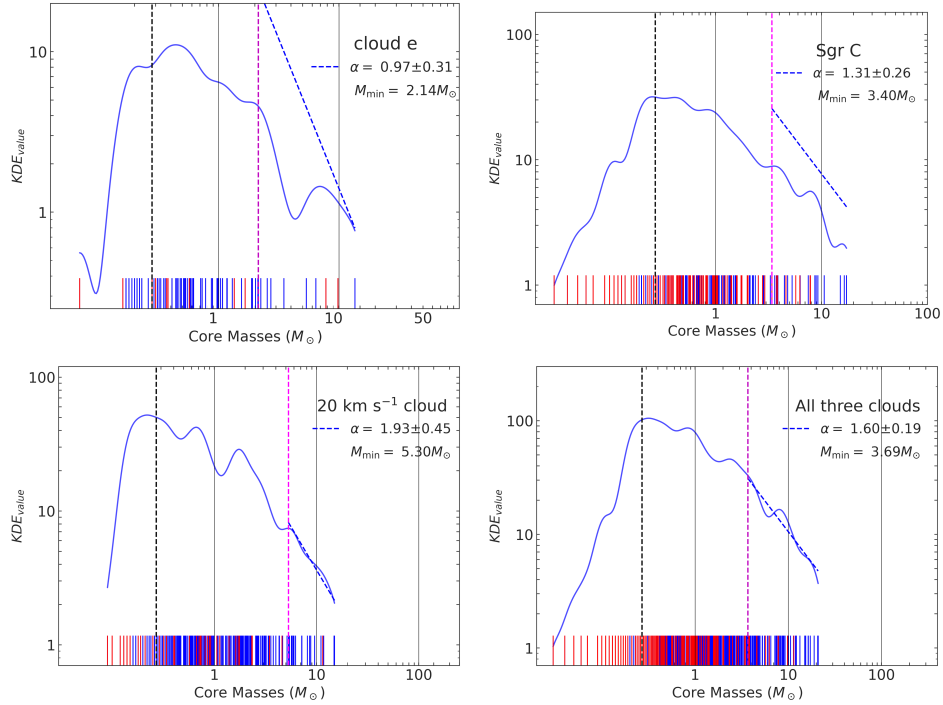


Figure D2. The CMFs for the three individual clouds and the three clouds combined, with core temperatures of 30 K adopted for those without H₂CO or CH₃CN detections. The symbols in the figures are the same as in Figure 9.

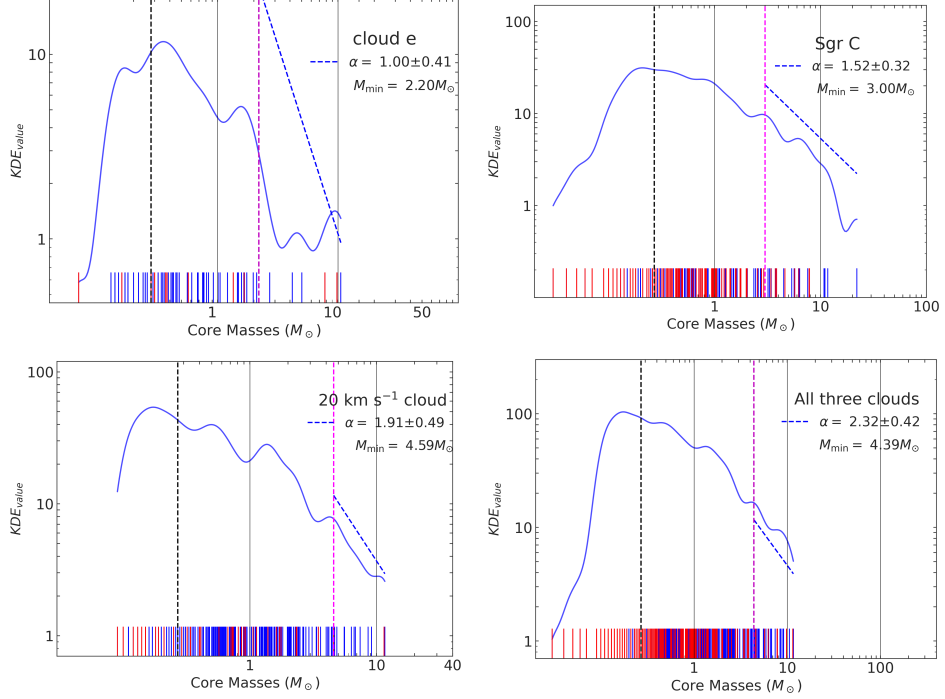


Figure D3. The CMFs for the three individual clouds and the three clouds combined, with core temperatures of 50 K adopted for those without H₂CO or CH₃CN detections. The symbols in the figures are the same as in Figure 9.

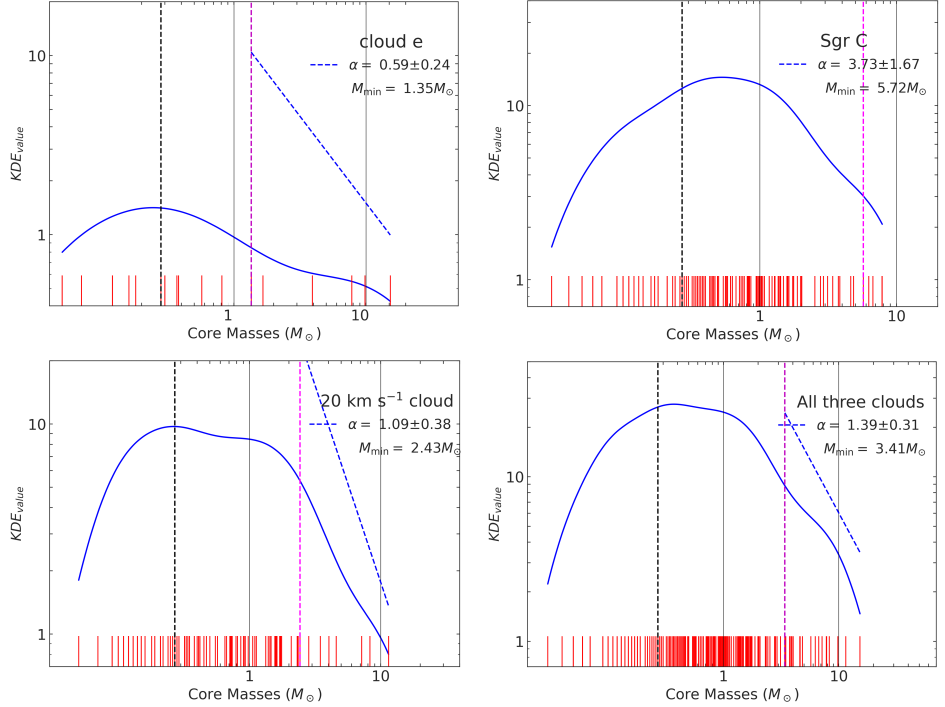


Figure D4. The CMFs for the three individual clouds and the three clouds combined, with only the core masses derived from best-fit temperatures using H₂CO or CH₃CN lines. The symbols in the figures are the same as in Figure 9.

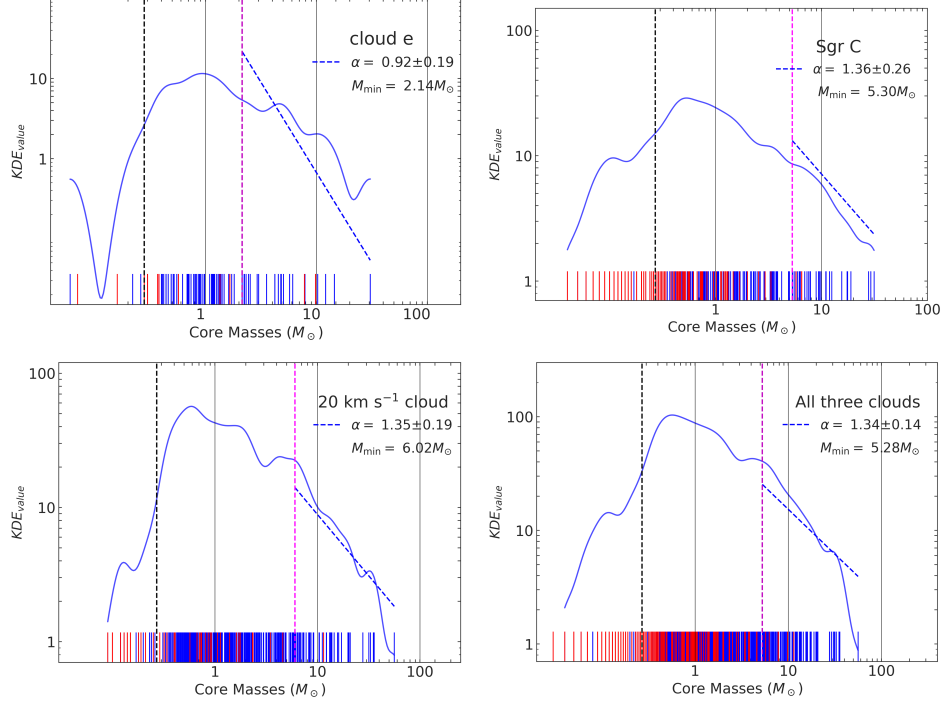


Figure D5. The CMFs for the three individual clouds and the three clouds combined, with core temperatures derived from the non-LTE fitting of H₂CO instead of from the LTE fitting, otherwise the core masses are identical to those in Figure 9. The symbols in the figures are the same as in Figure 9.

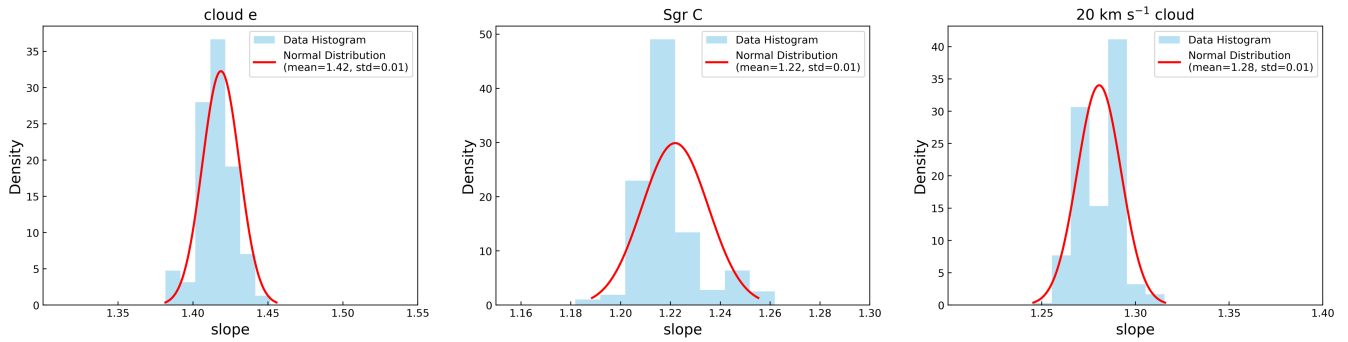


Figure D6. Distribution of the slopes of the CMFs in the three molecular clouds from Monte Carlo tests. The blue bars represent the data points and the red curves represent the Gaussian fits. The mean and standard deviation of each cloud are shown in the upper right corner of each panel.

E. FULL CORE CATALOGS

The following three tables list properties of the cores in cloud e, Sgr C, and the 20 km s⁻¹ cloud. The data columns are the same as those in Table 1.

Table E1. Properties of the cores in cloud e.

Core ID	RA and Dec	Flux	R	T _{H₂} CO	T _{H₂} CO	T _{CH₃CN}	T	σ _{H₂} CO	σ _{H₂} CO	σ _{CH₃CN}	σ	M _{core}	M	α _{vir,p}
(1)	(J2000)	(mJy)	(AU)	(K)	(K)	(K)	(K)	(km s ⁻¹)	(km s ⁻¹)	(km s ⁻¹)	(km s ⁻¹)	(M _⊕)	(14)	(15)
		density	LTE	non-LTE	LTE			LTE	non-LTE	LTE				
1	17:46:47.19, -28:32:16.93	0.46	1200	-	-	-	-	-	-	-	-	0.69	-	-
2	17:46:46.98, -28:32:14.43	0.48	1320	-	-	-	-	-	-	-	-	0.68	-	-
3	17:46:48.39, -28:32:10.31	4.07	2250	-	-	-	-	-	-	-	-	6.12	-	-
4	17:46:47.05, -28:32:09.91	0.72	1500	138.3±49.7	83±21	-	138.3±49.7	3.86±0.32	4.32±0.63	-	3.86±0.32	0.12	5.50±0.55	15.01
5	17:46:47.07, -28:32:08.93	21.53	3950	69.2±14.7	73±0.5	94.4±9.7	94.4±9.7	2.73±0.25	1.36±0.24	3.02±0.19	3.02±0.19	3.93	5.21±0.29	4.76
6	17:46:47.01, -28:32:08.88	0.25	1150	-	-	-	-	-	-	-	-	0.79	-	-
7	17:46:46.93, -28:32:08.57	0.2	1030	95.4±34.6	70±5.5	-	95.4±34.6	1.34±0.19	1.34±0.42	-	1.34±0.19	0.05	2.09±0.38	2.31
8	17:46:47.07, -28:32:07.26	152.95	8160	-	-	165.4±10.5	165.4±10.5	-	-	2.04±0.06	2.04±0.06	15.29	2.70±0.12	2.97
9	17:46:46.95, -28:32:08.02	1.77	1820	-	-	-	-	-	-	-	-	2.53	-	-
10	17:46:46.91, -28:32:07.58	1.1	1600	-	-	-	-	-	-	-	-	1.72	-	-
11	17:46:47.60, -28:32:07.73	0.72	1610	-	-	-	-	-	-	-	-	1.09	-	-
12	17:46:47.60, -28:32:07.17	0.3	1240	-	-	-	-	-	-	-	-	0.44	-	-
13	17:46:46.93, -28:32:07.03	0.91	1800	131.4±65.5	133±58	-	131.4±65.5	1.59±0.21	1.49±0.48	-	1.59±0.21	0.18	2.18±0.37	2.27
14	17:46:47.10, -28:32:06.46	0.45	1080	95.6±29.9	80.9±4.1	-	95.6±29.9	1.95±0.22	1.6±0.3	-	1.95±0.22	0.12	3.22±0.43	8.98
15	17:46:48.28, -28:32:06.08	0.32	1090	-	-	-	-	-	-	-	-	0.49	-	-
16	17:46:46.88, -28:32:05.84	7.54	2650	111.4±58.1	117±45	-	111.4±58.1	1.02±0.16	1.21±0.62	-	1.02±0.16	1.66	1.33±0.33	1.43
17	17:46:46.94, -28:32:05.45	20.34	3880	-	-	-	-	-	-	-	-	30.58	-	-
18	17:46:47.12, -28:32:05.35	0.27	1380	-	-	-	-	-	-	-	-	0.70	-	-
19	17:46:47.06, -28:32:05.29	0.56	1320	-	-	-	-	-	-	-	-	0.83	-	-
20	17:46:47.16, -28:32:04.53	3.04	1950	-	-	-	-	-	-	-	-	4.54	-	-
21	17:46:47.20, -28:32:04.53	0.61	1330	-	-	-	-	-	-	-	-	0.89	-	-
22	17:46:47.71, -28:32:04.09	1.94	2330	-	-	-	-	-	-	-	-	2.92	-	-
23	17:46:47.14, -28:32:03.87	0.26	1150	-	-	-	-	-	-	-	-	0.40	-	-
24	17:46:46.66, -28:32:03.64	3.21	2910	-	-	-	-	-	-	-	-	4.83	-	-
25	17:46:47.77, -28:32:03.59	0.74	1810	-	-	-	-	-	-	-	-	1.15	-	-
26	17:46:46.78, -28:32:03.37	0.34	1250	-	-	-	-	-	-	-	-	0.52	-	-
27	17:46:46.75, -28:32:03.09	0.31	1170	-	-	-	-	-	-	-	-	0.49	-	-
28	17:46:46.78, -28:32:02.78	0.62	1740	-	-	-	-	-	-	-	-	0.93	-	-
29	17:46:46.62, -28:32:02.67	1.45	1640	-	-	-	-	-	-	-	-	2.14	-	-
30	17:46:47.41, -28:32:02.54	1.08	2270	86.5±31.6	66±16	-	<99.0	1.02±0.15	0.97±0.59	-	1.02±0.15	<0.27	1.51±0.35	0.14
31	17:46:48.21, -28:32:02.36	1.17	1370	-	-	-	-	-	-	-	-	1.81	-	-
32	17:46:48.23, -28:32:02.13	9.64	2310	-	-	-	-	-	-	-	-	14.51	-	-
33	17:46:46.61, -28:32:02.19	1.05	1310	-	-	-	-	-	-	-	-	-	-	-
34	17:46:46.65, -28:32:02.10	1.1	1340	-	-	-	-	-	-	-	-	1.62	-	-
35	17:46:46.58, -28:32:01.75	2.86	1990	-	-	-	-	-	-	-	-	4.22	-	-
36	17:46:47.59, -28:32:01.85	0.4	1530	159.4±98	150±130	-	<91.5	2.99±0.37	2.6±0.8	-	2.99±0.37	<0.11	3.94±0.62	1.00
37	17:46:46.74, -28:32:01.70	0.39	1520	-	-	-	-	-	-	-	-	0.62	-	-
38	17:46:47.02, -28:32:01.63	0.35	1380	-	-	-	-	-	-	-	-	0.55	-	-
39	17:46:47.54, -28:32:01.19	2.81	2560	-	-	-	-	-	-	-	-	4.22	-	-
40	17:46:46.55, -28:32:01.34	0.92	1440	-	-	-	-	-	-	-	-	1.36	-	-
41	17:46:46.64, -28:32:01.00	0.34	1290	-	-	-	-	-	-	-	-	0.51	-	-
42	17:46:47.18, -28:32:00.75	0.26	1270	-	-	-	-	-	-	-	-	0.42	-	-
43	17:46:47.21, -28:32:00.52	0.33	1200	-	-	-	-	-	-	-	-	0.55	-	-
44	17:46:46.40, -28:32:00.39	3.91	2080	164.2±107.4	133±53	-	164.2±107.4	1.06±0.14	0.94±0.39	-	1.06±0.14	0.57	1.15±0.25	0.45
45	17:46:46.57, -28:32:00.29	0.83	2100	-	-	-	-	-	-	-	-	1.26	-	-
46	17:46:47.22, -28:32:00.21	0.43	1290	-	-	-	-	-	-	-	-	0.69	-	-
47	17:46:46.34, -28:32:00.08	2.02	1940	-	-	-	-	-	-	-	-	3.01	-	-
48	17:46:47.17, -28:31:59.75	0.54	1410	-	-	-	-	-	-	-	-	0.93	-	-
49	17:46:47.31, -28:31:59.59	0.93	1630	-	-	-	-	-	-	-	-	1.37	-	-
50	17:46:46.47, -28:31:59.55	0.69	1780	-	-	-	-	-	-	-	-	0.98	-	-
51	17:46:46.11, -28:31:59.47	1.47	1940	-	-	-	-	-	-	-	-	2.24	-	-
52	17:46:47.21, -28:31:59.46	0.56	1150	-	-	-	-	-	-	-	-	0.88	-	-
53	17:46:46.02, -28:31:59.25	1.55	2060	-	-	-	-	-	-	-	-	2.32	-	-
54	17:46:46.30, -28:31:58.69	36.54	4320	-	-	78.4±7.5	78.4±7.5	-	-	2.03±0.10	2.03±0.10	9.83	3.74±0.21	1.70
55	17:46:47.32, -28:31:59.16	1.33	1810	107.7±48.9	139.0±45.0	-	107.7±48.9	1.5±0.22	1.71±0.83	-	1.5±0.22	1.97	2.25±0.42	0.63

Table E1 *continued*

Table E1 (*continued*)

Core ID	RA and Dec	Flux	R	$T_{\text{H}_2\text{CO}}$	$T_{\text{H}_2\text{CO}}$	$T_{\text{CH}_3\text{CN}}$	T	$\sigma_{\text{H}_2\text{CO}}$	$\sigma_{\text{H}_2\text{CO}}$	$\sigma_{\text{CH}_3\text{CN}}$	σ	M_{core}	\mathcal{M}	$\alpha_{\text{vir,p}}$
		density		LTE	non-LTE	LTE		LTE	non-LTE	LTE				
(1)	(J2000)	(mJy)	(AU)	(K)	(K)	(K)	(K)	(km s $^{-1}$)	(km s $^{-1}$)	(km s $^{-1}$)	(km s $^{-1}$)	(M_{\odot})	(14)	(15)
(2)	(2)	(3)	(4)	(5)	(6)	(7)	(8)	(9)	(10)	(11)	(12)	(13)	(14)	(15)
56	17:46:47.22, -28:31:58.89	8.03	2560	-	-	-	-	-	-	-	-	12.11	-	-
57	17:46:46.25, -28:31:59.11	4.06	1630	-	-	62.9 \pm 15.5	62.9 \pm 15.5	-	-	1.54 \pm 0.19	1.54 \pm 0.19	0.38	1.89 \pm 0.24	1.90
58	17:46:46.15, -28:31:58.96	0.31	1120	-	-	-	-	-	-	-	-	0.46	-	-
59	17:46:47.33, -28:31:58.57	0.87	1830	-	-	-	-	-	-	-	-	1.33	-	-
60	17:46:46.36, -28:31:58.63	3.36	1690	-	-	-	-	-	-	-	-	5.05	-	-
61	17:46:47.20, -28:31:57.78	1.61	2000	-	-	-	-	-	-	-	-	2.44	-	-
62	17:46:46.27, -28:31:57.08	1.75	1940	147.2 \pm 89	143 \pm 28	-	147.2 \pm 89	1.82 \pm 0.25	2.36 \pm 0.94	-	1.82 \pm 0.25	0.28	2.40 \pm 0.43	0.73
63	17:46:47.09, -28:31:57.04	0.66	1700	-	-	-	-	-	-	-	-	0.97	-	-
64	17:46:46.98, -28:31:56.63	0.53	1590	-	-	-	-	-	-	-	-	0.81	-	-
65	17:46:46.34, -28:31:56.58	0.27	1120	121 \pm 56	77 \pm 7.2	-	121 \pm 56	3.41 \pm 0.41	3.65 \pm 0.82	-	3.41 \pm 0.41	0.05	5.18 \pm 0.73	2.33
66	17:46:46.88, -28:31:56.26	2.32	2760	-	-	-	-	-	-	-	-	3.55	-	-
67	17:46:46.23, -28:31:56.33	0.67	1270	88.9 \pm 38.4	77 \pm 6.2	-	88.9 \pm 38.4	1.42 \pm 0.24	1.67 \pm 0.54	-	1.42 \pm 0.24	0.16	2.32 \pm 0.50	0.99
68	17:46:46.23, -28:31:55.32	31.67	3770	99.7 \pm 31.7	77 \pm 8.6	-	99.7 \pm 31.7	3.01 \pm 0.3	2.23 \pm 0.61	-	3.01 \pm 0.3	3.22	5.02 \pm 0.57	3.71
69	17:46:45.41, -28:31:55.84	0.34	1270	-	-	-	-	-	-	-	-	0.49	-	-
70	17:46:46.28, -28:31:54.98	3.29	1780	98.6 \pm 32.7	113 \pm 19	-	98.6 \pm 32.7	3.03 \pm 0.32	3.55 \pm 0.94	-	3.03 \pm 0.32	0.81	5.08 \pm 0.61	6.09
71	17:46:46.85, -28:31:54.96	0.27	1110	-	-	-	-	-	-	-	-	0.40	-	-
72	17:46:47.04, -28:31:54.39	5.22	3480	-	-	-	-	-	-	-	-	7.89	-	-
73	17:46:46.23, -28:31:54.51	5.78	1920	104.3 \pm 42.2	143 \pm 23	-	104.3 \pm 42.2	1.68 \pm 0.23	1.43 \pm 0.53	-	1.68 \pm 0.23	1.35	2.61 \pm 0.44	1.98
74	17:46:45.30, -28:31:52.46	0.88	1690	-	-	-	-	-	-	-	-	1.30	-	-
75	17:46:45.46, -28:31:51.38	0.8	1880	-	-	-	-	-	-	-	-	1.19	-	-
76	17:46:46.63, -28:31:51.07	0.76	1700	-	-	-	-	-	-	-	-	1.13	-	-
77	17:46:45.17, -28:31:50.66	0.54	1320	-	-	-	-	-	-	-	-	0.78	-	-
78	17:46:45.43, -28:31:50.03	0.78	1850	-	-	-	-	-	-	-	-	1.17	-	-
79	17:46:45.24, -28:31:49.74	3.81	2500	-	-	-	-	-	-	-	-	5.73	-	-
80	17:46:45.23, -28:31:49.07	1.31	2670	-	-	-	-	-	-	-	-	4.78	-	-
81	17:46:45.55, -28:31:48.75	0.67	2060	-	-	-	-	-	-	-	-	1.41	-	-
82	17:46:45.33, -28:31:48.67	0.93	1440	-	-	-	-	-	-	-	-	0.90	-	-
83	17:46:45.61, -28:31:48.49	0.8	1810	-	-	-	-	-	-	-	-	1.21	-	-
84	17:46:45.49, -28:31:48.10	1.49	2430	-	-	-	-	-	-	-	-	2.23	-	-
85	17:46:45.71, -28:31:46.56	0.28	1120	-	-	-	-	-	-	-	-	0.44	-	-
86	17:46:45.19, -28:31:44.73	0.56	1330	-	-	-	-	-	-	-	-	0.86	-	-
87	17:46:44.97, -28:31:43.60	1.07	1520	-	-	-	-	-	-	-	-	1.62	-	-
88	17:46:45.09, -28:31:40.42	3.17	2640	-	-	-	-	-	-	-	-	4.78	-	-
89	17:46:45.05, -28:31:40.13	0.5	1120	-	-	-	-	-	-	-	-	0.74	-	-

Table E2. Properties of the cores in Sgr C.

Core ID	RA and Dec	Flux	R	$T_{\text{H}_2\text{CO}}$	$T_{\text{H}_2\text{CO}}$	$T_{\text{CH}_3\text{CN}}$	T	$\sigma_{\text{H}_2\text{CO}}$	$\sigma_{\text{H}_2\text{CO}}$	$\sigma_{\text{CH}_3\text{CN}}$	σ	M_{core}	\mathcal{M}	$\alpha_{\text{vir,p}}$
		density		LTE	non-LTE	LTE		LTE	non-LTE	LTE				
(1)	(J2000)	(mJy)	(AU)	(K)	(K)	(K)	(K)	(km s $^{-1}$)	(km s $^{-1}$)	(km s $^{-1}$)	(km s $^{-1}$)	(M_{\odot})	(14)	(15)
(2)	(2)	(3)	(4)	(5)	(6)	(7)	(8)	(9)	(10)	(11)	(12)	(13)	(14)	(15)
1	17:44:41.38, -29:28:29.90	19.33	4620	125.1 \pm 20.3	140 \pm 7	-	125.1 \pm 20.3	2.34 \pm 0.1	2.18 \pm 0.32	-	2.34 \pm 0.1	4.79	3.43 \pm 0.18	0.54
2	17:44:41.32, -29:28:30.03	0.34	1360	88 \pm 28	101 \pm 63	-	<89.1	1.56 \pm 0.2	1.27 \pm 0.37	-	1.56 \pm 0.2	<0.09	2.61 \pm 0.41	0.26
3	17:44:40.81, -29:28:27.70	0.37	1290	-	-	-	-	-	-	-	-	0.84	-	-
4	17:44:41.21, -29:28:26.84	1.1	2330	113.5 \pm 42.8	125 \pm 16	-	113.5 \pm 42.8	1.56 \pm 0.18	1.43 \pm 0.53	-	1.56 \pm 0.18	0.31	2.30 \pm 0.33	0.13
5	17:44:41.20, -29:28:23.94	0.61	1680	43.8 \pm 7.4	65 \pm 39	-	43.5 \pm 7.3	1.24 \pm 0.14	1.02 \pm 0.28	-	1.24 \pm 0.14	0.50	3.02 \pm 0.41	0.31
6	17:44:40.76, -29:28:19.77	0.36	1370	-	-	-	-	-	-	-	-	0.77	-	-
7	17:44:40.79, -29:28:19.50	1.15	1310	26.8 \pm 7.1	26 \pm 26	-	<89.9	1.36 \pm 0.21	1.35 \pm 0.31	-	1.36 \pm 0.21	<0.32	4.04 \pm 0.78	0.52
8	17:44:40.78, -29:28:19.09	1.14	1310	73.7 \pm 31.2	130 \pm 12	-	<99.5	1.7 \pm 0.33	1.53 \pm 0.63	-	1.7 \pm 0.33	<0.28	3.15 \pm 0.72	0.35
9	17:44:40.68, -29:28:19.20	0.43	1440	-	-	-	-	-	-	-	-	0.90	-	-
10	17:44:40.73, -29:28:19.01	0.25	1150	-	-	-	-	-	-	-	-	0.54	-	-
11	17:44:40.67, -29:28:17.93	3.16	2350	282.5 \pm 156.2	140 \pm 10	-	282.5 \pm 156.2	1.64 \pm 0.11	1.66 \pm 0.28	-	1.64 \pm 0.11	0.37	1.53 \pm 0.17	0.05
12	17:44:40.29, -29:28:17.38	1.66	2840	-	-	-	-	-	-	-	-	3.63	-	-

Table E2 *continued*

Table E2 (*continued*)

Core ID	RA and Dec	Flux	R	$T_{\text{H}_2\text{CO}}$	$T_{\text{H}_2\text{CO}}$	$T_{\text{CH}_3\text{CN}}$	T	$\sigma_{\text{H}_2\text{CO}}$	$\sigma_{\text{H}_2\text{CO}}$	$\sigma_{\text{CH}_3\text{CN}}$	σ	M_{core}	\mathcal{M}	$\alpha_{\text{vir,p}}$							
								density	LTE	non-LTE	LTE	LTE	non-LTE	LTE	(km s $^{-1}$)	(M_{\odot})	(14)	(15)			
								(J2000)	(mJy)	(AU)	(K)	(K)	(K)	(K)	(km s $^{-1}$)	(M_{\odot})					
(1)	(2)	(3)	(4)	(5)	(6)	(7)	(8)	(9)	(10)	(11)	(12)	(13)	(14)	(15)							
13	17:44:42.90, -29:28:17.12	6.67	4830	115.8±12.7	142±24	-	115.8±12.7	1.02±0.04	1.22±0.31	-	1.02±0.04	1.79	1.30±0.08	0.01							
14	17:44:40.46, -29:28:17.17	3.5	2430	56.9±7.3	73±0.42	-	56.9±7.3	1.7±0.12	2.09±0.23	-	1.7±0.12	2.19	3.59±0.30	0.21							
15	17:44:40.57, -29:28:17.24	9.92	1560	188±60.4	142±87	65.0±11.4	65.0±11.4	1.59±0.1	1.5±0.1	2.19±0.22	2.19±0.22	5.30	4.42±0.49	1.65							
16	17:44:40.16, -29:28:17.18	0.55	1460	67.6±11.1	141±49	-	67.6±11.1	1.01±0.09	1.04±0.17	-	1.01±0.09	0.31	1.69±0.23	0.04							
17	17:44:40.39, -29:28:17.12	0.6	1650	35.2±3.2	73±46	-	35.2±3.2	2.28±0.12	2.26±0.28	-	2.28±0.12	0.65	6.31±0.36	0.37							
18	17:44:40.12, -29:28:17.23	0.49	1410	-	-	-	-	-	-	-	-	1.14	-	-							
19	17:44:40.54, -29:28:17.23	5.39	1090	121.3±70.3	136.3±6.8	-	121.3±70.3	2.41±0.38	2.26±0.49	-	2.41±0.38	1.49	3.60±0.68	2.62							
20	17:44:40.75, -29:28:16.71	4.79	2280	-	-	-	-	-	-	-	-	9.86	-	-							
21	17:44:40.20, -29:28:16.69	0.47	1410	41.9±4	48±18	-	41.9±4	1.14±0.07	0.626±0.053	-	1.14±0.07	0.44	2.57±0.22	0.09							
22	17:44:40.58, -29:28:15.95	148.87	4850	-	-	729.8±152.0	729.8±152.0	-	-	4.42±0.17	4.42±0.17	9.07	3.37±0.15	0.85							
23	17:44:40.39, -29:28:16.53	0.86	1490	39.4±3.5	69±19	-	39.5±3.5	1.21±0.07	1.28±0.095	-	1.21±0.07	0.81	2.87±0.22	0.16							
24	17:44:40.34, -29:28:16.40	1.32	1840	42.2±5.6	48±17	-	42.2±5.6	1.67±0.14	1.68±0.25	-	1.67±0.14	1.18	4.09±0.40	0.24							
25	17:44:41.12, -29:28:16.38	1.64	2490	-	-	-	-	-	-	-	-	3.54	-	-							
26	17:44:40.48, -29:28:16.36	20.86	2740	-	-	77.4±7.8	77.4±7.8	-	-	3.6±0.24	3.6±0.24	9.22	6.85±0.50	2.27							
27	17:44:40.75, -29:28:16.23	0.22	1060	-	-	-	-	-	-	-	-	0.45	-	-							
28	17:44:40.30, -29:28:15.87	2.29	2340	100±27.4	127±82	-	100±27.4	1.94±0.18	3.44±0.64	-	1.94±0.18	0.80	3.13±0.34	0.12							
29	17:44:42.98, -29:28:15.91	3.08	2000	151.9±46.3	120.0±120.0	-	151.9±46.3	1.8±0.13	2.25±0.46	-	1.8±0.13	0.63	2.33±0.22	0.15							
30	17:44:40.43, -29:28:15.81	1.7	1920	125±40.7	136.8±2.4	-	125±40.7	1.61±0.15	2.01±0.32	-	1.61±0.15	0.45	2.27±0.27	0.09							
31	17:44:40.16, -29:28:15.64	2.2	2370	119.3±47.3	118.0±20.0	-	119.3±47.3	1.04±0.12	1.06±0.27	-	1.04±0.12	0.66	1.32±0.24	0.03							
32	17:44:42.78, -29:28:15.54	1.19	2270	38.1±3.5	121±58	-	38.1±3.5	0.72±0.04	0.7±0.13	-	0.72±0.04	1.08	1.16±0.19	0.02							
33	17:44:40.24, -29:28:15.51	1.16	1630	-	-	-	-	-	-	-	-	-	-	-							
34	17:44:42.94, -29:28:15.43	4.39	2160	166.8±53.2	139±16	-	166.8±53.2	2.51±0.17	2.69±0.53	-	2.51±0.17	0.82	3.20±0.27	0.29							
35	17:44:40.50, -29:28:15.31	0.65	1200	-	-	68.2±11.2	68.2±11.2	-	-	3.29±0.38	3.29±0.38	0.33	6.68±0.69	1.07							
36	17:44:40.35, -29:28:15.10	2.52	2910	137.6±57.3	130.7±8.2	-	137.6±57.3	3.07±0.3	3.69±0.65	-	3.07±0.3	0.62	4.36±0.51	0.12							
37	17:44:40.20, -29:28:15.26	0.89	1450	38.9±8.9	46±39	-	38.9±8.9	1.19±0.18	1.08±0.28	-	1.19±0.18	0.89	2.83±0.57	0.17							
38	17:44:40.72, -29:28:15.26	0.2	1040	-	-	-	-	-	-	-	-	0.41	-	-							
39	17:44:40.29, -29:28:15.05	0.41	1170	91.8±40.5	136±82	-	91.8±40.5	1.37±0.24	3.21±0.57	-	1.37±0.24	0.16	2.19±0.49	0.09							
40	17:44:42.81, -29:28:15.04	0.53	1590	-	-	-	-	-	-	-	-	1.04	-	-							
41	17:44:40.13, -29:28:15.01	0.96	1340	-	-	-	-	-	-	-	-	2.15	-	-							
42	17:44:40.76, -29:28:14.89	0.58	1640	-	-	-	-	-	-	-	-	1.18	-	-							
43	17:44:40.61, -29:28:14.96	3.1	1140	87.4±15.6	73.0±0.6	-	87.4±15.6	0.79±0.06	0.72±0.07	-	0.79±0.06	1.12	2.19±0.49	0.64							
44	17:44:40.90, -29:28:14.93	0.79	1830	-	-	-	-	-	-	-	-	1.62	-	-							
45	17:44:40.86, -29:28:14.82	0.35	1360	-	-	-	-	-	-	-	-	0.71	-	-							
46	17:44:40.11, -29:28:14.58	1.69	1730	155.1±66.1	136.9±3.8	-	155.1±66.1	1.89±0.18	2.32±0.46	-	1.89±0.18	0.39	2.44±0.30	0.14							
47	17:44:40.96, -29:28:14.54	1.1	1900	36.6±8.1	62±41	-	36.6±8.1	2.02±0.27	1.79±0.59	-	2.02±0.27	1.11	5.43±0.81	0.32							
48	17:44:40.53, -29:28:14.67	0.54	1280	129.6±36.5	142.5±4.8	-	129.6±36.5	4.74±0.32	4.32±0.32	-	4.74±0.32	0.13	7.01±0.56	0.78							
49	17:44:40.04, -29:28:14.49	0.5	1490	110.4±26.7	173±90	-	110.4±26.7	1.3±0.11	1.05±0.14	-	1.3±0.11	0.17	1.86±0.21	0.04							
50	17:44:40.26, -29:28:14.40	0.72	1040	-	-	-	-	-	-	-	-	1.54	-	-							
51	17:44:41.03, -29:28:14.18	3.07	2790	98.6±27.8	121±83	-	98.6±27.8	1.48±0.25	1.12±0.35	-	1.48±0.25	1.04	2.32±0.48	0.06							
52	17:44:40.50, -29:28:13.99	35.75	3700	114.8±26.2	133±5.3	82.1±8.9	82.1±8.9	2.29±0.15	1.7±0.16	1.96±0.11	1.96±0.11	10.56	3.56±0.22	0.52							
53	17:44:40.35, -29:28:14.18	3.26	2140	109.7±46.3	140±110	-	109.7±46.3	2.27±0.29	3.1±0.5	-	2.27±0.29	1.00	3.55±0.53	0.28							
54	17:44:40.17, -29:28:14.13	2.29	1490	130.1±34.3	129.6±6.7	-	130.1±34.3	1.6±0.12	1.65±0.43	-	1.6±0.12	0.62	2.21±0.21	0.25							
55	17:44:39.88, -29:28:13.99	1.9	2760	-	-	-	-	-	-	-	-	4.89	-	-							
56	17:44:40.24, -29:28:13.94	1.7	1460	118.9±24.2	125±76	-	118.9±24.2	1.36±0.09	1.37±0.23	-	1.36±0.09	0.50	1.90±0.17	0.15							
57	17:44:40.68, -29:28:13.92	0.3	1180	-	-	-	-	-	-	-	-	0.60	-	-							
58	17:44:41.10, -29:28:13.83	0.23	1150	166±118.7	112±11	-	166±118.7	1.51±0.23	1.41±0.33	-	1.51±0.23	0.04	1.82±0.38	0.04							
59	17:44:40.62, -29:28:13.68	1.88	2290	-	-	-	-	-	-	-	-	3.75	-	-							
60	17:44:40.39, -29:28:13.80	0.73	1140	-	-	-	-	-	-	-	-	1.50	-	-							
61	17:44:39.83, -29:28:13.54	0.52	1630	-	-	-	-	-	-	-	-	1.39	-	-							
62	17:44:40.13, -29:28:13.53	8.44	1410	-	-	-	-	-	-	-	-	18.94	-	-							
63	17:44:40.08, -29:28:13.33	24.63	2280	117.4±43.7	105±15	143.3±15.0	143.3±15.0	1.28±0.15	1.32±0.16	2.11±0.10	2.11±0.10	4.44	2.68±0.14	1.49							
64	17:44:40.54, -29:28:13.27	5.66	2040	-	-	-	-	-	-	-	-	11.36	-	-							
65	17:44:40.16, -29:28:12.95	69.56	2560	-	-	1241.4±449															

Table E2 (continued)

Core ID	RA and Dec	Flux	R	$T_{\text{H}_2\text{CO}}$	$T_{\text{H}_2\text{CO}}$	$T_{\text{CH}_3\text{CN}}$	T	$\sigma_{\text{H}_2\text{CO}}$	$\sigma_{\text{H}_2\text{CO}}$	$\sigma_{\text{CH}_3\text{CN}}$	σ	M_{core}	\mathcal{M}	$\alpha_{\text{vir,p}}$
		density	LTE	non-LTE	LTE		LTE	non-LTE	LTE					
(1)	(J2000)	(mJy)	(AU)	(K)	(K)	(K)	(K)	(km s $^{-1}$)	(km s $^{-1}$)	(km s $^{-1}$)	(km s $^{-1}$)	(M_{\odot})	(14)	(15)
(2)	(3)	(4)	(5)	(6)	(7)	(8)	(9)	(10)	(11)	(12)	(13)	(14)	(15)	
75	17:44:39.92, -29:28:11.75	0.5	1430	69.7±14.6	85±30	-	69.7±14.6	2.63±0.24	2.28±0.28	-	2.63±0.24	0.31	5.21±0.53	0.55
76	17:44:40.30, -29:28:11.66	0.35	1280	-	-	-	-	-	-	-	-	0.74	-	-
77	17:44:39.98, -29:28:11.69	0.27	1200	63.1±14.8	52±30	-	63.1±14.8	1.42±0.18	0.93±0.14	-	1.42±0.18	0.18	2.76±0.43	0.16
78	17:44:40.12, -29:28:11.55	0.24	1140	97.3±40.7	157±77	-	97.3±40.7	1.58±0.24	1.53±0.33	-	1.58±0.24	0.09	2.52±0.47	0.13
79	17:44:39.95, -29:28:11.52	0.22	1090	36.4±8.1	40±26	-	<90.4	1.57±0.23	1.1±0.2	-	1.57±0.23	<0.06	4.10±0.71	0.36
80	17:44:39.70, -29:28:11.32	1.22	2100	-	-	-	-	-	-	-	-	3.79	-	-
81	17:44:40.31, -29:28:11.34	0.32	1250	-	-	-	-	-	-	-	-	0.69	-	-
82	17:44:41.51, -29:28:10.77	0.19	1030	-	-	-	-	-	-	-	-	0.39	-	-
83	17:44:41.48, -29:28:10.16	0.3	1320	-	-	-	-	-	-	-	-	0.60	-	-
84	17:44:41.45, -29:28:10.37	0.21	1080	-	-	-	-	-	-	-	-	0.42	-	-
85	17:44:40.38, -29:28:10.02	0.34	1290	111.2±42	113±12	-	111.2±42	1.74±0.2	1.84±0.35	-	1.74±0.2	0.10	2.63±0.37	0.13
86	17:44:41.56, -29:28:09.68	0.24	1170	-	-	-	-	-	-	-	-	0.49	-	-
87	17:44:40.39, -29:28:09.64	0.23	1120	-	-	-	-	-	-	-	-	0.49	-	-
88	17:44:41.49, -29:28:09.46	0.29	1240	-	-	-	-	-	-	-	-	0.57	-	-
89	17:44:41.35, -29:28:08.63	1.15	2300	-	-	-	-	-	-	-	-	2.17	-	-
90	17:44:41.55, -29:28:07.45	2.35	3020	142.7±50.2	122±70	-	142.7±50.2	4.16±0.32	4.07±0.61	-	4.16±0.32	0.50	5.85±0.55	0.33
91	17:44:40.70, -29:28:07.03	0.21	1090	-	-	-	-	-	-	-	-	0.42	-	-
92	17:44:40.33, -29:28:07.06	0.29	1270	102.7±29.3	69.7±1.4	-	102.7±29.3	3.58±0.31	3.5±0.45	-	3.58±0.31	0.11	5.91±0.58	1.56
93	17:44:40.28, -29:28:06.94	0.45	1540	106.5±33.8	72±11	-	106.5±33.8	2.07±0.21	1.94±0.29	-	2.07±0.21	0.16	3.26±0.39	0.42
94	17:44:43.35, -29:28:06.66	0.56	1510	-	-	-	-	-	-	-	-	1.83	-	-
95	17:44:41.36, -29:28:06.64	4.95	2310	-	-	-	-	-	-	-	-	8.91	-	-
96	17:44:41.27, -29:28:06.69	0.74	1870	-	-	-	-	-	-	-	-	1.34	-	-
97	17:44:41.52, -29:28:06.34	18.37	3560	-	-	106.2±11.9	106.2±11.9	-	-	4.06±0.24	4.06±0.24	3.75	6.45±0.34	4.60
98	17:44:41.44, -29:28:06.18	17.56	3250	-	-	-	-	-	-	-	-	31.37	-	-
99	17:44:43.48, -29:28:05.98	1.29	2150	-	-	-	-	-	-	-	-	4.99	-	-
100	17:44:40.52, -29:28:05.85	0.36	1320	-	-	-	-	-	-	-	-	0.79	-	-
101	17:44:40.01, -29:28:05.62	0.2	1060	113.6±55.5	136.3±6.4	-	113.6±55.5	2.42±0.34	2.23±0.48	-	2.42±0.34	0.09	3.74±0.62	0.71
102	17:44:41.47, -29:28:05.46	4.14	2810	-	-	-	-	-	-	-	-	7.29	-	-
103	17:44:41.53, -29:28:05.04	0.93	1690	-	-	-	-	-	-	-	-	1.62	-	-
104	17:44:40.65, -29:28:05.09	0.75	1850	42.6±12.8	58±35	-	<106.5	1.45±0.28	1.31±0.58	-	1.45±0.28	<0.17	3.45±0.81	0.49
105	17:44:40.74, -29:28:04.83	1.51	2520	42.3±5.8	58±34	-	<79.8	1.58±0.14	1.49±0.38	-	1.58±0.14	<0.47	3.83±0.40	0.47
106	17:44:40.81, -29:28:04.92	0.36	1330	53.3±11	67±48	-	53.3±11	1.87±0.21	1.77±0.45	-	1.87±0.21	0.23	4.13±0.53	0.85
107	17:44:40.87, -29:28:04.81	0.28	1270	-	-	-	-	-	-	-	-	0.54	-	-
108	17:44:40.68, -29:28:04.66	0.67	1790	36.5±7.3	46±41	-	<87.7	1.59±0.2	1.49±0.49	-	1.59±0.2	<0.14	4.16±0.62	0.69
109	17:44:41.65, -29:28:04.69	0.24	1080	-	-	-	-	-	-	-	-	0.42	-	-
110	17:44:41.60, -29:28:04.53	0.41	1490	-	-	-	-	-	-	-	-	0.71	-	-
111	17:44:41.08, -29:28:04.37	2.99	2140	166±75.7	131±17	-	166±75.7	1.97±0.18	1.71±0.51	-	1.97±0.18	0.52	2.47±0.30	0.79
112	17:44:40.18, -29:28:04.53	0.29	1210	-	-	-	-	-	-	-	-	0.82	-	-
113	17:44:41.54, -29:28:04.44	0.48	1410	90.3±37.4	118±86	-	90.3±37.4	1.53±0.25	1.57±0.52	-	1.53±0.25	0.15	2.52±0.51	0.48
114	17:44:40.91, -29:28:04.00	0.79	2050	-	-	-	-	-	-	-	-	1.50	-	-
115	17:44:41.72, -29:28:03.37	33.43	3720	98.4±49.4	125±55	129.0±15.6	129.0±15.6	1.65±0.29	2.34±0.88	5.2±0.29	5.2±0.29	7.17	7.71±0.44	1.01
116	17:44:41.64, -29:28:03.95	1.48	2050	-	-	-	-	-	-	-	-	2.55	-	-
117	17:44:40.81, -29:28:03.92	0.32	1270	-	-	-	-	-	-	-	-	0.62	-	-
118	17:44:40.97, -29:28:03.76	1.06	1910	-	-	-	-	-	-	-	-	1.97	-	-
119	17:44:41.04, -29:28:03.72	1.1	1560	43.4±9.7	69±67	-	43.4±9.7	1.19±0.18	1.1±0.42	-	1.19±0.18	0.80	2.67±0.54	0.81
120	17:44:40.82, -29:28:03.61	0.28	1120	36.5±9.3	60±18	-	36.5±9.3	1.47±0.25	1.36±0.35	-	1.47±0.25	0.27	3.79±0.78	1.22
121	17:44:41.09, -29:28:03.02	33.06	6560	171.9±93.1	139±76	-	171.9±93.1	1.88±0.2	1.9±1.1	-	1.88±0.2	5.44	2.30±0.33	0.27
122	17:44:40.79, -29:28:03.46	0.49	1460	-	-	-	-	-	-	-	-	0.98	-	-
123	17:44:40.84, -29:28:03.46	0.32	1180	29.9±6.9	43±37	-	<93.8	1.2±0.18	1.14±0.36	-	1.2±0.18	<0.08	3.26±0.65	0.88
124	17:44:41.63, -29:28:03.10	2.26	2360	-	-	-	-	-	-	-	-	3.82	-	-
125	17:44:40.83, -29:28:03.08	0.37	1200	-	-	-	-	-	-	-	-	0.74	-	-
126	17:44:41.77, -29:28:02.69	4.06	1570	-	-	-	-	-	-	-	-	6.96	-	-
127	17:44:41.68, -29:28:02.49	3.35	1640	82.9±48	57±54	-	82.9±48	3.23±0.67	1.3±0.48	-	3.23±0.67	1.12	5.92±1.36	7.74
128	17:44:40.88, -29:28:02.36	4.35	2640	104.5±26.4	111.5±9.7	-	104.5±26.4	2.9±0.22	3.04±0.41	-	2.9±0.22	1.31	4.71±0.41	1.99
129	17:44:40.93, -29:28:01.99	5.25	2680	110.1±26.7	125±60	-	110.1±26.7	2.12±0.16	2.48±0.58	-	2.12±0.16	1.45	3.29±0.29	1.16
130	17:44:41.15, -29:28:02.17	0.47	1290	126.4±84.7	108±31	-	126.4±84.7	2.27±0.41	1.85±0.71	-	2.27±0.41	0.10	3.31±0.72	0.98
131	17:44:41.06, -29:28:02.19	0.37	1280	84.8±30	77±5.1	-	84.8±30	2.21±0.3	3.5±0.89	-	2.21±0.3	0.13	3.93±0.61	1.13
132	17:44:41.80, -29:28:02.19	0.9	1080	-	-	-	-	-	-	-	-	1.53	-	-
133	17:44:41.64, -29:28:02.16	0.47	1090	-	-	-	-	-	-	-	-	0.78	-	-
134	17:44:41.86, -29:28:01.84	5.26	2330	30.3±8.4	39±38	-	30.3±8.4	3.62±0.5	3.6±1.3	-	3.62±0.5	5.55	7.88±1.61	3.67
135	17:44:41.21, -29:28:01.93	0.4	1340	81.6±20.7	92±37	-	81.6±20.7	2.27±0.23	2.25±0.54	-	2.27±0.23	0.14	4.12±0.47	1.13
136	17:44:41.71, -29:28:01.78	0.48	1620	-	-	-	-	-	-	-	-	0.80	-	-

Table E2 continued

Table E2 (continued)

Core ID	RA and Dec	Flux	R	$T_{\text{H}_2\text{CO}}$	$T_{\text{H}_2\text{CO}}$	$T_{\text{CH}_3\text{CN}}$	T	$\sigma_{\text{H}_2\text{CO}}$	$\sigma_{\text{H}_2\text{CO}}$	$\sigma_{\text{CH}_3\text{CN}}$	σ	M_{core}	\mathcal{M}	$\alpha_{\text{vir,p}}$
				density	LTE	non-LTE		LTE	non-LTE	LTE	LTE	(km s $^{-1}$)	(km s $^{-1}$)	(km s $^{-1}$)
				(J2000)	(mJy)	(AU)	(K)	(K)	(K)	(K)	(km s $^{-1}$)	(km s $^{-1}$)	(km s $^{-1}$)	(M_{\odot})
(1)	(2)	(3)	(4)	(5)	(6)	(7)	(8)	(9)	(10)	(11)	(12)	(13)	(14)	(15)
137	17:44:41.81, -29:28:01.40	3.42	2620	58.6±18.7	76±65	-	58.6±18.7	3.37±0.49	3.5±1.2	-	3.37±0.49	1.67	7.36±1.15	3.72
138	17:44:41.01, -29:28:01.62	0.21	1080	94±25.8	78±29	-	94±25.8	4.45±0.39	3.86±0.81	-	4.45±0.39	0.07	7.72±0.75	4.22
139	17:44:41.18, -29:28:01.48	0.91	1950	81±24.2	111±82	-	81±24.2	2.22±0.26	1.98±0.61	-	2.22±0.26	0.32	4.04±0.54	0.82
140	17:44:41.96, -29:28:01.47	3.05	1280	-	-	-	-	-	-	-	-	5.38	-	-
141	17:44:41.22, -29:28:01.34	0.35	1060	79.4±31.5	189±81	-	79.4±31.5	1.5±0.26	2.06±0.54	-	1.5±0.26	0.12	2.63±0.56	0.88
142	17:44:42.00, -29:28:00.97	16.51	2370	-	-	-	-	-	-	-	-	29.24	-	-
143	17:44:40.87, -29:28:01.24	1.48	1210	65.1±15.4	90±15	-	65.1±15.4	3.11±0.32	3.18±0.52	-	3.11±0.32	0.75	6.43±0.72	9.94
144	17:44:40.96, -29:28:00.85	3.2	2170	110.7±19.9	149±22	-	110.7±19.9	1.99±0.11	1.76±0.33	-	1.99±0.11	0.87	3.06±0.20	1.18
145	17:44:41.12, -29:28:00.89	0.44	1220	15.1±13	45±45	-	<84.4	1.15±0.14	0.95±0.25	-	1.15±0.14	<0.13	4.35±0.89	1.18
146	17:44:40.86, -29:28:00.90	2.03	1420	107±38.4	157±77	-	107±38.4	2.06±0.23	2.02±0.34	-	2.06±0.23	0.61	3.24±0.43	2.71
147	17:44:41.04, -29:28:00.83	0.66	1340	79±17.6	126±19	-	79±17.6	1.32±0.14	1.18±0.25	-	1.32±0.14	0.25	2.25±0.31	0.63
148	17:44:41.16, -29:28:00.54	1.86	2000	50.2±6.7	99±67	-	50.2±6.7	1.19±0.1	1.24±0.31	-	1.19±0.1	1.09	2.48±0.28	0.59
149	17:44:40.91, -29:28:00.71	0.65	1060	148.7±40.6	144.4±5.3	-	148.7±40.6	1.97±0.13	2.31±0.28	-	1.97±0.13	0.13	2.61±0.22	1.64
150	17:44:41.26, -29:28:00.40	6.78	2190	120.6±30.3	125±66	-	120.6±30.3	2.71±0.18	3.04±0.62	-	2.71±0.18	1.51	4.09±0.32	3.58
151	17:44:41.08, -29:28:00.37	1.34	1940	-	-	-	-	-	-	-	-	2.37	-	-
152	17:44:41.00, -29:28:00.49	0.88	1440	77.1±10.9	125±39	-	77.1±10.9	2.3±0.14	1.92±0.16	-	2.3±0.14	0.35	4.30±0.29	2.17
153	17:44:41.27, -29:27:59.75	15.63	2870	111.8±23	129.6±4.9	-	111.8±23	2.01±0.13	2.13±0.35	-	2.01±0.13	3.73	3.08±0.24	1.82
154	17:44:42.13, -29:27:59.79	0.99	1620	-	-	-	-	-	-	-	-	1.82	-	-
155	17:44:41.47, -29:27:59.87	0.39	1340	71.6±25.8	89±44	-	71.6±25.8	1.52±0.26	1.39±0.51	-	1.52±0.26	0.14	2.81±0.58	0.57
156	17:44:41.12, -29:27:59.73	2.84	2430	72.8±17.6	140±130	-	72.8±17.6	2.49±0.25	3.77±0.81	-	2.49±0.25	1.12	4.81±0.54	1.75
157	17:44:42.03, -29:27:59.33	3.64	2850	-	-	-	-	-	-	-	-	6.32	-	-
158	17:44:41.20, -29:27:59.63	1.95	1360	80±31.4	135±37	-	80±31.4	3.09±0.46	2.12±0.42	-	3.09±0.46	0.68	5.76±0.95	8.03
159	17:44:41.89, -29:27:59.42	1.58	2180	-	-	-	-	-	-	-	-	2.61	-	-
160	17:44:41.46, -29:27:59.37	0.36	1270	177.4±83.1	53±2.1	-	177.4±83.1	1.02±0.09	1.27±0.37	-	1.02±0.09	0.05	1.04±0.16	0.14
161	17:44:41.33, -29:27:59.30	2.04	1110	108.3±29.2	119±68	-	108.3±29.2	5.1±0.38	4.73±0.31	-	5.1±0.38	0.49	4.86±0.70	29.57
162	17:44:41.29, -29:27:58.85	19.25	2520	-	-	343.4±30.5	343.4±30.5	-	-	4.21±0.12	4.21±0.12	1.39	3.92±0.13	6.57
163	17:44:42.09, -29:27:58.76	0.25	1180	-	-	-	-	-	-	-	-	0.44	-	-
164	17:44:42.12, -29:27:58.54	0.24	1170	-	-	-	-	-	-	-	-	0.43	-	-
165	17:44:41.23, -29:27:58.52	10.45	1980	-	-	182.6±17.9	182.6±17.9	-	-	4.23±0.23	4.23±0.23	1.79	5.45±0.59	10.97
166	17:44:41.19, -29:27:57.67	9.29	2040	-	-	-	-	-	-	-	-	15.52	-	-
167	17:44:42.12, -29:27:57.66	1.07	2160	-	-	-	-	-	-	-	-	1.88	-	-
168	17:44:41.26, -29:27:57.82	0.23	1030	95.3±23.7	101±37	-	95.3±23.7	5.83±0.44	5±0.43	-	5.83±0.44	0.06	10.09±0.85	7.37
169	17:44:41.71, -29:27:57.21	0.49	1530	212.9±128.7	138±31	-	212.9±128.7	1.67±0.16	2.07±0.64	-	1.67±0.16	0.06	1.80±0.25	0.17
170	17:44:41.57, -29:27:56.58	2.44	3270	-	-	-	-	-	-	-	-	3.76	-	-
171	17:44:42.03, -29:27:56.95	1.16	1530	-	-	-	-	-	-	-	-	1.95	-	-
172	17:44:41.90, -29:27:56.88	1.06	1280	-	-	-	-	-	-	-	-	1.71	-	-
173	17:44:41.73, -29:27:56.80	3.76	1580	144.3±79.1	125±52	-	144.3±79.1	1.21±0.17	1.42±0.41	-	1.21±0.17	0.65	1.48±0.30	0.89
174	17:44:41.25, -29:27:56.77	0.42	1220	37.5±6.5	49±36	-	<89.4	4.5±0.42	3.08±0.62	-	4.5±0.42	<0.12	12.83±1.27	12.98
175	17:44:41.35, -29:27:56.68	0.8	1440	94.6±32.7	140±130	-	94.6±32.7	2.82±0.31	2.86±0.61	-	2.82±0.31	0.22	4.81±0.60	2.17
176	17:44:41.87, -29:27:56.60	1.66	1520	-	-	-	-	-	-	-	-	2.64	-	-
177	17:44:42.08, -29:27:56.43	7.99	2330	121.5±69.6	171±74	-	121.5±69.6	0.94±0.16	0.87±0.19	-	0.94±0.16	1.81	1.11±0.33	0.40
178	17:44:41.75, -29:27:56.38	1.97	1480	31.5±9.1	42±40	-	<86.8	1.02±0.18	0.97±0.35	-	1.02±0.18	<0.56	2.54±0.67	0.70
179	17:44:41.28, -29:27:56.03	2.34	2350	39.1±4.3	46±25	-	39.1±4.3	4.98±0.27	4.48±0.95	-	4.98±0.27	1.72	13.43±0.77	10.08
180	17:44:41.66, -29:27:56.25	0.21	1030	-	-	-	-	-	-	-	-	0.32	-	-
181	17:44:42.18, -29:27:56.12	0.28	1200	-	-	-	-	-	-	-	-	0.51	-	-
182	17:44:42.10, -29:27:55.83	9.23	1980	-	-	107.6±15.8	107.6±15.8	-	-	3.79±0.31	3.79±0.31	2.13	6.04±0.47	9.70
183	17:44:42.04, -29:27:55.82	1.99	1570	-	-	477.7±164.8	477.7±164.8	-	-	3.09±0.78	3.09±0.78	0.60	3.73±0.36	2.34
184	17:44:41.85, -29:27:55.62	1.38	2000	36.2±7.9	48±45	-	36.2±7.9	1.97±0.26	1.76±0.69	-	1.97±0.26	1.08	5.31±0.79	1.63
185	17:44:41.65, -29:27:55.60	1.14	1940	58.7±9.4	84±70	-	58.7±9.4	1.69±0.15	1.46±0.38	-	1.69±0.15	0.50	3.51±0.36	0.71
186	17:44:41.89, -29:27:55.70	0.39	1030	-	-	-	-	-	-	-	-	0.61	-	-
187	17:44:42.13, -29:27:55.42	16.14	2000	-	-	-	-	-	-	-	-	27.90	-	-
188	17:44:41.26, -29:27:55.31	3.15	2320	90.1±19.1	190±190	-	90.1±19.1	5.53±0.37	4.63±0.82	-	5.53±0.37	0.92	9.84±0.73	7.90
189	17:44:42.19, -29:27:55.32	0.31	1250	-	-	-	-	-	-	-	-	0.54	-	-
190	17:44:41.68, -29:27:55.09	2.15	2300	-	-	-	-	-	-	-	-	3.28	-	-
191	17:44:41.91, -29:27:55.16	0.57	1060	-	-	-	-	-	-	-	-	0.90	-	-
192	17:44:41.88, -29:27:55.19	0.78	1110	-	-	-	-	-	-	-	-	1.23	-	-
193	17:44:42.00, -29:27:55.11	0.21	1060	-	-	-	-	-	-	-	-	0.34	-	-
194	17:44:41.31, -29:27:54.92	5.53	2280	66.5±12.6	150±120	-	<81.5	10.98±0.77	7±1	-	10.98±0.77	<1.69	25.24±1.99	76.14
195	17:44:41.80, -29:27:54.90	5.09	2090	106.1±35.1	120±110	-	106.1±35.1	1.43±0.16	1.07±0.28	-	1.43±0.16	1.21	2.14±0.31	7.34
196	17:44:42.16, -29:27:54.76	12.94	2480	-	-	237.9±52.5	237.9±52.5	-	-	4.86±0.48	4.86±0.48	1.50	5.31±0.56	1.72
197	17:44:41.06, -29:27:54.61	3.52	2710	-	-	-	-	-	-	-	-	6.16	-	-
198	17:44:41.61, -29:27:54.71	2.27	2210	-	-	-	-	-	-	-	-	3.46	-	-

Table E2 continued

Table E2 (*continued*)

Core ID	RA and Dec (J2000)	Flux (mJy)	R (AU)	$T_{\text{H}_2\text{CO}}$ (K)	$T_{\text{H}_2\text{CO}}$ (K)	$T_{\text{CH}_3\text{CN}}$ (K)	T (K)	$\sigma_{\text{H}_2\text{CO}}$ (km s $^{-1}$)	$\sigma_{\text{H}_2\text{CO}}$ (km s $^{-1}$)	$\sigma_{\text{CH}_3\text{CN}}$ (km s $^{-1}$)	σ	M_{core} (M_{\odot})	\mathcal{M}	$\alpha_{\text{vir},p}$	
(1)	(2)	(3)	(4)	(5)	(6)	(7)	(8)	(9)	(10)	(11)	(12)	(13)	(14)	(15)	
199	17:44:40.52, -29:27:54.80	0.42	1430	-	-	-	-	-	-	-	-	-	1.13	-	-
200	17:44:41.27, -29:27:54.59	1.44	1390	-	-	-	-	-	-	-	-	-	2.31	-	-
201	17:44:42.09, -29:27:54.50	0.24	1150	-	-	-	-	-	-	-	-	-	0.41	-	-
202	17:44:41.81, -29:27:54.47	1.34	1420	43.3±9.8	60±56	-	<81.7	1.02±0.15	0.86±0.35	-	1.02±0.15	<0.41	2.16±0.48	0.70	
203	17:44:41.93, -29:27:54.44	0.54	1520	-	-	-	-	-	-	-	-	-	0.86	-	-
204	17:44:41.34, -29:27:54.42	0.63	1200	48.7±14.2	81±39	-	48.7±14.2	3.75±0.53	3.4±1.1	-	3.75±0.53	0.35	9.01±1.36	9.61	
205	17:44:42.19, -29:27:54.19	6.74	2000	-	-	-	-	-	-	-	-	-	11.91	-	-
206	17:44:41.00, -29:27:54.25	0.27	1220	42.8±3.4	60±17	-	42.8±3.4	1.39±0.07	1.63±0.48	-	1.39±0.07	0.20	3.27±0.20	0.63	
207	17:44:41.88, -29:27:54.22	0.23	1150	-	-	-	-	-	-	-	-	-	0.35	-	-
208	17:44:41.53, -29:27:54.06	0.32	1370	-	-	-	-	-	-	-	-	-	0.49	-	-
209	17:44:41.30, -29:27:54.15	0.46	1180	-	-	-	-	-	-	-	-	-	0.73	-	-
210	17:44:42.25, -29:27:53.87	9.53	3980	-	-	-	-	-	-	-	-	-	17.46	-	-
211	17:44:41.37, -29:27:54.14	0.27	1080	136.6±55	138±19	-	136.6±55	5.22±0.47	4.74±0.93	-	5.22±0.47	0.05	7.53±0.81	4.30	
212	17:44:41.42, -29:27:54.02	0.58	1460	44.3±7.9	47±26	-	44.3±7.9	5.62±0.47	4.86±0.9	-	5.62±0.47	0.35	14.26±1.26	12.88	
213	17:44:41.78, -29:27:53.87	2.07	1840	-	-	-	-	-	-	-	-	-	3.19	-	-
214	17:44:41.61, -29:27:53.91	0.31	1320	-	-	-	-	-	-	-	-	-	0.48	-	-
215	17:44:41.36, -29:27:53.39	8.03	4090	-	-	-	-	-	-	-	-	-	12.53	-	-
216	17:44:41.12, -29:27:53.56	4.63	2570	43.9±2.9	50±16	-	43.9±2.9	1.57±0.06	1.5±0.2	-	1.57±0.06	3.12	3.74±0.17	1.05	
217	17:44:42.32, -29:27:53.19	0.51	1080	-	-	-	-	-	-	-	-	-	0.98	-	-
218	17:44:42.28, -29:27:53.09	5.14	2070	-	-	-	-	-	-	-	-	-	9.61	-	-
219	17:44:41.18, -29:27:53.00	2.55	2020	38.6±3.3	51±29	-	38.6±3.3	1.31±0.08	1.29±0.37	-	1.31±0.08	1.94	3.21±0.25	0.90	
220	17:44:41.45, -29:27:52.56	7.92	3490	118.3±28.4	130.8±1.2	62.3±9.4	62.3±9.4	2.66±0.18	2.56±0.33	1.67±0.13	1.67±0.13	1.08	4.47±0.40	1.26	
221	17:44:41.38, -29:27:52.65	0.81	1530	109.1±27.3	110±17	-	109.1±27.3	2.67±0.2	2.39±0.34	-	2.67±0.2	0.19	4.23±0.37	1.60	
222	17:44:41.70, -29:27:52.41	3.88	2250	-	-	-	-	-	-	-	-	-	5.93	-	-
223	17:44:41.21, -29:27:52.35	0.42	1110	30.8±5.9	39±28	-	30.8±5.9	1.9±0.21	1.45±0.34	-	1.9±0.21	0.42	5.54±0.69	3.38	
224	17:44:41.48, -29:27:52.08	1.27	1420	66±11.8	141±19	-	66±11.8	0.97±0.09	1.23±0.43	-	0.97±0.09	0.49	1.61±0.24	0.55	
225	17:44:41.11, -29:27:51.83	0.71	1840	100.3±17.9	146±38	-	100.3±17.9	1.29±0.09	1.31±0.36	-	1.29±0.09	0.20	1.94±0.18	0.20	
226	17:44:41.22, -29:27:51.80	0.66	1590	-	-	-	-	-	-	-	-	-	1.07	-	-
227	17:44:41.53, -29:27:51.91	0.47	1320	27.1±4.5	39±23	-	<83.5	1.11±0.11	1.02±0.22	-	1.11±0.11	<0.14	3.09±0.43	0.80	
228	17:44:41.54, -29:27:51.22	0.22	1120	62.6±12.9	64±36	-	62.6±12.9	1.43±0.16	1.39±0.41	-	1.43±0.16	0.09	2.80±0.39	0.55	
229	17:44:41.68, -29:27:51.04	0.48	1310	-	-	-	-	-	-	-	-	-	0.74	-	-
230	17:44:42.46, -29:27:51.02	0.21	1030	-	-	-	-	-	-	-	-	-	0.45	-	-
231	17:44:41.57, -29:27:50.87	2.57	2180	47.2±11.3	51±45	-	47.2±11.3	1.69±0.24	1.49±0.65	-	1.69±0.24	1.45	3.92±0.65	1.34	
232	17:44:41.52, -29:27:50.74	1.69	1790	193±107	199±79	-	193±107	1.71±0.17	1.64±0.45	-	1.71±0.17	0.21	1.95±0.27	0.53	
233	17:44:42.47, -29:27:50.71	0.26	1180	-	-	-	-	-	-	-	-	-	0.57	-	-
234	17:44:42.49, -29:27:50.27	0.47	1500	-	-	-	-	-	-	-	-	-	1.05	-	-
235	17:44:41.58, -29:27:49.85	6.92	2860	84.7±12	200±140	-	84.7±12	1.55±0.09	1.42±0.25	-	1.55±0.09	2.08	2.64±0.19	0.79	
236	17:44:41.53, -29:27:49.78	0.87	1630	32.1±4.4	41±17	-	32.1±4.4	1.30±0.12	1.14±0.26	-	1.30±0.12	0.77	3.52±0.47	0.98	
237	17:44:41.59, -29:27:48.69	6.99	4000	107.9±23.1	137.2±5.2	90.1±17.7	90.1±17.7	3.08±0.19	3.19±0.39	2.15±0.22	2.15±0.22	0.97	5.09±0.42	1.13	
238	17:44:42.54, -29:27:49.06	0.38	1320	-	-	-	-	-	-	-	-	-	0.90	-	-
239	17:44:41.68, -29:27:48.35	1.48	1590	65.4±14.5	84±45	-	65.4±14.5	0.87±0.1	0.83±0.23	-	0.87±0.1	0.60	1.35±0.29	0.37	
240	17:44:41.65, -29:27:47.83	4.37	2780	112.9±22.4	143.3±6.1	-	112.9±22.4	2.41±0.14	2.29±0.36	-	2.41±0.14	1.00	3.73±0.25	1.17	
241	17:44:41.74, -29:27:47.07	1.98	2580	131±54.4	185±88	-	131±54.4	3.11±0.31	2.77±0.88	-	3.11±0.31	0.40	4.53±0.54	1.02	
242	17:44:41.83, -29:27:46.97	2.24	2240	-	-	-	-	-	-	-	-	-	3.78	-	-
243	17:44:41.87, -29:27:46.83	0.48	1290	-	-	-	-	-	-	-	-	-	0.82	-	-
244	17:44:41.10, -29:27:44.48	3.03	2730	-	-	-	-	-	-	-	-	-	5.30	-	-
245	17:44:40.86, -29:27:44.35	1.3	1790	-	-	-	-	-	-	-	-	-	2.47	-	-
246	17:44:42.13, -29:27:40.63	0.34	1250	-	-	-	-	-	-	-	-	-	0.90	-	-
247	17:44:46.14, -29:27:39.94	11.37	3340	-	-	-	-	-	-	-	-	-	17.66	-	-
248	17:44:42.10, -29:27:39.98	4.15	2410	-	-	-	-	-	-	-	-	-	11.04	-	-
249	17:44:46.29, -29:27:39.83	0.25	1170	-	-	-	-	-	-	-	-	-	0.37	-	-
250	17:44:46.33, -29:27:39.67	0.91	1040	83.6±15.3	80.9±0.28	-	83.6±15.3	1.36±0.11	1.46±0.35	-	1.36±0.11	0.27	2.27±0.23	0.68	
251	17:44:46.35, -29:27:39.46	1.33	1240	103±27.2	81±28	-	103±27.2	1.41±0.13	1.4±0.34	-	1.41±0.13	0.32	2.14±0.25	0.54	
252	17:44:42.10, -29:27:39.45	0.82	1500	-	-	-	-	-	-	-	-	-	2.28	-	-
253	17:44:42.86, -29:27:39.01	1.45	1940	-	-	-	-	-	-	-	-	-	4.22	-	-
254	17:44:46.34, -29:27:38.81	0.22	1040	-	-	-	-	-	-	-	-	-	0.33	-	-
255	17:44:42.10, -29:27:38.83	0.19	1030	-	-	-	-	-	-	-	-	-	0.54	-	-
256	17:44:42.74, -29:27:38.57	1.1	2270	-	-	-	-	-	-	-	-	-	3.38	-	-
257	17:44:46.31, -29:27:38.27	0.54	1390	-	-	-	-	-	-	-	-	-	0.83	-	-
258	17:44:46.27, -29:27:38.23	0.3	1040	-	-	-	-	-	-	-	-	-	0.46	-	-
259	17:44:41.94, -29:27:37.91	0.38	1390	-	-	-	-	-	-	-	-	-	1.06	-	-
260	17:44:43.03, -29:27:37.11	0.62	1720	-	-	-	-	-	-	-	-	-	1.54	-	-

Table E2 *continued*

Table E2 (*continued*)

Core ID	RA and Dec	Flux	R	$T_{\text{H}_2\text{CO}}$	$T_{\text{H}_2\text{CO}}$	$T_{\text{CH}_3\text{CN}}$	T	$\sigma_{\text{H}_2\text{CO}}$	$\sigma_{\text{H}_2\text{CO}}$	$\sigma_{\text{CH}_3\text{CN}}$	σ	M_{core}	\mathcal{M}	$\alpha_{\text{vir,p}}$
		density	LTE	non-LTE	LTE		LTE	non-LTE	LTE					
(1)	(J2000)	(mJy)	(AU)	(K)	(K)	(K)	(K)	(km s $^{-1}$)	(km s $^{-1}$)	(km s $^{-1}$)	(km s $^{-1}$)	(M_{\odot})	(14)	(15)
(2)	(3)	(4)	(5)	(6)	(7)	(8)	(9)	(10)	(11)	(12)	(13)	(14)	(15)	
261	17:44:42.68, -29:27:36.82	2.39	2190	-	-	-	-	-	-	-	-	7.57	-	-
262	17:44:42.73, -29:27:36.73	0.25	1120	-	-	-	-	-	-	-	-	0.77	-	-
263	17:44:42.69, -29:27:35.23	1.1	1760	-	-	-	-	-	-	-	-	3.44	-	-
264	17:44:43.50, -29:27:33.12	2.67	1720	320.8 \pm 245.1	129 \pm 22	210 \pm 30.3	210 \pm 30.3	2.98 \pm 0.23	2.45 \pm 0.16	4.83 \pm 0.33	4.83 \pm 0.33	0.34	5.03 \pm 0.40	0.81
265	17:44:43.53, -29:27:32.60	4.79	2030	-	-	-	-	-	-	-	-	9.38	-	-
266	17:44:43.54, -29:27:31.85	13.65	2580	130.7 \pm 42.1	129.7 \pm 2.7	-	130.7 \pm 42.1	1.87 \pm 0.16	1.71 \pm 0.14	-	1.87 \pm 0.16	3.29	2.63 \pm 0.28	0.93
267	17:44:42.74, -29:27:31.71	0.38	1360	-	-	-	-	-	-	-	-	1.12	-	-
268	17:44:43.60, -29:27:30.86	5.5	2760	96.5 \pm 16.3	80.97 \pm 0.17	-	96.5 \pm 16.3	1.59 \pm 0.1	2.15 \pm 0.88	-	1.59 \pm 0.1	1.84	2.55 \pm 0.20	0.35
269	17:44:43.12, -29:27:26.74	0.67	1590	-	-	-	-	-	-	-	-	1.67	-	-
270	17:44:43.63, -29:27:26.62	0.71	1790	-	-	-	-	-	-	-	-	1.58	-	-
271	17:44:43.66, -29:27:25.86	1.41	2270	96.7 \pm 22.4	125 \pm 62	-	96.7 \pm 22.4	2.15 \pm 0.17	2.37 \pm 0.49	-	2.15 \pm 0.17	0.55	3.57 \pm 0.33	0.36
272	17:44:43.85, -29:27:22.37	0.26	1150	-	-	-	-	-	-	-	-	0.80	-	-
273	17:44:43.90, -29:27:21.62	1.68	2250	-	-	-	-	-	-	-	-	5.61	-	-
274	17:44:39.55, -29:27:19.83	0.4	1320	88.8 \pm 34.3	126 \pm 13	-	88.8 \pm 34.3	2.01 \pm 0.29	2 \pm 0.32	-	2.01 \pm 0.29	0.25	3.46 \pm 0.58	0.71

Table E3. Properties of the cores in the 20 km s $^{-1}$ cloud.

Core ID	RA and Dec	Flux	R	$T_{\text{H}_2\text{CO}}$	$T_{\text{H}_2\text{CO}}$	$T_{\text{CH}_3\text{CN}}$	T	$\sigma_{\text{H}_2\text{CO}}$	$\sigma_{\text{H}_2\text{CO}}$	$\sigma_{\text{CH}_3\text{CN}}$	σ	M_{core}	\mathcal{M}	$\alpha_{\text{vir,p}}$
		density	LTE	non-LTE	LTE		LTE	non-LTE	LTE					
(1)	(J2000)	(mJy)	(AU)	(K)	(K)	(K)	(K)	(km s $^{-1}$)	(km s $^{-1}$)	(km s $^{-1}$)	(km s $^{-1}$)	(M_{\odot})	(14)	(15)
(2)	(3)	(4)	(5)	(6)	(7)	(8)	(9)	(10)	(11)	(12)	(13)	(14)	(15)	
1	17:45:36.41, -29:06:30.01	0.4	1290	-	-	-	-	-	-	-	-	0.71	-	-
2	17:45:36.53, -29:06:29.63	0.27	1040	-	-	-	-	-	-	-	-	0.36	-	-
3	17:45:36.53, -29:06:29.38	0.33	1240	-	-	-	-	-	-	-	-	0.51	-	-
4	17:45:36.23, -29:06:29.28	0.34	1330	-	-	-	-	-	-	-	-	0.55	-	-
5	17:45:36.27, -29:06:28.57	0.25	1360	-	-	-	-	-	-	-	-	0.52	-	-
6	17:45:36.64, -29:06:26.83	0.86	1720	101.5 \pm 49.7	125 \pm 61	-	101.5 \pm 49.7	2.39 \pm 0.37	2.99 \pm 0.96	-	2.39 \pm 0.37	0.21	3.90 \pm 0.70	6.12
7	17:45:36.34, -29:06:26.57	0.26	1200	-	-	-	-	-	-	-	-	0.42	-	-
8	17:45:36.70, -29:06:24.69	0.5	1790	61.2 \pm 20.4	69.1 \pm 3.1	-	61.2 \pm 20.4	3.43 \pm 0.51	3 \pm 1	-	3.43 \pm 0.51	0.21	7.34 \pm 1.18	11.18
9	17:45:36.41, -29:06:24.27	0.33	1590	-	-	-	-	-	-	-	-	0.71	-	-
10	17:45:36.31, -29:06:23.97	0.35	1290	-	-	-	-	-	-	-	-	0.46	-	-
11	17:45:36.41, -29:06:23.50	1.07	1240	-	-	-	-	-	-	-	-	0.44	-	-
12	17:45:36.43, -29:06:23.15	0.77	1860	-	-	-	-	-	-	-	-	1.04	-	-
13	17:45:36.45, -29:06:21.89	0.58	2060	-	-	-	-	-	-	-	-	1.15	-	-
14	17:45:36.39, -29:06:21.73	0.26	1830	-	-	-	-	-	-	-	-	0.93	-	-
15	17:45:36.47, -29:06:21.52	0.25	1180	-	-	-	-	-	-	-	-	0.38	-	-
16	17:45:36.50, -29:06:20.75	6.44	1120	-	-	-	-	-	-	-	-	0.35	-	-
17	17:45:36.07, -29:06:20.49	0.32	2950	-	-	-	-	-	-	-	-	11.17	-	-
18	17:45:36.20, -29:06:20.24	9.35	1250	-	-	-	-	-	-	-	-	0.52	-	-
19	17:45:36.35, -29:06:19.20	0.45	4490	-	90 \pm 7.4	90 \pm 7.4	-	-	2.06 \pm 0.1	2.06 \pm 0.1	0.12	3.53 \pm 0.19	0.16	
20	17:45:36.68, -29:06:19.65	0.32	1480	-	-	-	-	-	-	-	-	0.66	-	-
21	17:45:36.61, -29:06:19.60	3.51	1180	-	-	-	-	-	-	-	-	0.46	-	-
22	17:45:36.25, -29:06:19.22	0.25	2370	-	-	-	-	-	-	-	-	5.78	-	-
23	17:45:36.89, -29:06:19.19	0.29	1060	-	-	-	-	-	-	-	-	0.33	-	-
24	17:45:36.52, -29:06:19.16	0.7	1330	-	-	-	-	-	-	-	-	0.66	-	-
25	17:45:36.65, -29:06:19.13	0.33	1120	-	-	-	-	-	-	-	-	1.02	-	-
26	17:45:36.48, -29:06:18.72	0.32	3710	-	-	-	-	-	-	-	-	5.83	-	-
27	17:45:36.86, -29:06:18.92	2.55	1310	-	-	-	-	-	-	-	-	0.51	-	-
28	17:45:36.64, -29:06:18.76	2.05	1630	111.2 \pm 49	158 \pm 40	-	111.2 \pm 49	5.33 \pm 0.63	3.51 \pm 0.49	-	5.33 \pm 0.63	0.45	8.53 \pm 1.16	56.25
29	17:45:36.71, -29:06:18.48	2.23	2830	109.6 \pm 25.9	185 \pm 56	-	109.6 \pm 25.9	3.8 \pm 0.25	3.73 \pm 0.57	-	3.8 \pm 0.25	0.50	6.09 \pm 0.46	8.43
30	17:45:32.92, -29:06:18.69	0.48	1560	173.9 \pm 87	193 \pm 37	-	173.9 \pm 87	3.57 \pm 0.33	3.41 \pm 0.28	-	3.57 \pm 0.33	0.07	4.53 \pm 0.54	6.64
31	17:45:36.93, -29:06:18.50	2.08	2250	149.9 \pm 89	80.8 \pm 3.4	76.4 \pm 13.3	76.4 \pm 13.3	2.56 \pm 0.33	1.85 \pm 0.33	1.73 \pm 0.16	1.73 \pm 0.16	0.32	5.17 \pm 0.49	5.11
32	17:45:36.07, -29:06:18.01	1.58	2060	112.1 \pm 47.7	172 \pm 73	-	112.1 \pm 47.7	5.87 \pm 0.66	5.9 \pm 1.5	-	5.87 \pm 0.66	0.34	9.37 \pm 1.21	34.08

Table E3 *continued*

Table E3 (*continued*)

Core ID	RA and Dec	Flux	R	$T_{\text{H}_2\text{CO}}$	$T_{\text{H}_2\text{CO}}$	$T_{\text{CH}_3\text{CN}}$	T	$\sigma_{\text{H}_2\text{CO}}$	$\sigma_{\text{H}_2\text{CO}}$	$\sigma_{\text{CH}_3\text{CN}}$	σ	M_{core}	\mathcal{M}	$\alpha_{\text{vir},p}$
		density		LTE	non-LTE	LTE		LTE	non-LTE	LTE				
(1)	(J2000)	(mJy)	(AU)	(K)	(K)	(K)	(K)	(km s $^{-1}$)	(km s $^{-1}$)	(km s $^{-1}$)	(km s $^{-1}$)	(M_{\odot})	(14)	(15)
(2)		(3)	(4)	(5)	(6)	(7)	(8)	(9)	(10)	(11)	(12)	(13)		
33	17:45:36.93, -29:06:18.17	0.25	1030	-	-	-	-	-	-	-	-	0.38	-	-
34	17:45:36.38, -29:06:18.04	0.4	1490	75.9±24.8	73±20	-	75.9±24.8	1.96±0.27	2.18±0.55	-	1.96±0.27	0.13	3.64±0.58	3.93
35	17:45:36.82, -29:06:17.64	15.52	3440	94.9±30.9	138±10	-	94.9±30.9	3.7±0.39	3.61±0.46	-	3.7±0.39	4.03	6.37±0.75	12.99
36	17:45:36.68, -29:06:17.97	0.55	1320	-	-	-	-	-	-	-	-	0.83	-	-
37	17:45:36.64, -29:06:17.72	1.62	2000	45.8±12.7	69±11	-	<94.3	3.17±0.45	3.1±1.1	-	3.17±0.45	<0.42	7.82±1.19	16.99
38	17:45:36.35, -29:06:17.62	0.21	1140	99.8±36.2	53.8±0.9	-	99.8±36.2	1.98±0.24	1.94±0.39	-	1.98±0.24	0.05	3.21±0.46	3.63
39	17:45:36.88, -29:06:17.17	6.32	3420	99.3±37.8	104±14	-	99.3±37.8	3.18±0.38	3.1±0.52	-	3.18±0.38	1.56	5.32±0.72	8.55
40	17:45:33.22, -29:06:17.48	0.27	1150	-	-	-	-	-	-	-	-	0.66	-	-
41	17:45:36.65, -29:06:17.17	0.4	1030	-	-	-	-	-	-	-	-	0.56	-	-
42	17:45:36.55, -29:06:17.07	0.33	1370	-	-	-	-	-	-	-	-	0.55	-	-
43	17:45:36.67, -29:06:16.56	3.95	2260	88.5±30.5	65.6±4.6	-	88.5±30.5	2.61±0.32	2.77±0.75	-	2.61±0.32	1.10	4.59±0.64	10.24
44	17:45:36.94, -29:06:16.60	0.33	1090	-	-	-	-	-	-	-	-	0.49	-	-
45	17:45:36.56, -29:06:16.33	1.99	3000	-	-	-	-	-	-	-	-	3.17	-	-
46	17:45:33.01, -29:06:16.51	0.19	1040	-	-	-	-	-	-	-	-	0.66	-	-
47	17:45:37.00, -29:06:16.37	0.26	1150	-	-	-	-	-	-	-	-	0.44	-	-
48	17:45:33.88, -29:06:16.09	1.08	1120	-	-	-	-	-	-	-	-	0.59	-	-
49	17:45:33.92, -29:06:16.00	0.61	1630	73.7±21.6	69±12	-	<92.3	2.47±0.3	2.02±0.52	-	2.47±0.3	<0.16	4.74±0.64	7.42
50	17:45:36.65, -29:06:15.88	1.79	1650	157±80.9	133±75	-	157±80.9	1.42±0.17	1.44±0.36	-	1.42±0.17	0.27	1.74±0.29	3.19
51	17:45:36.28, -29:06:15.97	0.23	1150	-	-	-	-	-	-	-	-	0.43	-	-
52	17:45:33.95, -29:06:15.64	2.63	2920	49.2±8.4	66±39	-	49.2±8.4	1.39±0.15	1.3±0.36	-	1.39±0.15	1.39	3.05±0.41	1.92
53	17:45:33.07, -29:06:15.54	2.56	2880	-	-	-	-	-	-	-	-	8.33	-	-
54	17:45:36.58, -29:06:15.77	0.54	1490	-	-	-	-	-	-	-	-	0.91	-	-
55	17:45:36.55, -29:06:14.80	0.96	1710	166.3±125.5	137±11	-	166.3±125.5	2.35±0.35	2.49±0.77	-	2.35±0.35	0.14	1.58±0.55	1.54
56	17:45:33.91, -29:06:14.39	1.98	3020	68.5±15	53±47	-	68.5±15	1.52±0.17	1.64±0.67	-	1.52±0.17	0.73	2.87±0.39	1.48
57	17:45:34.52, -29:06:14.38	0.26	1090	-	-	-	-	-	-	-	-	0.55	-	-
58	17:45:33.92, -29:06:13.63	0.36	1290	100.1±43.5	77±4.5	-	100.1±43.5	1.33±0.21	1.63±0.45	-	1.33±0.21	0.09	2.02±0.42	1.98
59	17:45:33.95, -29:06:13.51	0.34	1320	76.9±40.3	53±7.4	-	76.9±40.3	1.61±0.37	1.45±0.48	-	1.61±0.37	0.11	2.90±0.80	3.17
60	17:45:33.91, -29:06:13.27	0.38	1290	108.8±54.6	77±17	-	108.8±54.6	1.34±0.23	1.64±0.55	-	1.34±0.23	0.09	1.95±0.44	2.05
61	17:45:33.92, -29:06:13.06	0.45	1330	86.4±31.2	53±46	-	86.4±31.2	1.4±0.21	1.45±0.25	-	1.4±0.21	0.13	2.32±0.44	2.73
62	17:45:36.60, -29:06:12.78	3.09	2940	-	-	-	-	-	-	-	-	5.83	-	-
63	17:45:33.94, -29:06:11.92	0.89	2180	-	-	-	-	-	-	-	-	1.74	-	-
64	17:45:33.20, -29:06:08.94	0.4	1460	-	-	-	-	-	-	-	-	1.24	-	-
65	17:45:36.52, -29:06:08.15	1.81	2230	63.7±16.4	81±22	-	63.7±16.4	2.17±0.27	2.3±1.5	-	2.17±0.27	0.72	4.44±0.62	6.21
66	17:45:34.95, -29:06:06.89	1.83	2280	-	-	-	-	-	-	-	-	6.35	-	-
67	17:45:35.84, -29:06:06.03	0.65	1630	-	-	-	-	-	-	-	-	1.87	-	-
68	17:45:35.16, -29:06:03.01	5.97	2720	-	-	-	-	-	-	-	-	17.17	-	-
69	17:45:34.65, -29:06:03.02	0.69	1710	-	-	-	-	-	-	-	-	2.33	-	-
70	17:45:36.81, -29:06:02.50	0.23	1120	-	-	-	-	-	-	-	-	0.59	-	-
71	17:45:34.84, -29:06:02.41	0.56	1370	-	-	-	-	-	-	-	-	1.72	-	-
72	17:45:36.19, -29:06:01.90	4.08	2810	-	-	-	-	-	-	-	-	9.21	-	-
73	17:45:36.87, -29:06:01.31	2.68	2160	-	-	-	-	-	-	-	-	7.08	-	-
74	17:45:35.32, -29:06:00.04	0.48	1340	-	-	-	-	-	-	-	-	1.10	-	-
75	17:45:36.97, -29:05:59.52	0.22	1060	-	-	-	-	-	-	-	-	0.51	-	-
76	17:45:37.03, -29:05:58.77	1.8	2880	-	-	-	-	-	-	-	-	4.38	-	-
77	17:45:37.17, -29:05:58.34	0.46	1520	-	-	-	-	-	-	-	-	1.11	-	-
78	17:45:36.99, -29:05:58.10	0.97	2270	-	-	-	-	-	-	-	-	2.25	-	-
79	17:45:37.09, -29:05:58.00	0.54	1360	-	-	-	-	-	-	-	-	0.83	-	-
80	17:45:37.06, -29:05:58.09	0.5	1330	-	-	-	-	-	-	-	-	0.90	-	-
81	17:45:34.74, -29:05:57.99	0.21	1540	-	-	-	-	-	-	-	-	1.69	-	-
82	17:45:35.50, -29:05:58.04	0.26	1040	66.8±25.8	52±12	-	<109.7	1.23±0.25	1.3±0.44	-	1.23±0.25	<0.06	2.24±0.60	0.71
83	17:45:35.58, -29:05:57.82	0.95	2210	161.6±124	125±29	-	161.6±124	1.01±0.16	1.03±0.65	-	1.01±0.16	0.14	1.07±0.29	0.09
84	17:45:35.00, -29:05:57.53	0.48	1380	-	-	-	-	-	-	-	-	1.17	-	-
85	17:45:35.55, -29:05:57.21	0.65	1500	-	-	-	-	-	-	-	-	1.12	-	-
86	17:45:35.49, -29:05:57.04	2.5	2180	150.3±78.4	105±83	-	150.3±78.4	1.35±0.17	1.18±0.36	-	1.35±0.17	0.40	1.67±0.29	0.44
87	17:45:34.65, -29:05:57.04	1	1820	-	-	-	-	-	-	-	-	3.42	-	-
88	17:45:35.42, -29:05:56.74	10.77	3570	-	-	-	-	-	-	-	-	20.16	-	-
89	17:45:34.78, -29:05:56.92	0.47	1540	-	-	-	-	-	-	-	-	1.36	-	-
90	17:45:35.55, -29:05:56.57	3.86	2980	-	-	-	-	-	-	-	-	6.73	-	-
91	17:45:35.24, -29:05:56.78	1.12	1940	-	-	-	-	-	-	-	-	2.28	-	-
92	17:45:35.28, -29:05:56.73	0.31	1030	-	-	-	-	-	-	-	-	0.59	-	-
93	17:45:34.65, -29:05:56.47	0.8	1910	-	-	-	-	-	-	-	-	2.65	-	-
94	17:45:37.12, -29:05:55.96	3.03	2790	-	-	-	-	-	-	-	-	6.39	-	-

Table E3 *continued*

Table E3 (*continued*)

Core ID	RA and Dec	Flux	R	$T_{\text{H}_2\text{CO}}$	$T_{\text{H}_2\text{CO}}$	$T_{\text{CH}_3\text{CN}}$	T	$\sigma_{\text{H}_2\text{CO}}$	$\sigma_{\text{H}_2\text{CO}}$	$\sigma_{\text{CH}_3\text{CN}}$	σ	M_{core}	\mathcal{M}	$\alpha_{\text{vir},p}$
		density		LTE	non-LTE	LTE		LTE	non-LTE	LTE				
(1)	(J2000)	(mJy)	(AU)	(K)	(K)	(K)	(K)	(km s $^{-1}$)	(km s $^{-1}$)	(km s $^{-1}$)	(km s $^{-1}$)	(M_{\odot})	(14)	(15)
(2)		(3)	(4)	(5)	(6)	(7)	(8)	(9)	(10)	(11)	(12)	(13)		
95	17:45:35.28, -29:05:55.51	16.53	5270	-	-	-	-	-	-	-	-	32.84	-	-
96	17:45:35.50, -29:05:55.91	6.76	1520	123.5±49.9	109±52	-	123.5±49.9	2.77±0.29	2.44±0.42	-	2.77±0.29	1.33	4.13±0.51	7.99
97	17:45:35.43, -29:05:55.72	0.5	2950	-	-	-	-	-	-	-	-	12.27	-	-
98	17:45:35.57, -29:05:55.44	1.31	2540	95±36	125±29	-	95±36	2.71±0.34	3±1.3	-	2.71±0.34	0.34	4.61±0.66	0.88
99	17:45:35.51, -29:05:55.06	2.55	3040	190.2±100.4	109±40	-	190.2±100.4	4.97±0.44	5±1.7	-	4.97±0.44	0.32	6.07±0.72	1.66
100	17:45:37.10, -29:05:54.65	2.95	3040	84.9±33.6	73±15	-	84.9±33.6	1.78±0.27	2±1	-	1.78±0.27	0.86	3.09±0.56	0.54
101	17:45:35.16, -29:05:54.59	6.56	2960	140.7±98.3	180±120	-	140.7±98.3	1.89±0.31	2.1±1.1	-	1.89±0.31	1.13	2.56±0.53	0.89
102	17:45:35.23, -29:05:54.73	0.89	1490	-	-	-	-	-	-	-	-	1.74	-	-
103	17:45:37.24, -29:05:54.53	1.4	2480	-	-	-	-	-	-	-	-	2.84	-	-
104	17:45:35.58, -29:05:54.50	0.26	1110	-	-	-	-	-	-	-	-	0.37	-	-
105	17:45:35.34, -29:05:54.50	1.01	1530	-	-	-	-	-	-	-	-	1.98	-	-
106	17:45:35.47, -29:05:54.18	3.16	1820	-	-	-	-	-	-	-	-	5.45	-	-
107	17:45:37.48, -29:05:53.77	3.84	3170	-	-	-	-	-	-	-	-	8.39	-	-
108	17:45:35.29, -29:05:54.10	2.4	2280	-	-	-	-	-	-	-	-	4.63	-	-
109	17:45:36.15, -29:05:53.95	2.12	2230	-	-	-	-	-	-	-	-	3.34	-	-
110	17:45:35.52, -29:05:53.80	7.7	2220	-	-	-	-	-	-	-	-	13.43	-	-
111	17:45:35.42, -29:05:53.59	1.16	2180	-	-	-	-	-	-	-	-	2.16	-	-
112	17:45:35.48, -29:05:53.45	1.78	1580	93.5±45.1	73±12	-	93.5±45.1	1.99±0.34	2.21±0.78	-	1.99±0.34	0.47	3.33±0.67	2.44
113	17:45:35.18, -29:05:53.48	1.48	1060	-	-	-	-	-	-	-	-	3.14	-	-
114	17:45:35.15, -29:05:53.32	2.79	1370	-	-	-	-	-	-	-	-	6.15	-	-
115	17:45:35.47, -29:05:52.95	2.59	3050	-	-	-	-	-	-	-	-	3.90	-	-
116	17:45:36.03, -29:05:53.25	0.46	1520	-	-	-	-	-	-	-	-	0.68	-	-
117	17:45:35.52, -29:05:53.25	0.57	1490	-	-	-	-	-	-	-	-	1.05	-	-
118	17:45:37.40, -29:05:53.22	0.93	1530	-	-	-	-	-	-	-	-	1.84	-	-
119	17:45:37.12, -29:05:52.94	3.04	2710	-	-	-	-	-	-	-	-	5.41	-	-
120	17:45:35.40, -29:05:52.63	4.04	3250	62±14.9	53±7.7	-	62±14.9	6.12±0.59	5±1	-	6.12±0.59	7.36	13.14±1.36	9.73
121	17:45:37.17, -29:05:52.86	0.34	1320	-	-	-	-	-	-	-	-	0.58	-	-
122	17:45:36.06, -29:05:53.02	0.31	1040	-	-	-	-	-	-	-	-	0.42	-	-
123	17:45:36.06, -29:05:52.46	1.46	2230	-	-	-	-	-	-	-	-	2.19	-	-
124	17:45:35.10, -29:05:52.48	2.43	2310	37.2±9.8	32±30	-	<96.3	1.87±0.3	1.9±1.1	-	1.87±0.3	<0.62	4.95±0.90	2.00
125	17:45:37.20, -29:05:52.53	1.2	2280	-	-	-	-	-	-	-	-	2.07	-	-
126	17:45:35.01, -29:05:51.62	0.92	1680	-	-	-	-	-	-	-	-	1.94	-	-
127	17:45:36.48, -29:05:51.40	2.06	2450	-	-	-	-	-	-	-	-	2.99	-	-
128	17:45:37.49, -29:05:51.40	0.58	1620	-	-	-	-	-	-	-	-	1.03	-	-
129	17:45:35.04, -29:05:51.25	0.56	1490	-	-	-	-	-	-	-	-	1.05	-	-
130	17:45:36.01, -29:05:51.21	0.37	1340	-	-	-	-	-	-	-	-	0.56	-	-
131	17:45:34.95, -29:05:50.71	8.49	4140	-	-	-	-	-	-	-	-	20.85	-	-
132	17:45:36.04, -29:05:51.10	1.4	1340	-	-	-	-	-	-	-	-	0.64	-	-
133	17:45:36.44, -29:05:50.87	0.88	1660	54.2±16.1	106±80	-	54.2±16.1	2.07±0.33	2.59±0.99	-	2.07±0.33	0.42	4.58±0.82	7.20
134	17:45:36.05, -29:05:50.77	0.42	1500	-	-	-	-	-	-	-	-	0.64	-	-
135	17:45:37.45, -29:05:50.15	1.08	2140	-	-	-	-	-	-	-	-	1.80	-	-
136	17:45:36.53, -29:05:50.02	0.75	2000	-	-	-	-	-	-	-	-	1.16	-	-
137	17:45:36.34, -29:05:49.81	25.49	2650	-	-	538.0±91.4	538.0±91.4	-	-	3.86±0.16	3.86±0.16	2.08	3.36±0.17	15.26
138	17:45:37.51, -29:05:49.57	0.23	2920	-	-	-	-	-	-	-	-	2.98	-	-
139	17:45:36.03, -29:05:49.69	0.43	1630	-	-	-	-	-	-	-	-	0.90	-	-
140	17:45:37.43, -29:05:49.67	1.21	1910	-	-	-	-	-	-	-	-	1.35	-	-
141	17:45:36.30, -29:05:49.76	2.36	1140	-	-	-	-	-	-	-	-	3.31	-	-
142	17:45:37.46, -29:05:49.58	1.09	1040	-	-	-	-	-	-	-	-	0.37	-	-
143	17:45:36.50, -29:05:49.30	2.85	2450	-	-	-	-	-	-	-	-	4.42	-	-
144	17:45:36.22, -29:05:49.26	4.43	2350	-	-	-	-	-	-	-	-	6.76	-	-
145	17:45:36.03, -29:05:49.16	1.08	2000	-	-	-	-	-	-	-	-	1.51	-	-
146	17:45:37.23, -29:05:49.29	2.8	1800	-	-	-	-	-	-	-	-	4.54	-	-
147	17:45:36.44, -29:05:49.32	0.62	1220	-	-	-	-	-	-	-	-	0.80	-	-
148	17:45:36.27, -29:05:48.74	2.75	2540	-	-	-	-	-	-	-	-	4.20	-	-
149	17:45:37.58, -29:05:48.89	0.82	1950	-	-	-	-	-	-	-	-	1.33	-	-
150	17:45:37.20, -29:05:48.98	1.15	1530	-	-	-	-	-	-	-	-	1.81	-	-
151	17:45:36.58, -29:05:48.66	4.8	3150	-	-	-	-	-	-	-	-	7.30	-	-
152	17:45:36.17, -29:05:48.38	22.19	4600	-	-	-	-	-	-	-	-	35.14	-	-
153	17:45:35.42, -29:05:48.64	0.97	2160	-	-	-	-	-	-	-	-	1.87	-	-
154	17:45:36.64, -29:05:48.50	3.35	2840	90.3±39.1	53±15	-	90.3±39.1	1.62±0.27	1.73±0.87	-	1.62±0.27	0.92	2.69±0.55	2.23
155	17:45:37.45, -29:05:48.28	4.65	3520	68.7±22.5	101±31	-	68.7±22.5	1.98±0.3	2.18±0.83	-	1.98±0.3	1.71	3.87±0.67	2.98
156	17:45:36.00, -29:05:48.46	0.72	1790	-	-	-	-	-	-	-	-	1.16	-	-

Table E3 *continued*

Table E3 (*continued*)

Core ID	RA and Dec	Flux	R	$T_{\text{H}_2\text{CO}}$	$T_{\text{H}_2\text{CO}}$	$T_{\text{CH}_3\text{CN}}$	T	$\sigma_{\text{H}_2\text{CO}}$	$\sigma_{\text{H}_2\text{CO}}$	$\sigma_{\text{CH}_3\text{CN}}$	σ	M_{core}	\mathcal{M}	$\alpha_{\text{vir},p}$
		density		LTE	non-LTE	LTE		LTE	non-LTE	LTE				
(1)	(J2000)	(mJy)	(AU)	(K)	(K)	(K)	(K)	(km s $^{-1}$)	(km s $^{-1}$)	(km s $^{-1}$)	(km s $^{-1}$)	(M_{\odot})	(14)	(15)
(2)		(3)	(4)	(5)	(6)	(7)	(8)	(9)	(10)	(11)	(12)	(13)		
157	17:45:37.34, -29:05:48.23	1.25	2500	-	-	-	-	-	-	-	-	1.93	-	-
158	17:45:37.73, -29:05:48.00	0.23	1090	-	-	-	-	-	-	-	-	0.38	-	-
159	17:45:37.61, -29:05:47.88	0.91	1710	134.9 \pm 88.5	140 \pm 130	-	134.9 \pm 88.5	2.05 \pm 0.33	2.05 \pm 0.98	-	2.05 \pm 0.33	0.16	2.86 \pm 0.57	3.39
160	17:45:36.30, -29:05:48.01	0.4	1420	-	-	-	-	-	-	-	-	0.59	-	-
161	17:45:37.68, -29:05:47.97	0.28	1290	-	-	-	-	-	-	-	-	0.49	-	-
162	17:45:37.75, -29:05:47.51	1.05	2150	-	-	-	-	-	-	-	-	1.73	-	-
163	17:45:37.52, -29:05:47.61	1.07	1670	81.4 \pm 23	80 \pm 56	-	81.4 \pm 23	1.96 \pm 0.22	2.1 \pm 1.2	-	1.96 \pm 0.22	0.33	3.52 \pm 0.46	5.67
164	17:45:36.04, -29:05:47.22	5.05	3530	-	-	-	-	-	-	-	-	8.23	-	-
165	17:45:37.46, -29:05:47.27	0.9	1690	-	-	-	-	-	-	-	-	1.35	-	-
166	17:45:37.52, -29:05:47.23	0.45	1110	-	-	-	-	-	-	-	-	0.61	-	-
167	17:45:36.74, -29:05:47.25	0.22	1030	-	-	-	-	-	-	-	-	0.31	-	-
168	17:45:36.60, -29:05:46.84	4.86	2630	76 \pm 17	53 \pm 31	-	76 \pm 17	1.57 \pm 0.16	1.49 \pm 0.45	-	1.57 \pm 0.16	1.60	2.83 \pm 0.35	2.97
169	17:45:36.13, -29:05:46.85	0.4	1650	-	-	-	-	-	-	-	-	0.80	-	-
170	17:45:36.74, -29:05:46.36	35.86	5970	-	-	149.9 \pm 30.4	149.9 \pm 30.4	-	-	2.76 \pm 0.29	2.76 \pm 0.29	56.22	3.71 \pm 0.30	0.83
171	17:45:37.74, -29:05:46.54	0.89	1840	-	-	-	-	-	-	-	-	1.49	-	-
172	17:45:35.33, -29:05:46.52	0.41	1250	-	-	-	-	-	-	-	-	0.84	-	-
173	17:45:37.23, -29:05:46.45	0.32	1080	-	-	-	-	-	-	-	-	0.46	-	-
174	17:45:37.18, -29:05:46.25	4	3350	-	-	-	-	-	-	-	-	6.02	-	-
175	17:45:36.87, -29:05:46.23	3.12	2620	73.5 \pm 16.3	67 \pm 16	-	73.5 \pm 16.3	1.76 \pm 0.17	1.74 \pm 0.65	-	1.76 \pm 0.17	1.06	3.28 \pm 0.37	0.70
176	17:45:37.38, -29:05:46.11	0.47	1640	-	-	-	-	-	-	-	-	0.72	-	-
177	17:45:37.61, -29:05:46.23	1.28	1610	57.9 \pm 11.1	78 \pm 47	-	57.9 \pm 11.1	1.31 \pm 0.15	1.52 \pm 0.58	-	1.31 \pm 0.15	0.57	2.61 \pm 0.38	0.80
178	17:45:37.27, -29:05:46.05	1.71	2500	-	-	-	-	-	-	-	-	2.58	-	-
179	17:45:37.78, -29:05:46.04	0.5	1280	-	-	-	-	-	-	-	-	0.76	-	-
180	17:45:37.74, -29:05:46.94	0.44	1440	59.6 \pm 15.8	49.5 \pm 3.5	-	59.6 \pm 15.8	2.43 \pm 0.31	2.22 \pm 0.72	-	2.43 \pm 0.31	0.19	5.19 \pm 0.73	1.51
181	17:45:37.05, -29:05:45.86	1.93	2030	-	-	-	-	-	-	-	-	2.97	-	-
182	17:45:36.59, -29:05:46.01	0.21	1040	-	-	-	-	-	-	-	-	0.33	-	-
183	17:45:36.99, -29:05:45.87	0.65	1680	-	-	-	-	-	-	-	-	0.96	-	-
184	17:45:37.45, -29:05:45.88	0.34	1180	-	-	-	-	-	-	-	-	0.61	-	-
185	17:45:36.61, -29:05:45.75	0.46	1590	43.7 \pm 10.5	63 \pm 45	-	43.7 \pm 10.5	2.93 \pm 0.38	3 \pm 1	-	2.93 \pm 0.38	0.28	7.38 \pm 1.03	4.57
186	17:45:36.04, -29:05:45.77	0.39	1410	-	-	-	-	-	-	-	-	0.66	-	-
187	17:45:37.84, -29:05:45.70	1.34	1360	-	-	-	-	-	-	-	-	2.04	-	-
188	17:45:37.30, -29:05:45.48	0.49	1420	-	-	-	-	-	-	-	-	0.73	-	-
189	17:45:37.50, -29:05:45.51	1.51	1430	176.1 \pm 89.8	80.8 \pm 1.5	,	176.1 \pm 89.8	1.45 \pm 0.15	1.59 \pm 0.34	-	1.45 \pm 0.15	0.21	1.68 \pm 0.25	1.03
190	17:45:38.01, -29:05:45.38	0.43	1480	-	-	-	-	-	-	-	-	0.73	-	-
191	17:45:37.22, -29:05:45.23	0.6	1660	-	-	-	-	-	-	-	-	0.89	-	-
192	17:45:36.01, -29:05:45.20	0.48	1590	-	-	-	-	-	-	-	-	0.82	-	-
193	17:45:37.87, -29:05:45.20	4.38	1210	-	-	-	-	-	-	-	-	6.57	-	-
194	17:45:37.49, -29:05:44.25	57.91	5170	67.8 \pm 12.2	53 \pm 2.9	127.3 \pm 19.9	127.3 \pm 19.9	1.34 \pm 0.13	2.99 \pm 0.67	4.89 \pm 0.36	4.89 \pm 0.36	11.49	6.66 \pm 0.51	0.51
195	17:45:37.90, -29:05:44.84	6.48	1430	-	-	-	-	-	-	-	-	10.37	-	-
196	17:45:37.81, -29:05:44.88	0.91	1250	-	-	-	-	-	-	-	-	1.76	-	-
197	17:45:36.80, -29:05:44.37	3.37	3760	92.8 \pm 35.6	53 \pm 4.5	-	92.8 \pm 35.6	1.59 \pm 0.23	1.81 \pm 0.51	-	1.59 \pm 0.23	0.90	2.60 \pm 0.46	0.34
198	17:45:36.94, -29:05:44.76	0.22	1110	-	-	-	-	-	-	-	-	0.36	-	-
199	17:45:36.91, -29:05:44.35	1.49	3190	-	-	-	-	-	-	-	-	3.42	-	-
200	17:45:37.62, -29:05:44.62	0.77	1110	-	-	-	-	-	-	-	-	10.43	-	-
201	17:45:37.78, -29:05:44.54	6.97	1080	-	-	-	-	-	-	-	-	1.25	-	-
202	17:45:37.92, -29:05:44.41	12.19	1930	-	-	-	-	-	-	-	-	19.81	-	-
203	17:45:37.63, -29:05:44.28	19.55	1620	-	-	509.2 \pm 83.0	509.2 \pm 83.0	-	-	4.43 \pm 0.18	4.43 \pm 0.18	0.79	3.41 \pm 0.16	16.21
204	17:45:37.07, -29:05:43.93	0.63	1560	-	-	-	-	-	-	-	-	0.97	-	-
205	17:45:37.13, -29:05:43.80	2.84	2240	-	-	-	-	-	-	-	-	4.36	-	-
206	17:45:37.87, -29:05:43.59	8.99	2070	-	-	-	-	-	-	-	-	14.54	-	-
207	17:45:37.96, -29:05:43.55	1.32	1740	-	-	-	-	-	-	-	-	2.15	-	-
208	17:45:37.77, -29:05:43.59	3.81	1590	-	-	-	-	-	-	-	-	5.78	-	-
209	17:45:37.19, -29:05:43.56	2.91	1620	74.6 \pm 30.1	53 \pm 5.8	-	74.6 \pm 30.1	2.1 \pm 0.36	2.5 \pm 0.7	-	2.1 \pm 0.36	0.98	3.96 \pm 0.77	4.74
210	17:45:37.22, -29:05:43.32	3.97	2090	-	-	-	-	-	-	-	-	6.06	-	-
211	17:45:36.90, -29:05:43.10	1.98	2280	-	-	-	-	-	-	-	-	3.19	-	-
212	17:45:37.87, -29:05:43.16	2.62	1200	-	-	-	-	-	-	-	-	3.84	-	-
213	17:45:37.76, -29:05:42.93	10.7	2430	-	-	-	-	-	-	-	-	16.12	-	-
214	17:45:37.51, -29:05:42.98	0.5	1040	85.3 \pm 34.2	53 \pm 2.1	-	85.3 \pm 34.2	1.07 \pm 0.18	1.64 \pm 0.44	-	1.07 \pm 0.18	0.15	1.64 \pm 0.41	1.04
215	17:45:37.59, -29:05:42.63	12.33	2380	136.9 \pm 44.2	140 \pm 26	186.3 \pm 32.6	186.3 \pm 32.6	1.84 \pm 0.15	2.34 \pm 0.68	6.01 \pm 0.48	6.01 \pm 0.48	1.58	7.44 \pm 0.63	2.62
216	17:45:37.68, -29:05:42.39	0.25	1080	-	-	-	-	-	-	-	-	4.93	-	-
217	17:45:37.90, -29:05:42.33	3.37	1200	-	-	-	-	-	-	-	-	0.39	-	-
218	17:45:37.65, -29:05:42.31	6.88	1430	71.1 \pm 23.6	83 \pm 18	-	71.1 \pm 23.6	1.44 \pm 0.24	1.51 \pm 0.36	-	1.44 \pm 0.24	2.43	2.65 \pm 0.54	1.70

Table E3 continued

Table E3 (*continued*)

Core ID	RA and Dec	Flux	R	$T_{\text{H}_2\text{CO}}$	$T_{\text{H}_2\text{CO}}$	$T_{\text{CH}_3\text{CN}}$	T	$\sigma_{\text{H}_2\text{CO}}$	$\sigma_{\text{H}_2\text{CO}}$	$\sigma_{\text{CH}_3\text{CN}}$	σ	M_{core}	\mathcal{M}	$\alpha_{\text{vir},p}$
		density		LTE	non-LTE	LTE		LTE	non-LTE	LTE				
(1)	(J2000)	(mJy)	(AU)	(K)	(K)	(K)	(K)	(km s $^{-1}$)	(km s $^{-1}$)	(km s $^{-1}$)	(km s $^{-1}$)	(M_{\odot})	(14)	(15)
(2)	(3)	(4)	(5)	(6)	(7)	(8)	(9)	(10)	(11)	(12)	(13)			
219	17:45:37.60, -29:05:42.25	2.5	1490	87.1±17	50±8.2	-	87.1±17	2.32±0.17	2.42±0.49	-	2.32±0.17	0.71	4.08±0.34	5.99
220	17:45:37.42, -29:05:41.97	13.11	3380	-	-	-	-	-	-	-	-	20.29	-	-
221	17:45:37.85, -29:05:42.11	0.52	1610	-	-	-	-	-	-	-	-	0.88	-	-
222	17:45:37.13, -29:05:42.13	1.1	1540	-	-	-	-	-	-	-	-	1.69	-	-
223	17:45:37.17, -29:05:41.89	2.69	3880	-	-	-	-	-	-	-	-	27.72	-	-
224	17:45:37.35, -29:05:42.05	17.59	1580	-	-	-	-	-	-	-	-	3.91	-	-
225	17:45:37.88, -29:05:41.81	0.35	1280	-	-	-	-	-	-	-	-	0.73	-	-
226	17:45:37.37, -29:05:41.72	0.87	1170	-	-	-	-	-	-	-	-	1.43	-	-
227	17:45:37.96, -29:05:41.55	1.39	2000	-	-	-	-	-	-	-	-	2.27	-	-
228	17:45:37.85, -29:05:41.62	0.96	1570	-	-	-	-	-	-	-	-	1.50	-	-
229	17:45:37.45, -29:05:41.39	3.94	2270	-	-	-	-	-	-	-	-	5.98	-	-
230	17:45:38.14, -29:05:41.54	0.36	1280	-	-	-	-	-	-	-	-	0.61	-	-
231	17:45:37.27, -29:05:41.30	4.56	3110	-	-	-	-	-	-	-	-	7.36	-	-
232	17:45:38.18, -29:05:41.31	2.31	2490	-	-	-	-	-	-	-	-	3.92	-	-
233	17:45:37.54, -29:05:41.39	1.47	1860	24.8±7.3	33±33	-	<86.9	2.36±0.34	2.3±0.9	-	2.36±0.34	<0.42	7.80±1.24	5.18
234	17:45:37.91, -29:05:41.21	2.53	2240	-	-	-	-	-	-	-	-	5.92	-	-
235	17:45:37.36, -29:05:41.23	0.99	1310	-	-	-	-	-	-	-	-	1.43	-	-
236	17:45:37.76, -29:05:41.23	0.44	1460	-	-	-	-	-	-	-	-	0.65	-	-
237	17:45:37.73, -29:05:40.79	0.71	2250	-	-	-	-	-	-	-	-	2.71	-	-
238	17:45:37.40, -29:05:40.86	3.18	2430	96.8±20.2	53±16	-	96.8±20.2	6.43±0.4	6.4±1.4	-	6.43±0.4	0.81	11.05±0.77	16.68
239	17:45:37.93, -29:05:40.74	0.78	1200	-	-	-	-	-	-	-	-	1.30	-	-
240	17:45:37.77, -29:05:40.70	0.43	1060	-	-	-	-	-	-	-	-	0.58	-	-
241	17:45:37.97, -29:05:40.12	10.89	3910	114.7±42.2	158±99	-	114.7±42.2	2.51±0.26	2.41±0.89	-	2.51±0.26	2.32	3.86±0.47	1.78
242	17:45:37.37, -29:05:40.43	1.34	1590	87.9±19.9	146±13	-	87.9±19.9	6.56±0.93	6.56±0.93	-	6.84±0.49	0.38	12.34±0.98	30.43
243	17:45:38.10, -29:05:40.38	0.44	1410	-	-	-	-	-	-	-	-	0.61	-	-
244	17:45:37.76, -29:05:40.21	0.68	1490	-	-	-	-	-	-	-	-	1.04	-	-
245	17:45:37.17, -29:05:40.12	0.87	2120	-	-	-	-	-	-	-	-	1.44	-	-
246	17:45:37.81, -29:05:40.16	0.31	1240	-	-	-	-	-	-	-	-	0.43	-	-
247	17:45:37.45, -29:05:39.88	1.17	2390	54.3±14.1	53±14	-	54.3±14.1	4.06±0.48	5±1.6	-	4.06±0.48	0.55	9.26±1.17	4.90
248	17:45:38.04, -29:05:39.84	0.92	1650	-	-	-	-	-	-	-	-	1.42	-	-
249	17:45:37.93, -29:05:39.72	1.62	1730	-	-	-	-	-	-	-	-	2.55	-	-
250	17:45:37.30, -29:05:39.77	1.16	1780	-	-	-	-	-	-	-	-	1.78	-	-
251	17:45:37.19, -29:05:39.76	0.35	1450	-	-	-	-	-	-	-	-	0.67	-	-
252	17:45:37.25, -29:05:39.51	1.61	2580	-	-	-	-	-	-	-	-	2.59	-	-
253	17:45:37.87, -29:05:39.39	0.38	1430	-	-	-	-	-	-	-	-	0.56	-	-
254	17:45:38.00, -29:05:39.33	0.68	1370	-	-	-	-	-	-	-	-	0.91	-	-
255	17:45:37.47, -29:05:38.60	9.47	4040	159.7±79.2	138±40	-	159.7±79.2	2.38±0.24	2.6±1.4	-	2.38±0.24	1.43	3.09±0.40	2.65
256	17:45:37.78, -29:05:38.29	6.4	4550	97.3±20.6	138±13	-	97.3±20.6	3.33±0.22	3.27±0.66	-	3.33±0.22	1.62	5.64±0.42	4.05
257	17:45:37.05, -29:05:38.78	0.23	1030	-	-	-	-	-	-	-	-	0.37	-	-
258	17:45:37.41, -29:05:38.57	2.43	1940	-	-	-	-	-	-	-	-	3.90	-	-
259	17:45:38.07, -29:05:38.41	0.48	1540	-	-	-	-	-	-	-	-	0.72	-	-
260	17:45:37.54, -29:05:37.87	1.13	1980	-	-	-	-	-	-	-	-	1.69	-	-
261	17:45:37.01, -29:05:37.06	1.02	2330	-	-	-	-	-	-	-	-	2.10	-	-
262	17:45:38.02, -29:05:37.08	0.41	1500	-	-	-	-	-	-	-	-	0.60	-	-
263	17:45:37.65, -29:05:36.86	0.38	1320	-	-	-	-	-	-	-	-	0.50	-	-
264	17:45:37.02, -29:05:36.56	0.3	1120	-	-	-	-	-	-	-	-	0.47	-	-
265	17:45:37.63, -29:05:36.43	0.22	1030	-	-	-	-	-	-	-	-	0.33	-	-
266	17:45:38.12, -29:05:35.67	1.01	2290	74.6±19.6	65±18	-	74.6±19.6	1.55±0.19	1.45±0.68	-	1.55±0.19	0.34	2.82±0.42	1.43
267	17:45:37.61, -29:05:35.67	1.23	2100	-	-	-	-	-	-	-	-	2.08	-	-
268	17:45:37.59, -29:05:35.32	0.31	1110	-	-	-	-	-	-	-	-	0.54	-	-
269	17:45:38.02, -29:05:34.59	22.43	5210	-	-	-	-	-	-	-	-	35.76	-	-
270	17:45:38.16, -29:05:34.25	2.18	2820	-	-	-	-	-	-	-	-	2.46	-	-
271	17:45:38.77, -29:05:34.05	1.1	1810	-	-	-	-	-	-	-	-	2.53	-	-
272	17:45:37.09, -29:05:34.04	0.32	1310	-	-	-	-	-	-	-	-	0.72	-	-
273	17:45:36.90, -29:05:34.03	0.25	1090	-	-	-	-	-	-	-	-	0.66	-	-
274	17:45:37.99, -29:05:33.66	0.34	1340	-	-	-	-	-	-	-	-	0.54	-	-
275	17:45:38.19, -29:05:33.53	0.36	1080	-	-	-	-	-	-	-	-	0.51	-	-
276	17:45:38.26, -29:05:33.38	0.27	1110	-	-	-	-	-	-	-	-	0.41	-	-
277	17:45:38.20, -29:05:33.24	0.52	1280	-	-	-	-	-	-	-	-	0.72	-	-
278	17:45:38.29, -29:05:33.00	0.33	1150	-	-	-	-	-	-	-	-	0.49	-	-
279	17:45:38.14, -29:05:32.94	3.42	1280	-	-	-	-	-	-	-	-	5.70	-	-
280	17:45:38.11, -29:05:32.81	2.58	1200	-	-	-	-	-	-	-	-	4.17	-	-

Table E3 *continued*

Table E3 (*continued*)

Core ID	RA and Dec	Flux	R	$T_{\text{H}_2\text{CO}}$	$T_{\text{H}_2\text{CO}}$	$T_{\text{CH}_3\text{CN}}$	T	$\sigma_{\text{H}_2\text{CO}}$	$\sigma_{\text{H}_2\text{CO}}$	$\sigma_{\text{CH}_3\text{CN}}$	σ	M_{core}	\mathcal{M}	$\alpha_{\text{vir},p}$
		density		LTE	non-LTE	LTE		LTE	non-LTE	LTE				
(1)	(J2000)	(mJy)	(AU)	(K)	(K)	(K)	(K)	(km s $^{-1}$)	(km s $^{-1}$)	(km s $^{-1}$)	(km s $^{-1}$)	(M_{\odot})	(14)	(15)
(2)	(3)	(4)	(5)	(6)	(7)	(8)	(9)	(10)	(11)	(12)	(13)	(14)	(15)	
281	17:45:38.32, -29:05:32.56	1.09	2250	-	-	-	-	-	-	-	-	2.02	-	-
282	17:45:38.21, -29:05:32.25	3.62	2870	54.6±13.7	53±7	-	54.6±13.7	1.41±0.21	1.51±0.47	-	1.41±0.21	1.71	2.95±0.54	1.93
283	17:45:38.35, -29:05:32.03	0.58	1630	-	-	-	-	-	-	-	-	0.98	-	-
284	17:45:38.40, -29:05:31.60	0.67	1890	-	-	-	-	-	-	-	-	1.15	-	-
285	17:45:38.16, -29:05:31.76	2.98	2330	-	-	-	-	-	-	-	-	4.56	-	-
286	17:45:38.37, -29:05:31.73	0.21	1030	-	-	-	-	-	-	-	-	0.34	-	-
287	17:45:37.69, -29:05:31.63	0.91	1950	-	-	-	-	-	-	-	-	1.58	-	-
288	17:45:38.32, -29:05:31.56	0.39	1310	-	-	-	-	-	-	-	-	0.59	-	-
289	17:45:38.12, -29:05:31.40	1.03	1710	-	-	-	-	-	-	-	-	2.06	-	-
290	17:45:37.80, -29:05:30.87	0.26	1140	-	-	-	-	-	-	-	-	0.43	-	-
291	17:45:38.48, -29:05:30.55	0.35	1390	90.4±26.5	91±30	-	90.4±26.5	1.48±0.17	1.41±0.42	-	1.48±0.17	0.10	2.42±0.35	1.78
292	17:45:38.20, -29:05:30.48	2.48	2130	-	-	-	-	-	-	-	-	4.30	-	-
293	17:45:38.54, -29:05:30.46	0.44	1450	-	-	-	-	-	-	-	-	0.87	-	-
294	17:45:38.70, -29:05:30.15	0.43	1440	-	-	-	-	-	-	-	-	0.93	-	-
295	17:45:38.15, -29:05:29.82	2.37	2580	-	-	-	-	-	-	-	-	4.06	-	-
296	17:45:38.23, -29:05:30.07	0.31	1080	-	-	-	-	-	-	-	-	0.37	-	-
297	17:45:37.80, -29:05:29.70	0.76	2070	-	-	-	-	-	-	-	-	1.36	-	-
298	17:45:38.41, -29:05:29.79	0.24	1140	-	-	-	-	-	-	-	-	0.41	-	-
299	17:45:38.36, -29:05:29.29	0.77	1900	-	-	-	-	-	-	-	-	1.32	-	-
300	17:45:38.17, -29:05:29.21	0.37	1040	-	-	-	-	-	-	-	-	0.61	-	-
301	17:45:38.46, -29:05:29.08	1.93	2630	72.1±28.3	125±30	-	72.1±28.3	1.12±0.21	1±1	-	1.12±0.21	0.67	1.90±0.51	0.17
302	17:45:38.20, -29:05:28.85	3.13	2740	-	-	-	-	-	-	-	-	5.51	-	-
303	17:45:38.49, -29:05:28.47	1.19	2050	72.7±29.6	125±80	-	72.7±29.6	1.64±0.31	2±1.4	-	1.64±0.31	0.41	3.05±0.69	0.51
304	17:45:38.58, -29:05:28.52	0.24	1110	-	-	-	-	-	-	-	-	0.46	-	-
305	17:45:38.34, -29:05:27.88	2.86	2770	-	-	-	-	-	-	-	-	5.28	-	-
306	17:45:38.40, -29:05:27.52	1.07	2150	-	-	-	-	-	-	-	-	1.95	-	-
307	17:45:37.81, -29:05:27.40	0.46	1510	-	-	-	-	-	-	-	-	0.75	-	-
308	17:45:38.46, -29:05:26.90	0.29	1330	-	-	-	-	-	-	-	-	0.62	-	-
309	17:45:37.00, -29:05:26.48	1.25	2410	-	-	-	-	-	-	-	-	3.69	-	-
310	17:45:36.80, -29:05:25.30	0.36	1220	-	-	-	-	-	-	-	-	1.31	-	-
311	17:45:36.66, -29:05:23.38	2.38	1920	-	-	-	-	-	-	-	-	9.09	-	-
312	17:45:37.51, -29:05:22.80	2.79	2560	92.9±37	111±40	-	92.9±37	1.49±0.22	1.77±0.63	-	1.49±0.22	0.74	2.41±0.44	0.39
313	17:45:37.46, -29:05:22.60	0.54	1480	76.7±30.8	53±3.7	-	76.7±30.8	0.87±0.16	1.37±0.46	-	0.87±0.16	0.18	1.24±0.43	0.15
314	17:45:37.57, -29:05:21.97	0.38	1330	-	-	-	-	-	-	-	-	0.66	-	-
315	17:45:37.49, -29:05:21.88	0.42	1510	-	-	-	-	-	-	-	-	0.80	-	-
316	17:45:37.60, -29:05:21.75	0.29	1240	-	-	-	-	-	-	-	-	0.51	-	-
317	17:45:37.56, -29:05:20.68	14.32	5540	-	-	-	-	-	-	-	-	31.68	-	-
318	17:45:37.68, -29:05:20.94	0.34	1390	-	-	-	-	-	-	-	-	0.64	-	-
319	17:45:37.68, -29:05:20.59	0.23	1140	-	-	-	-	-	-	-	-	0.41	-	-
320	17:45:37.69, -29:05:19.50	0.56	1630	-	-	-	-	-	-	-	-	0.91	-	-
321	17:45:37.64, -29:05:19.05	0.67	2160	-	-	-	-	-	-	-	-	1.43	-	-
322	17:45:37.62, -29:05:18.15	0.31	1250	-	-	-	-	-	-	-	-	0.48	-	-
323	17:45:37.66, -29:05:14.28	4.25	3040	-	-	-	-	-	-	-	-	6.75	-	-
324	17:45:37.78, -29:05:10.07	1.2	2390	-	-	-	-	-	-	-	-	1.74	-	-
325	17:45:38.02, -29:05:09.08	1.71	2380	-	-	-	-	-	-	-	-	2.76	-	-
326	17:45:38.06, -29:05:08.73	0.31	1310	-	-	-	-	-	-	-	-	0.51	-	-
327	17:45:38.01, -29:05:04.40	0.22	1040	-	-	-	-	-	-	-	-	0.32	-	-
328	17:45:37.87, -29:05:04.20	5.12	2380	-	-	-	-	-	-	-	-	8.27	-	-
329	17:45:37.94, -29:05:03.96	13.71	3600	141.2±66.3	130±120	-	141.2±66.3	1.55±0.18	1.71±0.87	-	1.55±0.18	2.35	2.04±0.31	0.69
330	17:45:37.47, -29:05:03.68	0.37	1450	73.6±33.2	65±54	-	73.6±33.2	0.97±0.2	0.87±0.68	-	0.97±0.2	0.13	1.52±0.51	0.22
331	17:45:37.89, -29:05:03.21	2.67	2510	-	-	-	-	-	-	-	-	4.44	-	-
332	17:45:37.79, -29:05:03.11	16.16	1830	-	-	138.3±18.2	138.3±18.2	-	-	3.97±0.33	3.97±0.33	2.83	5.67±0.49	12.11
333	17:45:38.07, -29:05:03.04	1.61	2340	57.9±15.7	42±34	-	<98.8	1.26±0.2	1.21±0.68	-	1.26±0.2	<0.4	2.49±0.51	0.46
334	17:45:37.78, -29:05:02.59	16.58	2130	99.2±32.7	118±18	119.0±22.8	119.0±22.8	2.03±0.23	4.41±0.92	4.10±0.50	4.10±0.50	2.31	4.70±0.51	2.69
335	17:45:37.78, -29:05:02.22	3.93	1110	-	-	-	-	-	-	-	-	5.89	-	-
336	17:45:37.72, -29:05:02.02	0.28	1110	-	-	-	-	-	-	-	-	0.45	-	-
337	17:45:37.88, -29:05:01.90	0.28	1180	-	-	-	-	-	-	-	-	0.42	-	-
338	17:45:37.81, -29:05:01.86	0.67	1500	-	-	-	-	-	-	-	-	1.24	-	-
339	17:45:37.62, -29:05:01.46	0.83	2030	-	-	-	-	-	-	-	-	1.31	-	-
340	17:45:37.88, -29:05:01.41	0.24	1240	-	-	-	-	-	-	-	-	0.47	-	-
341	17:45:37.77, -29:05:01.06	2.42	1410	-	-	-	-	-	-	-	-	4.04	-	-
342	17:45:37.65, -29:05:00.83	0.23	1090	-	-	-	-	-	-	-	-	0.43	-	-

Table E3 continued

Table E3 (*continued*)

Core ID	RA and Dec	Flux	R	$T_{\text{H}_2\text{CO}}$	$T_{\text{H}_2\text{CO}}$	$T_{\text{CH}_3\text{CN}}$	T	$\sigma_{\text{H}_2\text{CO}}$	$\sigma_{\text{H}_2\text{CO}}$	$\sigma_{\text{CH}_3\text{CN}}$	σ	M_{core}	\mathcal{M}	$\alpha_{\text{vir},p}$
		density		LTE	non-LTE	LTE		LTE	non-LTE	LTE				
(1)	(J2000)	(mJy)	(AU)	(K)	(K)	(K)	(K)	(km s $^{-1}$)	(km s $^{-1}$)	(km s $^{-1}$)	(km s $^{-1}$)	(M_{\odot})	(14)	(15)
(2)	(3)	(4)	(5)	(6)	(7)	(8)	(9)	(10)	(11)	(12)	(13)			
343	17:45:37.76, -29:05:00.57	7.94	1980	-	-	-	-	-	-	-	-	13.83	-	-
344	17:45:37.59, -29:05:00.65	0.2	1370	-	-	-	-	-	-	-	-	0.69	-	-
345	17:45:37.64, -29:05:00.30	2.29	3250	-	-	-	-	-	-	-	-	6.03	-	-
346	17:45:37.76, -29:04:59.70	0.93	2250	-	-	-	-	-	-	-	-	1.73	-	-
347	17:45:37.60, -29:04:58.65	0.33	1310	-	-	-	-	-	-	-	-	0.57	-	-
348	17:45:38.35, -29:04:51.58	0.3	1220	-	-	-	-	-	-	-	-	1.06	-	-
349	17:45:34.87, -29:04:41.25	0.23	1040	-	-	-	-	-	-	-	-	0.34	-	-
350	17:45:38.70, -29:04:37.26	8.11	3040	-	-	-	-	-	-	-	-	12.22	-	-
351	17:45:35.21, -29:04:34.65	0.34	1240	-	-	-	-	-	-	-	-	0.52	-	-
352	17:45:34.99, -29:04:33.39	1.03	1950	-	-	-	-	-	-	-	-	1.55	-	-
353	17:45:37.81, -29:04:33.02	1.93	2810	-	-	-	-	-	-	-	-	4.86	-	-
354	17:45:34.98, -29:04:32.86	0.7	1580	70 ± 27	73 ± 29	-	<105.9	2.63 ± 0.43	3 ± 1	-	2.63 ± 0.43	<0.16	5.20 ± 0.94	1.76
355	17:45:37.79, -29:04:32.21	0.24	1110	-	-	-	-	-	-	-	-	0.54	-	-
356	17:45:38.25, -29:04:32.06	0.86	1890	167.1 ± 127.9	130 ± 110	-	167.1 ± 127.9	2.77 ± 0.41	1.6 ± 0.4	-	2.77 ± 0.41	0.12	3.55 ± 0.68	9.49
357	17:45:38.22, -29:04:31.35	0.99	1390	-	-	-	-	-	-	-	-	1.95	-	-
358	17:45:38.21, -29:04:30.81	1.75	1330	-	-	-	-	-	-	-	-	3.18	-	-
359	17:45:38.20, -29:04:30.40	2.12	1510	-	-	-	-	-	-	-	-	4.03	-	-
360	17:45:38.05, -29:04:28.65	0.88	2100	-	-	-	-	-	-	-	-	1.62	-	-
361	17:45:38.05, -29:04:28.14	0.38	1440	-	-	-	-	-	-	-	-	0.65	-	-
362	17:45:38.16, -29:04:27.80	1.25	2310	-	-	-	-	-	-	-	-	2.16	-	-
363	17:45:38.09, -29:04:27.85	3.32	2960	-	-	-	-	-	-	-	-	5.89	-	-
364	17:45:37.47, -29:04:27.39	0.92	2020	-	-	-	-	-	-	-	-	2.56	-	-
365	17:45:38.13, -29:04:27.40	0.2	1060	-	-	-	-	-	-	-	-	0.34	-	-
366	17:45:37.54, -29:04:27.34	0.37	1710	-	-	-	-	-	-	-	-	1.38	-	-
367	17:45:37.33, -29:04:26.84	4.7	3240	-	-	-	-	-	-	-	-	15.72	-	-
368	17:45:37.55, -29:04:26.83	0.69	2010	-	-	-	-	-	-	-	-	1.97	-	-
369	17:45:37.47, -29:04:26.89	0.33	1200	-	-	-	-	-	-	-	-	0.88	-	-
370	17:45:38.32, -29:04:26.40	1.12	2390	-	-	-	-	-	-	-	-	1.79	-	-
371	17:45:38.13, -29:04:24.84	0.47	1580	-	-	-	-	-	-	-	-	0.78	-	-
372	17:45:38.15, -29:04:24.41	0.32	1310	-	-	-	-	-	-	-	-	0.51	-	-
373	17:45:38.15, -29:04:24.12	0.44	1490	101.2 ± 48.2	102 ± 88	-	<90.8	1.85 ± 0.29	1.4 ± 0.5	-	1.85 ± 0.29	$0 < 0.12$	2.95 ± 0.56	7.32
374	17:45:38.34, -29:04:23.01	0.85	2100	99.7 ± 35.3	73 ± 4.5	-	99.7 ± 35.3	1.61 ± 0.2	1.47 ± 0.37	-	1.61 ± 0.2	0.21	2.54 ± 0.39	3.80
375	17:45:38.37, -29:04:22.68	0.53	1720	-	-	-	-	-	-	-	-	0.82	-	-
376	17:45:38.48, -29:04:21.79	0.28	1250	-	-	-	-	-	-	-	-	0.43	-	-
377	17:45:38.63, -29:04:20.52	0.49	1650	-	-	-	-	-	-	-	-	0.71	-	-
378	17:45:38.55, -29:04:20.41	0.44	1560	-	-	-	-	-	-	-	-	0.62	-	-
379	17:45:38.58, -29:04:16.76	0.97	2200	-	-	-	-	-	-	-	-	1.51	-	-
380	17:45:37.55, -29:03:52.03	0.49	1450	-	-	-	-	-	-	-	-	0.91	-	-
381	17:45:37.35, -29:03:51.88	0.77	1960	-	-	-	-	-	-	-	-	1.47	-	-
382	17:45:37.68, -29:03:51.82	0.21	1080	-	-	-	-	-	-	-	-	0.36	-	-
383	17:45:37.63, -29:03:51.73	0.92	1570	-	-	-	-	-	-	-	-	1.44	-	-
384	17:45:37.55, -29:03:51.66	0.91	1340	-	-	-	-	-	-	-	-	0.97	-	-
385	17:45:37.38, -29:03:51.50	0.25	1320	-	-	-	-	-	-	-	-	0.55	-	-
386	17:45:37.70, -29:03:51.23	0.83	1750	-	-	-	-	-	-	-	-	1.44	-	-
387	17:45:37.65, -29:03:51.28	0.59	1280	-	-	-	-	-	-	-	-	1.00	-	-
388	17:45:37.59, -29:03:51.29	0.58	1220	-	-	-	-	-	-	-	-	0.87	-	-
389	17:45:37.42, -29:03:51.15	0.29	1150	-	-	-	-	-	-	-	-	0.53	-	-
390	17:45:37.81, -29:03:51.12	0.93	1830	-	-	-	-	-	-	-	-	1.51	-	-
391	17:45:37.74, -29:03:50.98	0.52	1240	-	-	-	-	-	-	-	-	0.76	-	-
392	17:45:37.77, -29:03:50.83	0.34	1030	-	-	-	-	-	-	-	-	0.49	-	-
393	17:45:37.31, -29:03:50.80	0.44	1330	-	-	-	-	-	-	-	-	0.67	-	-
394	17:45:37.71, -29:03:50.62	0.68	1450	112.4 ± 81.3	132.8 ± 2.6	-	112.4 ± 81.3	1.14 ± 0.26	1.66 ± 0.93	-	1.14 ± 0.26	0.15	1.55 ± 0.52	0.36
395	17:45:37.65, -29:03:50.51	2.53	2000	-	-	-	-	-	-	-	-	3.91	-	-
396	17:45:37.49, -29:03:49.81	131.13	4770	-	-	421.4 ± 54.0	421.4 ± 54.0	-	-	3.61 ± 0.14	3.61 ± 0.14	8.29	3.01 ± 0.12	3.88
397	17:45:37.38, -29:03:50.08	2.13	2530	-	-	-	-	-	-	-	-	3.82	-	-
398	17:45:37.56, -29:03:50.27	1.16	1120	143.9 ± 86.8	77 ± 12	-	143.9 ± 86.8	2.76 ± 0.38	2.71 ± 0.49	-	2.76 ± 0.38	0.19	3.81 ± 0.64	5.47
399	17:45:37.64, -29:03:49.83	0.45	1210	-	-	-	-	-	-	-	-	0.68	-	-
400	17:45:37.70, -29:03:49.55	0.5	1360	-	-	-	-	-	-	-	-	0.74	-	-
401	17:45:37.85, -29:03:49.45	0.37	1330	-	-	-	-	-	-	-	-	0.60	-	-
402	17:45:37.77, -29:03:49.18	0.89	1610	-	-	-	-	-	-	-	-	1.40	-	-
403	17:45:37.60, -29:03:49.19	1.18	1280	-	-	-	-	-	-	-	-	1.84	-	-
404	17:45:37.82, -29:03:49.01	0.78	1730	-	-	-	-	-	-	-	-	1.33	-	-

Table E3 *continued*

Table E3 (*continued*)

Core ID	RA and Dec	Flux	R	$T_{\text{H}_2\text{CO}}$	$T_{\text{H}_2\text{CO}}$	$T_{\text{CH}_3\text{CN}}$	T	$\sigma_{\text{H}_2\text{CO}}$	$\sigma_{\text{H}_2\text{CO}}$	$\sigma_{\text{CH}_3\text{CN}}$	σ	M_{core}	\mathcal{M}	$\alpha_{\text{vir,p}}$	
		density		LTE	non-LTE	LTE		LTE	non-LTE	LTE					
(1)	(J2000)	(mJy)	(AU)	(K)	(K)	(K)	(K)	(km s $^{-1}$)	(km s $^{-1}$)	(km s $^{-1}$)	(km s $^{-1}$)	(M_{\odot})	(14)	(15)	
(2)	(3)	(4)	(5)	(6)	(7)	(8)	(9)	(10)	(11)	(12)	(13)				
405	17:45:37.71, -29:03:49.08	0.44	1060	-	-	-	-	-	-	-	-	0.65	-	-	
406	17:45:37.62, -29:03:48.72	2.56	1960	-	-	-	-	-	-	-	-	4.14	-	-	
407	17:45:37.48, -29:03:48.65	12.81	2040	-	-	-	-	-	-	-	-	20.30	-	-	
408	17:45:37.36, -29:03:48.64	0.21	1060	-	-	-	-	-	-	-	-	0.36	-	-	
409	17:45:37.91, -29:03:48.48	0.22	1030	-	-	-	-	-	-	-	-	0.33	-	-	
410	17:45:37.82, -29:03:48.48	0.21	1170	61.6 \pm 26.2	68 \pm 28	-	61.6 \pm 26.2	2.59 \pm 0.51	2.43 \pm 0.89	-	2.59 \pm 0.51	0.09	5.46 \pm 1.18	2.05	
411	17:45:37.94, -29:03:48.38	0.41	1410	-	-	-	-	-	-	-	-	0.63	-	-	
412	17:45:37.72, -29:03:48.30	8.85	1780	-	-	-	-	-	-	-	-	13.64	-	-	
413	17:45:37.97, -29:03:48.08	0.23	1970	-	-	-	-	-	-	-	-	1.27	-	-	
414	17:45:37.86, -29:03:48.11	0.79	1140	-	-	-	-	-	-	-	-	0.36	-	-	
415	17:45:37.65, -29:03:48.07	5.64	1790	-	-	-	-	-	-	-	-	8.63	-	-	
416	17:45:37.48, -29:03:48.12	2.76	1270	-	-	-	-	-	-	-	-	4.59	-	-	
417	17:45:37.89, -29:03:47.79	0.56	1980	-	-	-	-	-	-	-	-	1.08	-	-	
418	17:45:37.57, -29:03:47.71	1.56	1790	61.2 \pm 30.2	74.2 \pm 5.8	-	61.2 \pm 30.2	2.86 \pm 0.64	2.5 \pm 1.3	-	2.86 \pm 0.64	0.65	6.08 \pm 1.48	4.51	
419	17:45:37.52, -29:03:47.82	0.82	1170	-	-	-	-	-	-	-	-	1.14	-	-	
420	17:45:37.66, -29:03:47.57	15.33	2790	108 \pm 77.2	67.9 \pm 8.6	-	108 \pm 77.2	0.93 \pm 0.21	0.92 \pm 0.38	-	0.93 \pm 0.21	3.47	1.16 \pm 0.46	0.48	
421	17:45:37.74, -29:03:47.55	8.61	1600	-	-	-	-	-	-	-	-	13.14	-	-	
422	17:45:37.46, -29:03:47.15	0.29	1120	-	-	-	-	-	-	-	-	0.46	-	-	
423	17:45:37.74, -29:03:46.94	27.29	2100	-	-	79.8 \pm 14.1	79.8 \pm 14.1	-	-	2.19 \pm 0.22	2.19 \pm 0.22	7.17	4.12 \pm 0.42	2.60	
424	17:45:37.83, -29:03:47.01	0.56	1270	-	-	-	-	-	-	-	-	0.71	-	-	
425	17:45:37.97, -29:03:46.91	0.36	1760	-	-	-	-	-	-	-	-	0.89	-	-	
426	17:45:38.01, -29:03:46.68	0.55	1560	-	-	-	-	-	-	-	-	0.65	-	-	
427	17:45:37.90, -29:03:46.82	0.4	1030	-	-	-	-	-	-	-	-	0.41	-	-	
428	17:45:37.66, -29:03:46.69	1.09	1210	127.5 \pm 73.5	77 \pm 6.3	-	127.5 \pm 73.5	2.18 \pm 0.33	2.73 \pm 0.46	-	2.18 \pm 0.33	0.21	3.15 \pm 0.58	3.01	
429	17:45:37.92, -29:03:46.60	0.71	1420	-	-	-	-	-	-	-	-	1.02	-	-	
430	17:45:37.78, -29:03:46.33	0.63	2730	55.5 \pm 25.9	77 \pm 75	-	55.5 \pm 25.9	1.71 \pm 0.44	1.34 \pm 0.58	-	1.71 \pm 0.44	0.29	3.66 \pm 1.10	0.22	
431	17:45:38.07, -29:03:46.33	2.88	1730	-	-	-	-	-	-	-	-	0.88	-	-	
432	17:45:37.69, -29:03:46.16	3.85	1940	66.4 \pm 21	73 \pm 5.5	-	66.4 \pm 21	3.17 \pm 0.43	2.3 \pm 0.48	-	3.17 \pm 0.43	1.46	6.49 \pm 0.96	7.44	
433	17:45:38.03, -29:03:46.19	0.27	1220	-	-	-	-	-	-	-	-	0.42	-	-	
434	17:45:37.73, -29:03:46.27	0.52	1030	137 \pm 66.4	107 \pm 29	-	137 \pm 66.4	2.44 \pm 0.29	2.39 \pm 0.48	-	2.44 \pm 0.29	0.09	3.43 \pm 0.50	2.74	
435	17:45:37.90, -29:03:45.74	1.37	1850	-	-	-	-	-	-	-	-	2.42	-	-	
436	17:45:37.86, -29:03:45.86	0.68	1310	-	-	-	-	-	-	-	-	1.11	-	-	
437	17:45:37.96, -29:03:45.67	1.2	1940	-	-	-	-	-	-	-	-	1.95	-	-	
438	17:45:38.01, -29:03:44.98	1.63	2430	-	-	-	-	-	-	-	-	2.14	-	-	
439	17:45:38.08, -29:03:45.33	0.25	1120	-	-	-	-	-	-	-	-	0.35	-	-	
440	17:45:37.84, -29:03:44.99	3.22	2280	-	-	-	-	-	-	-	-	4.70	-	-	
441	17:45:37.96, -29:03:44.99	0.77	1720	-	-	-	-	-	-	-	-	1.11	-	-	
442	17:45:37.92, -29:03:44.54	0.54	1650	-	-	-	-	-	-	-	-	0.82	-	-	
443	17:45:37.93, -29:03:44.05	0.49	1570	52.8 \pm 18.3	41 \pm 28	-	52.8 \pm 18.3	1.99 \pm 0.37	2 \pm 1.1	-	1.99 \pm 0.37	0.24	4.44 \pm 0.93	5.82	
444	17:45:38.05, -29:03:43.75	3.98	3430	106.4 \pm 42.9	113 \pm 7.1	-	106.4 \pm 42.9	2.18 \pm 0.27	2.06 \pm 0.88	-	2.18 \pm 0.27	0.92	3.45 \pm 0.50	2.82	
445	17:45:37.98, -29:03:43.71	0.27	1140	-	-	-	-	-	-	-	-	0.34	-	-	
446	17:45:38.06, -29:03:43.14	0.29	1080	-	-	-	-	-	-	-	-	0.44	-	-	
447	17:45:38.14, -29:03:43.09	0.22	1080	-	-	-	-	-	-	-	-	0.36	-	-	
448	17:45:38.07, -29:03:42.86	0.5	1120	-	-	-	-	-	-	-	-	0.57	-	-	
449	17:45:38.11, -29:03:42.46	9.19	3440	131.4 \pm 50.6	117 \pm 12	-	131.4 \pm 50.6	3.19 \pm 0.29	3.2 \pm 1.2	-	3.19 \pm 0.29	1.70	4.64 \pm 0.51	9.11	
450	17:45:38.12, -29:03:41.57	0.21	1660	-	-	-	-	-	-	-	-	1.01	-	-	
451	17:45:38.21, -29:03:41.12	2.84	3800	-	-	-	-	-	-	-	-	10.40	-	-	
452	17:45:38.32, -29:03:40.49	3.99	3000	-	-	-	-	-	-	-	-	6.83	-	-	
453	17:45:38.07, -29:03:40.50	0.71	1820	78.8 \pm 27.9	69.6 \pm 1.5	-	78.8 \pm 27.9	1.6 \pm 0.25	1.67 \pm 0.54	-	1.6 \pm 0.25	0.22	2.84 \pm 0.53	2.42	
454	17:45:38.21, -29:03:40.34	1.44	2160	-	-	-	-	-	-	-	-	2.26	-	-	
455	17:45:38.25, -29:03:39.75	1.09	1970	101.1 \pm 53.6	101 \pm 31	-	101.1 \pm 53.6	1.5 \pm 0.28	1.39 \pm 0.73	-	1.5 \pm 0.28	0.26	2.32 \pm 0.55	2.04	
456	17:45:38.17, -29:03:39.26	5.34	2940	-	-	-	-	-	-	-	-	8.65	-	-	
457	17:45:38.31, -29:03:38.98	0.48	1150	-	-	-	-	-	-	-	-	0.81	-	-	
458	17:45:38.28, -29:03:38.96	0.99	1690	-	76.3 \pm 20.1	76.3 \pm 20.1	-	-	2.00 \pm 0.28	2.00 \pm 0.28	0.32	3.74 \pm 0.54	2.60		
459	17:45:37.96, -29:03:38.90	0.2	1080	-	-	-	-	-	-	-	-	0.32	-	-	
460	17:45:38.33, -29:03:37.85	1.4	3620	-	-	-	-	-	-	-	-	4.39	-	-	
461	17:45:38.28, -29:03:38.30	0.25	2120	-	-	-	-	-	-	-	-	1.83	-	-	
462	17:45:38.22, -29:03:38.42	0.69	1650	50.8 \pm 13.4	69.5 \pm 1.5	-	50.8 \pm 13.4	2.56 \pm 0.35	2.9 \pm 0.76	-	2.56 \pm 0.35	0.35	5.94 \pm 0.89	11.14	
463	17:45:38.39, -29:03:37.79	0.35	1340	-	-	-	-	-	-	-	-	0.55	-	-	
464	17:45:38.18, -29:03:37.52	4.65	3250	-	-	-	-	-	-	-	-	7.75	-	-	
465	17:45:38.28, -29:03:37.67	0.19	1040	-	-	-	-	-	-	-	-	0.33	-	-	
466	17:45:38.35, -29:03:36.82	2.12	2880	-	-	-	-	-	-	-	-	3.55	-	-	

Table E3 continued

Table E3 (*continued*)

Core ID	RA and Dec (J2000)	Flux (mJy)	R (AU)	$T_{\text{H}_2\text{CO}}$	$T_{\text{H}_2\text{CO}}$	$T_{\text{CH}_3\text{CN}}$	T (K)	$\sigma_{\text{H}_2\text{CO}}$	$\sigma_{\text{H}_2\text{CO}}$	$\sigma_{\text{CH}_3\text{CN}}$	σ	M_{core}	\mathcal{M}	$\alpha_{\text{vir},p}$			
				density	LTE	non-LTE		LTE	non-LTE	LTE	LTE	non-LTE	LTE	LTE	non-LTE	LTE	
				(1)	(2)	(3)	(4)	(5)	(6)	(7)	(8)	(9)	(10)	(11)	(12)	(13)	(14)
467	17:45:38.09, -29:03:37.03	0.8	1860	51.1 \pm 10.9	83 \pm 35	-	51.1 \pm 10.9	2.14 \pm 0.25	2.55 \pm 0.79	-	2.14 \pm 0.25	0.41	4.89 \pm 0.64	6.51	-	-	-
468	17:45:38.18, -29:03:36.57	0.28	1150	-	-	-	-	-	-	-	-	-	0.44	-	-	-	-
469	17:45:38.37, -29:03:35.92	0.66	1650	-	-	-	-	-	-	-	-	-	1.16	-	-	-	-
470	17:45:38.38, -29:03:35.37	1.08	2000	-	-	-	-	-	-	-	-	-	1.93	-	-	-	-
471	17:45:38.41, -29:03:34.94	0.58	1860	-	-	-	-	-	-	-	-	-	1.15	-	-	-	-

REFERENCES

- Ao, Y., Henkel, C., Menten, K. M., et al. 2013, A&A, 550, A135, doi: [10.1051/0004-6361/201220096](https://doi.org/10.1051/0004-6361/201220096)
- Astropy Collaboration, Robitaille, T. P., Tollerud, E. J., et al. 2013, A&A, 558, A33, doi: [10.1051/0004-6361/201322068](https://doi.org/10.1051/0004-6361/201322068)
- Astropy Collaboration, Price-Whelan, A. M., Sipőcz, B. M., et al. 2018, AJ, 156, 123, doi: [10.3847/1538-3881/aabc4f](https://doi.org/10.3847/1538-3881/aabc4f)
- Astropy Collaboration, Price-Whelan, A. M., Lim, P. L., et al. 2022, ApJ, 935, 167, doi: [10.3847/1538-4357/ac7c74](https://doi.org/10.3847/1538-4357/ac7c74)
- Barnes, A. T., Longmore, S. N., Battersby, C., et al. 2017, MNRAS, 469, 2263, doi: [10.1093/mnras/stx941](https://doi.org/10.1093/mnras/stx941)
- Bastian, N., Covey, K. R., & Meyer, M. R. 2010, ARA&A, 48, 339, doi: [10.1146/annurev-astro-082708-101642](https://doi.org/10.1146/annurev-astro-082708-101642)
- Battersby, C., Walker, D. L., Barnes, A., et al. 2024, 3-D CMZ I: Central Molecular Zone Overview. <https://arxiv.org/abs/2410.17334>
- Bergin, E. A., & Tafalla, M. 2007, ARA&A, 45, 339, doi: [10.1146/annurev.astro.45.071206.100404](https://doi.org/10.1146/annurev.astro.45.071206.100404)
- Bertoldi, F., & McKee, C. F. 1992, ApJ, 395, 140, doi: [10.1086/171638](https://doi.org/10.1086/171638)
- Bieging, J. H., Wilson, T. L., & Downes, D. 1982, A&AS, 49, 607
- Bonnell, I. A., Bate, M. R., Clarke, C. J., & Pringle, J. E. 2001, MNRAS, 323, 785, doi: [10.1046/j.1365-8711.2001.04270.x](https://doi.org/10.1046/j.1365-8711.2001.04270.x)
- Bonnell, I. A., Bate, M. R., & Zinnecker, H. 1998, MNRAS, 298, 93, doi: [10.1046/j.1365-8711.1998.01590.x](https://doi.org/10.1046/j.1365-8711.1998.01590.x)
- Callanan, D., Longmore, S. N., Battersby, C., et al. 2023, MNRAS, 520, 4760, doi: [10.1093/mnras/stad388](https://doi.org/10.1093/mnras/stad388)
- Cao, Y., Qiu, K., Zhang, Q., Wang, Y., & Xiao, Y. 2021, ApJL, 918, L4, doi: [10.3847/2041-8213/ac1947](https://doi.org/10.3847/2041-8213/ac1947)
- CASA Team, Bean, B., Bhatnagar, S., et al. 2022, PASP, 134, 114501, doi: [10.1088/1538-3873/ac9642](https://doi.org/10.1088/1538-3873/ac9642)
- Cheng, Y., Lu, X., Sanhueza, P., et al. 2024, ApJ, 967, 56, doi: [10.3847/1538-4357/ad3c41](https://doi.org/10.3847/1538-4357/ad3c41)
- Clauset, A., Shalizi, C. R., & Newman, M. E. J. 2009, SIAM Review, 51, 661, doi: [10.1137/070710111](https://doi.org/10.1137/070710111)
- Dell’Ova, P., Motte, F., Gusdorf, A., et al. 2024, A&A, 687, A217, doi: [10.1051/0004-6361/202348984](https://doi.org/10.1051/0004-6361/202348984)
- Downes, D., Wilson, T. L., Bieging, J., & Wink, J. 1980, A&AS, 40, 379
- Elmegreen, B. G., Klessen, R. S., & Wilson, C. D. 2008, ApJ, 681, 365, doi: [10.1086/588725](https://doi.org/10.1086/588725)
- Giannetti, A., Leurini, S., König, C., et al. 2017, A&A, 606, L12, doi: [10.1051/0004-6361/201731728](https://doi.org/10.1051/0004-6361/201731728)
- Ginsburg, A., Sokolov, V., de Val-Borro, M., et al. 2022, AJ, 163, 291, doi: [10.3847/1538-3881/ac695a](https://doi.org/10.3847/1538-3881/ac695a)
- Ginsburg, A., Henkel, C., Ao, Y., et al. 2016, A&A, 586, A50, doi: [10.1051/0004-6361/201526100](https://doi.org/10.1051/0004-6361/201526100)
- Ginsburg, A., Csengeri, T., Galván-Madrid, R., et al. 2022, Astronomy & Astrophysics, 662, A9
- Goldsmith, P. F. 2001, ApJ, 557, 736, doi: [10.1086/322255](https://doi.org/10.1086/322255)
- GRAVITY Collaboration, Abuter, R., Aimar, N., et al. 2022, A&A, 657, L12, doi: [10.1051/0004-6361/202142465](https://doi.org/10.1051/0004-6361/202142465)
- Hennebelle, P., & Chabrier, G. 2008, ApJ, 684, 395, doi: [10.1086/589916](https://doi.org/10.1086/589916)
- Henshaw, J. D., Barnes, A. T., Battersby, C., et al. 2023, in Astronomical Society of the Pacific Conference Series, Vol. 534, Protostars and Planets VII, ed. S. Inutsuka, Y. Aikawa, T. Muto, K. Tomida, & M. Tamura, 83, doi: [10.48550/arXiv.2203.11223](https://arxiv.org/abs/2203.11223)
- Henshaw, J. D., Longmore, S. N., Kruijssen, J. M. D., et al. 2016, MNRAS, 457, 2675, doi: [10.1093/mnras/stw121](https://doi.org/10.1093/mnras/stw121)
- Hildebrand, R. H. 1983, QJRAS, 24, 267
- Hopkins, A. M. 2018, PASA, 35, e039, doi: [10.1017/pasa.2018.29](https://doi.org/10.1017/pasa.2018.29)

- Hosek, Matthew W., J., Lu, J. R., Anderson, J., et al. 2019, ApJ, 870, 44, doi: [10.3847/1538-4357/aaef90](https://doi.org/10.3847/1538-4357/aaef90)
- Hußmann, B., Stolte, A., Brandner, W., Gennaro, M., & Liermann, A. 2012, A&A, 540, A57, doi: [10.1051/0004-6361/201117637](https://doi.org/10.1051/0004-6361/201117637)
- Kauffmann, J., Bertoldi, F., Bourke, T. L., Evans, N. J., I., & Lee, C. W. 2008, A&A, 487, 993, doi: [10.1051/0004-6361:200809481](https://doi.org/10.1051/0004-6361:200809481)
- Kauffmann, J., Goldsmith, P. F., Melnick, G., et al. 2017a, A&A, 605, L5, doi: [10.1051/0004-6361/201731123](https://doi.org/10.1051/0004-6361/201731123)
- Kauffmann, J., Pillai, T., & Goldsmith, P. F. 2013, ApJ, 779, 185, doi: [10.1088/0004-637X/779/2/185](https://doi.org/10.1088/0004-637X/779/2/185)
- Kauffmann, J., Pillai, T., Zhang, Q., et al. 2017b, A&A, 603, A89, doi: [10.1051/0004-6361/201628088](https://doi.org/10.1051/0004-6361/201628088)
- Kirk, H., Dunham, M. M., Di Francesco, J., et al. 2017, ApJ, 838, 114, doi: [10.3847/1538-4357/aa63f8](https://doi.org/10.3847/1538-4357/aa63f8)
- Klessen, R. S. 2000, ApJ, 535, 869, doi: [10.1086/308854](https://doi.org/10.1086/308854)
- Krieger, N., Ott, J., Beuther, H., et al. 2017, ApJ, 850, 77, doi: [10.3847/1538-4357/aa951c](https://doi.org/10.3847/1538-4357/aa951c)
- Kroupa, P. 2002, Science, 295, 82, doi: [10.1126/science.1067524](https://doi.org/10.1126/science.1067524)
- Kruijssen, J. M. D., Dale, J. E., & Longmore, S. N. 2015, MNRAS, 447, 1059, doi: [10.1093/mnras/stu2526](https://doi.org/10.1093/mnras/stu2526)
- Kruijssen, J. M. D., Longmore, S. N., Elmegreen, B. G., et al. 2014, MNRAS, 440, 3370, doi: [10.1093/mnras/stu494](https://doi.org/10.1093/mnras/stu494)
- Krumholz, M. R., Kruijssen, J. M. D., & Crocker, R. M. 2017, MNRAS, 466, 1213, doi: [10.1093/mnras/stw3195](https://doi.org/10.1093/mnras/stw3195)
- Larson, R. B. 2005, MNRAS, 359, 211, doi: [10.1111/j.1365-2966.2005.08881.x](https://doi.org/10.1111/j.1365-2966.2005.08881.x)
- Li, J., Liu, C., Zhang, Z.-Y., et al. 2023a, Nature, 613, 460, doi: [10.1038/s41586-022-05488-1](https://doi.org/10.1038/s41586-022-05488-1)
- Li, S., Sanhueza, P., Zhang, Q., et al. 2023b, ApJ, 949, 109, doi: [10.3847/1538-4357/acc58f](https://doi.org/10.3847/1538-4357/acc58f)
- Liu, H. B., Ho, P. T. P., Wright, M. C. H., et al. 2013, ApJ, 770, 44, doi: [10.1088/0004-637X/770/1/44](https://doi.org/10.1088/0004-637X/770/1/44)
- Longmore, S. N., Bally, J., Testi, L., et al. 2013, MNRAS, 429, 987, doi: [10.1093/mnras/sts376](https://doi.org/10.1093/mnras/sts376)
- Louvet, F., Sanhueza, P., Stutz, A., et al. 2024, arXiv e-prints, arXiv:2407.18719, doi: [10.48550/arXiv.2407.18719](https://doi.org/10.48550/arXiv.2407.18719)
- Lu, X., Cheng, Y., Ginsburg, A., et al. 2020, ApJL, 894, L14, doi: [10.3847/2041-8213/ab8b65](https://doi.org/10.3847/2041-8213/ab8b65)
- Lu, X., Zhang, Q., Kauffmann, J., et al. 2017, ApJ, 839, 1, doi: [10.3847/1538-4357/aa67f7](https://doi.org/10.3847/1538-4357/aa67f7)
- Lu, X., Mills, E. A. C., Ginsburg, A., et al. 2019a, ApJS, 244, 35, doi: [10.3847/1538-4365/ab4258](https://doi.org/10.3847/1538-4365/ab4258)
- Lu, X., Zhang, Q., Kauffmann, J., et al. 2019b, ApJ, 872, 171, doi: [10.3847/1538-4357/ab017d](https://doi.org/10.3847/1538-4357/ab017d)
- Lu, X., Li, S., Ginsburg, A., et al. 2021, ApJ, 909, 177, doi: [10.3847/1538-4357/abde3c](https://doi.org/10.3847/1538-4357/abde3c)
- Lu, X., Liu, J., Pillai, T., et al. 2024, ApJ, 962, 39, doi: [10.3847/1538-4357/ad1395](https://doi.org/10.3847/1538-4357/ad1395)
- Mangum, J. G., Darling, J., Menten, K. M., & Henkel, C. 2008, ApJ, 673, 832, doi: [10.1086/524354](https://doi.org/10.1086/524354)
- Matthews, B., Krivov, A., Wyatt, M., Bryden, G., & Eiroa, C. 2014, Protostars and Planets VI, eds. H. Beuther, R.S. Klessen, CP Dullemond, & T. Henning, University of Arizona Press, Tucson
- McMullin, J. P., Waters, B., Schiebel, D., Young, W., & Golap, K. 2007, in Astronomical Society of the Pacific Conference Series, Vol. 376, Astronomical Data Analysis Software and Systems XVI, ed. R. A. Shaw, F. Hill, & D. J. Bell, 127
- Möller, T., Endres, C., & Schilke, P. 2017, A&A, 598, A7, doi: [10.1051/0004-6361/201527203](https://doi.org/10.1051/0004-6361/201527203)
- Morris, M., & Serabyn, E. 1996, ARA&A, 34, 645, doi: [10.1146/annurev.astro.34.1.645](https://doi.org/10.1146/annurev.astro.34.1.645)
- Motte, F., Nony, T., Louvet, F., et al. 2018, Nature Astronomy, 2, 478, doi: [10.1038/s41550-018-0452-x](https://doi.org/10.1038/s41550-018-0452-x)
- Motte, F., Bontemps, S., Csengeri, T., et al. 2022, Astronomy & Astrophysics, 662, A8
- Myers, P. C., Hatchfield, H. P., & Battersby, C. 2022, ApJ, 929, 34, doi: [10.3847/1538-4357/ac5906](https://doi.org/10.3847/1538-4357/ac5906)
- Ntormousi, E., & Hennebelle, P. 2019, A&A, 625, A82, doi: [10.1051/0004-6361/201834094](https://doi.org/10.1051/0004-6361/201834094)
- Offner, S. S. R., Clark, P. C., Hennebelle, P., et al. 2014, in Protostars and Planets VI, ed. H. Beuther, R. S. Klessen, C. P. Dullemond, & T. Henning, 53–75, doi: [10.2458/azu_uapress_9780816531240-ch003](https://doi.org/10.2458/azu_uapress_9780816531240-ch003)
- Offner, S. S. R., Taylor, J., Markey, C., et al. 2022, MNRAS, 517, 885, doi: [10.1093/mnras/stac2734](https://doi.org/10.1093/mnras/stac2734)
- Ossenkopf, V., & Henning, T. 1994, A&A, 291, 943
- Padoan, P., & Nordlund, Å. 2011, ApJL, 741, L22, doi: [10.1088/2041-8205/741/1/L22](https://doi.org/10.1088/2041-8205/741/1/L22)
- Paglione, T. A. D., Jackson, J. M., Bolatto, A. D., & Heyer, M. H. 1998, ApJ, 493, 680, doi: [10.1086/305136](https://doi.org/10.1086/305136)
- Park, S.-M., Goodwin, S. P., & Kim, S. S. 2020, MNRAS, 494, 325, doi: [10.1093/mnras/staa668](https://doi.org/10.1093/mnras/staa668)
- Pattle, K., Ward-Thompson, D., Kirk, J. M., et al. 2015, MNRAS, 450, 1094, doi: [10.1093/mnras/stv376](https://doi.org/10.1093/mnras/stv376)
- Pillai, T., Kauffmann, J., Tan, J. C., et al. 2015, ApJ, 799, 74, doi: [10.1088/0004-637X/799/1/74](https://doi.org/10.1088/0004-637X/799/1/74)
- Pouteau, Y., Motte, F., Nony, T., et al. 2023, A&A, 674, A76, doi: [10.1051/0004-6361/202244776](https://doi.org/10.1051/0004-6361/202244776)
- Rathborne, J. M., Longmore, S. N., Jackson, J. M., et al. 2014, ApJL, 795, L25, doi: [10.1088/2041-8205/795/2/L25](https://doi.org/10.1088/2041-8205/795/2/L25)

- Robitaille, T., & Bressert, E. 2012, APLpy: Astronomical Plotting Library in Python, Astrophysics Source Code Library, record ascl:1208.017
- Sanhueza, P., Contreras, Y., Wu, B., et al. 2019, ApJ, 886, 102, doi: [10.3847/1538-4357/ab45e9](https://doi.org/10.3847/1538-4357/ab45e9)
- Santa-Maria, M. G., Goicoechea, J. R., Etxaluze, M., Cernicharo, J., & Cuadrado, S. 2021, A&A, 649, A32, doi: [10.1051/0004-6361/202040221](https://doi.org/10.1051/0004-6361/202040221)
- Scibelli, S., Shirley, Y., Schmiedeke, A., et al. 2023, MNRAS, 521, 4579, doi: [10.1093/mnras/stad827](https://doi.org/10.1093/mnras/stad827)
- Suárez, G., Galván-Madrid, R., Aguilar, L., et al. 2021, ApJ, 921, 48, doi: [10.3847/1538-4357/ac1bb9](https://doi.org/10.3847/1538-4357/ac1bb9)
- Tang, X. D., Esimbek, J., Zhou, J. J., et al. 2013, A&A, 551, A28, doi: [10.1051/0004-6361/201219809](https://doi.org/10.1051/0004-6361/201219809)
- van der Tak, F. F. S., Black, J. H., Schöier, F. L., Jansen, D. J., & van Dishoeck, E. F. 2007, A&A, 468, 627, doi: [10.1051/0004-6361:20066820](https://doi.org/10.1051/0004-6361:20066820)
- Walker, D. L., Longmore, S. N., Zhang, Q., et al. 2018, MNRAS, 474, 2373, doi: [10.1093/mnras/stx2898](https://doi.org/10.1093/mnras/stx2898)
- Williams, B. A., Walker, D. L., Longmore, S. N., et al. 2022, MNRAS, 514, 578, doi: [10.1093/mnras/stac1378](https://doi.org/10.1093/mnras/stac1378)
- Zhang, Q., Wang, K., Lu, X., & Jiménez-Serra, I. 2015, ApJ, 804, 141, doi: [10.1088/0004-637X/804/2/141](https://doi.org/10.1088/0004-637X/804/2/141)
- Zylka, R., Guesten, R., Henkel, C., & Batrla, W. 1992, A&AS, 96, 525